

Evaporitic–lacustrine mudstone laminites and prodelta mudlobes – continuity and change in the Hartmann’s Valley interval, Murray formation, Gale crater, Mars

JUERGEN SCHIEBER*, , KEVIN M. BOHACS†, DAVID BISH‡, MAX COLEMAN§,
LUCY THOMPSON¶, WILLIAM RAPIN** and ZALMAI YAWAR*

*Indiana University, Department of Geological Sciences, 1001 E 10th Str, Bloomington 47405, IN, USA
(E-mail: jschiebe@indiana.edu)

†KMBohacs GEOconsulting, 10018 Sugar Hill Drive, Houston 77042, TX, USA

‡Indiana University Molecular Structure Center, 800 E. Kirkwood Ave, Bloomington 47405, IN, USA

§NASA Jet Propulsion Laboratory, California Institute of Technology, M/S 300-123G, 4800 Oak Grove Drive, Pasadena 91109, CA, USA

¶Department of Earth Sciences, University of New Brunswick, 2 Bailey Dr, Fredericton E3B5A3, NB, Canada

**IRAP – CNRS, University of Toulouse, 2 avenue du Colonel Roche, Toulouse Cedex 4 BP 44346 31028, France

Associate Editor – Kevin Taylor

ABSTRACT

The sedimentary fill of Gale crater on Mars is dominated by lacustrine strata that are the focus of investigations into surface processes, climate change and habitability early in the planet’s history. This study focuses on the lower part of the explored portion of the Murray formation on Aeolis Mons (Mount Sharp) in the Pahrump Hills and Hartmann’s Valley field areas. At Pahrump Hills, sedimentary features and geochemical attributes of exposed mudstones suggest accumulation in an underfilled lake basin in which lake levels, shorelines and salinities fluctuated greatly at various temporal scales. The immediately superjacent stratigraphic interval, designated by the rover team as the Hartmann’s Valley member, has previously been interpreted as an aeolian-deposited sandstone interval. This fresh examination of all available data, however, suggests that the Hartmann’s Valley member is strongly dominated by the same mudstone facies that compose most of the underlying Pahrump Hills member. The one novel facies element encountered in the Hartmann’s Valley member are undulose bedded to convex bodies of mudstone that are oriented roughly north–south, suggestive of sediment supply from a northern fluvial source. Mudstones analogous in scale and character to these undulose mudstones occur on Earth in multiple modern and ancient lacustrine successions, and are related to deposition of prodelta mud lobes. The mudstones of the Hartmann’s Valley member record a continuation of the underfilled evaporative lake system proposed previously for the underlying Pahrump Hills member but with somewhat more variable environmental conditions. Hartmann’s Valley mudstones contain more abundant matrix CaSO₄, suggesting more severe evaporitic conditions, whereas the interbedded undulose bedded mudstones signify intermittent freshening and buildout of mud-dominated deltas into the lake. The textural similarities between Pahrump Hills and Hartmann’s Valley strata suggest that the Gale lacustrine system operated at a stable depositional mode with similar environmental parameters during both stratigraphic intervals.

Keywords Environmental analysis, evaporite, Gale crater, geochemistry, lake floor topography, Mars, prodelta mudstone, provenance, sequence stratigraphy.

INTRODUCTION

Overview

Since landing in Gale crater in August 2012, the Mars Science Laboratory (MSL) Curiosity rover has been used to explore sedimentary strata to understand past Martian depositional environments and their potential for habitability (Grotzinger *et al.*, 2012). Following initial studies of sedimentary strata exposed on the crater floor (e.g. Williams *et al.*, 2013; Grotzinger *et al.*, 2014; Schieber *et al.*, 2017; Edgar *et al.*, 2018), the rover arrived in the foothills of Aeolis Mons (informally called Mount Sharp) about two Earth years later (*ca* Sol 700). At the Pahrump Hills field site, the rover team commenced the ongoing examination of the Mount Sharp sedimentary succession.

Those strata, the Pahrump Hills member of the Murray formation (Mount Sharp group), were variously interpreted as mudstones deposited in: (i) an evaporitic–lacustrine setting (Schieber *et al.*, 2015, 2022), comparable to the Wilkins Peak Member of the Eocene Green River Formation, USA (Bradley, 1964; Smith *et al.*, 2015); (ii) a shallow lake that intermittently evaporated to dryness (Kah *et al.*, 2018); or (iii) as down-dip extensions of a fluvial-deltaic system with river-generated hyperpycnal flows (Grotzinger *et al.*, 2015; Stack *et al.*, 2019). Whereas the latter studies envision a stable freshwater lake depositional setting, Schieber *et al.* (2022) considered it as an underfilled, generally saline, lake system that recorded significant variations in lake level and water body salinity.

The stratigraphic interval overlying the Pahrump Hills member, the Hartmann’s Valley member of the Murray formation (Gwizd *et al.*, 2022), is the subject of the present study. The examination of this unit suggests a lack of significant lithological distinction from the underlying Pahrump Hills member. Because of this, the authors prefer instead to use the terms “Hartmann’s Valley interval” (HVi), observed between –4436 to –4411 m elevation (Gwizd *et al.*, 2022) along the rover traverse, and ‘Pahrump Hills interval’ (PHi) for all Murray strata

below it. Locally the sandstones of the Stimson formation (Banham *et al.*, 2018, 2021, 2022) unconformably overlie Murray formation strata (Watkins *et al.*, 2022) in the study area. The rover team, under the assumption of largely flat-lying Mount Sharp strata, uses elevation as a proxy for stratigraphic position.

Geological background

Located slightly south of the Martian equator, the *ca* 150 km diameter Gale crater (Fig. 1) has a central mound (Aeolis Mons/Mount Sharp) that consists of a *ca* 5.5 km thick succession of sedimentary rocks (Malin & Edgett, 2000; Grotzinger *et al.*, 2015). The originating impact occurred approximately 3.6 to 3.8 billion years ago (Thomson *et al.*, 2011; Le Deit *et al.*, 2013), or perhaps even 4 billion years ago (Werner, 2019). Shortly thereafter the sedimentary infilling of the crater commenced and extended through most of the Hesperian and possibly into the Early Amazonian period (*ca* 3.6 to 2.8 Gyr; Grant *et al.*, 2014; Palucis *et al.*, 2014). Orbital images as well as direct rover observations indicate that sediment accumulation was interrupted multiple times by erosive interludes (Malin & Edgett, 2000; Anderson & Bell III, 2010; Milliken *et al.*, 2010; Fedo *et al.*, 2022; Schieber *et al.*, 2022; Watkins *et al.*, 2022), some driven by aeolian processes that are still active today (Day & Kocurek, 2016; Ewing *et al.*, 2017; Schieber *et al.*, 2020).

As of May 2024, the rover has scaled almost 800 m of Mount Sharp strata over a time span of about nine years. A provisional and steadily evolving stratigraphic scheme has been used by the MSL team for the past 11 years (e.g. Fedo *et al.*, 2022) and its general structure is followed here.

The basal exposed succession of the Mount Sharp group (Fig. 2) has been assigned to the Murray formation, an interval of approximately 320 m stratigraphic thickness (e.g. Fedo *et al.*, 2022). The Pahrump Hills interval (PHi) spans approximately 25 m of the lowermost exposed Murray formation, and metres 0 to 15 were studied in considerable detail

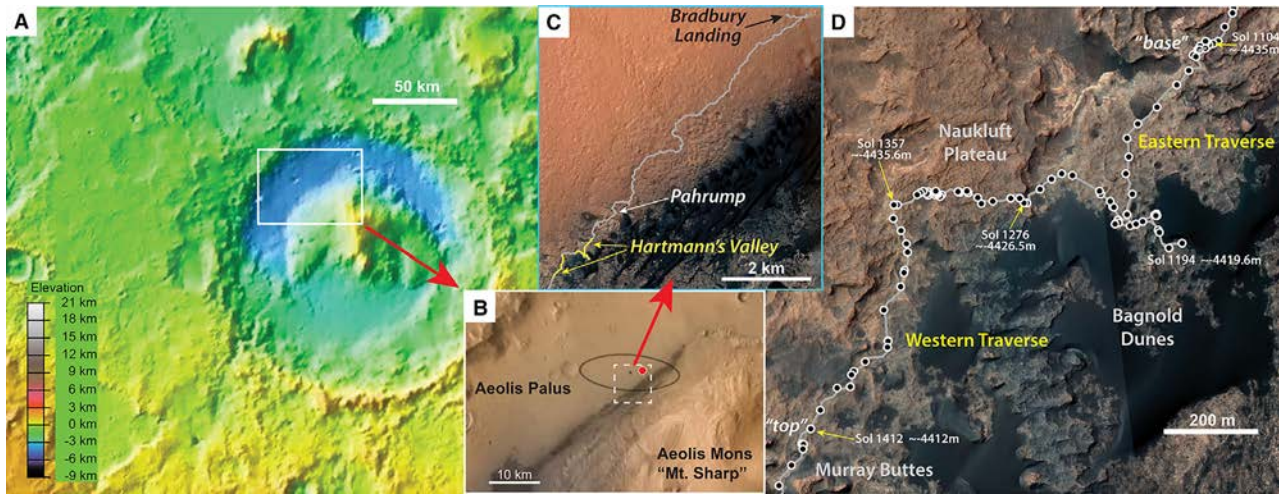


Fig. 1. Gale crater locations and rover track for the Hartmann's Valley elevation interval. (A) Elevation map of Gale crater. Inset (B) shows the landing site (red dot). The white dashed rectangle is the location of inset (C) that shows the rover traverse from the landing site (Bradbury Landing), the Pahrump Hills study area and the location of the rover traverses (yellow lines) across the Hartmann's valley elevation interval. (D) Shows the Hartmann's Valley rover traverses in the context of other landmarks. Black dots are rover locations (some marked with arrival Sol). Yellow arrows point to start and end points for the eastern and western Hartmann's Valley traverses, together with arrival Sol and approximate elevation of the presumed base and top of the interval (Fedo *et al.*, 2022). Credit for component images: NASA/JPL/GSFC/University of Arizona, image (D) basemap: Calef, F.J. III, and Parker, T., 2016, MSL Gale merged orthophoto mosaic (25 cm per pixel scale): U.S. Geological Survey NASA Planetary Data System (PDS) Annex, https://bit.ly/MSL_Basemap.

(Kah *et al.*, 2018; Stack *et al.*, 2019; Schieber *et al.*, 2022) owing to the high quality of the exposure. Multiple rover traverses, a high density of image and analytical data, as well as good lateral context, provided a unique opportunity for in-depth investigation of Martian sedimentology and stratigraphic architecture (Schieber *et al.*, 2022) at that site. The overlying 10 m of the PHi are poorly exposed along the traverse from the Pahrump Hills field site to the presently interpreted top of the PHi (Gwizd *et al.*, 2022) at the Sol 1104 location (Fig. 1), about 770 m to the south-west. Although during the traverse of this portion of the PHi the rover's resources were focused on better understanding the sandstone-dominated Stimson formation that unconformably overlies the Murray formation (e.g. Banham *et al.*, 2018), available images of Murray lithologies suggest that it stayed in character with what was observed at Pahrump Hills (Figs 3 and 4).

Images of the HVi collected between Sol 1104 and Sol 1412 (the top of the Hartmann's Valley member as interpreted by Gwizd *et al.*, 2022) suggests that this approximately 25 m thick interval (−4436 to −4411 m elevation) is

dominated by the same evaporitic-lacustrine facies that characterize the PHi (Schieber *et al.*, 2022). Given that the amount of observable detail at any given location is quite limited compared to Pahrump Hills (Schieber *et al.*, 2022), a significant part of the present evaluation relies on textural and compositional comparison to laminated mudstones as observed at Pahrump Hills.

Objective of study

Depositional setting and history of the HVi has been the subject of a prior study that characterized the HVi as an interval of largely aeolian sandstones (Gwizd *et al.*, 2022). In contrast, the authors consider the HVi to be dominated by lacustrine evaporitic mudstones that share many characteristics with those of the underlying PHi (Schieber *et al.*, 2022). These irreconcilable differences, based on careful examination of the exact same data base, were the impetus to prepare this manuscript. In the following sections, observed facies are compared with those already seen in the underlying PHi. Stratigraphic and lateral distribution of these facies, examined in

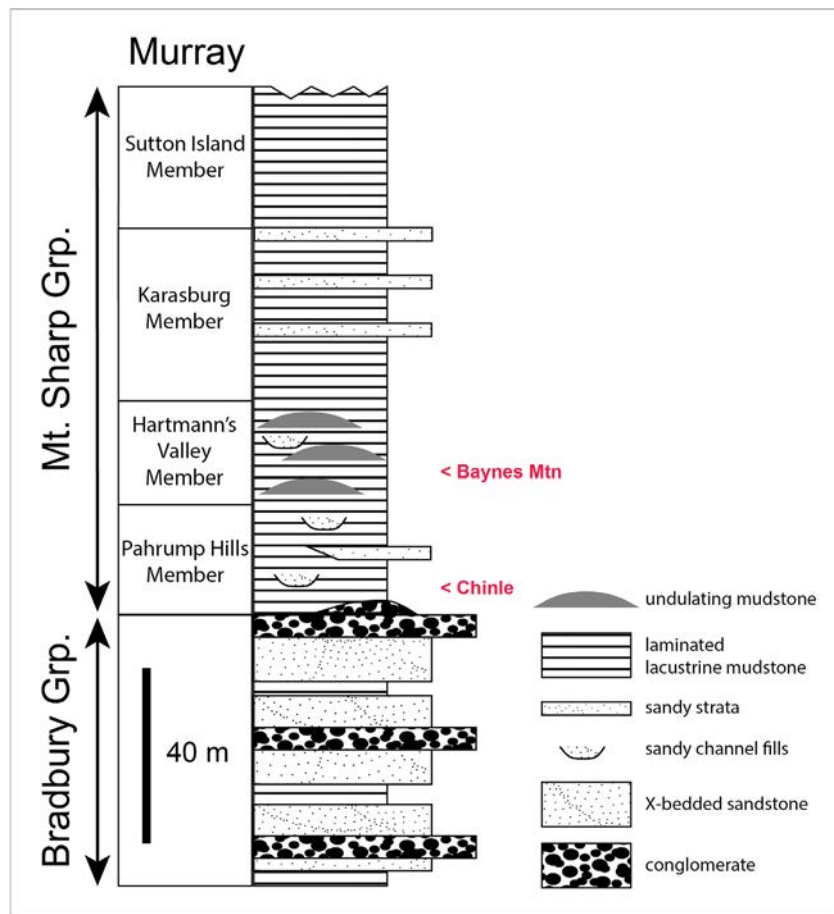


Fig. 2. Stratigraphic overview of the lower exposed portion of the Murray formation, adapted from Schieber *et al.* (2022). The Pahrump Hills member is dominantly laminated mudstones with an extensive sandstone interval (Salsberry Peak) and sandstone lenses. Unlike other publications where the Hartmann's Valley member is depicted as a sandstone interval (e.g. Fedo *et al.*, 2022; Gwizd *et al.*, 2022), it is here shown as consisting of laminated mudstones with lenses of undulating mudstone, reflecting the conclusions reached in this study. The key stratigraphic levels of Chinle and Baynes Mtn are marked in red.

the context of Earth analogues, allows for a starkly different alternative interpretation. Subsequent integration with mineralogical and chemical data collected by the rover instruments adds a compositional dimension to this analysis and provides a holistic perspective of the sedimentological and stratigraphic evolution of the HVi. The conclusions reached herein are then followed by a discussion that highlights crucial differences to Gwizd *et al.* (2022) with regard to the assessment of sediment grain size (mud instead of sand) and the presence (or rather absence) of aeolian cross-stratification, and affirm an assessment of the HVi as deposited in the context of an underfilled evaporative lake system.

Methods and instruments

'Rover geology' differs fundamentally from Earth-based field geology, being quite slow and fraught with omissions and ambiguity, as

pointed out in earlier publications (Schieber *et al.*, 2017, 2022). Compared with the Pahrump Hills campaign that expended a total of 206 Earth days to study 15 m of stratigraphy, the traverse across the HVi spent 233 Earth days to describe 25 m of stratigraphy. Yet, in the Pahrump Hills the rover investigated an area of only roughly 60 m by 80 m and drove a total of 534 m on multiple intersecting traverses (Minitti *et al.*, 2019), whereas for the HVi it traversed 1949 m along a single track and also investigated outcrops of the Stimson formation and the Bagnold field site of active sand dunes for multiple days (Banham *et al.*, 2018). Less time was devoted to individual exposures, and consequently stratigraphic context within the HVi is burdened with more uncertainty. A further consideration is slope – the overall north–south slope of the Pahrump Hills outcrop is nine degrees, whereas the average slope of the HVi traverse is about two to three degrees. Thus, HVi imaging was dominated by places where

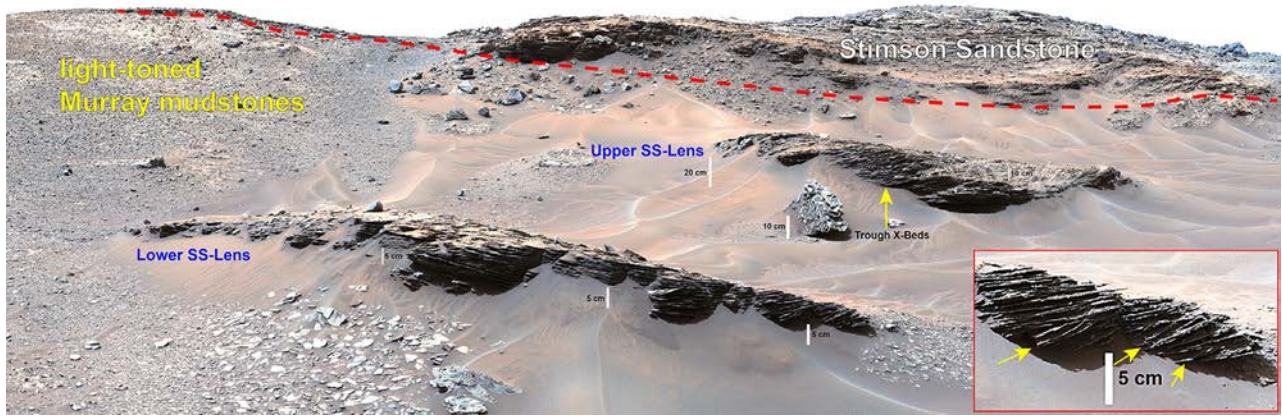


Fig. 3. Outcrop of the Logan's Pass area shows the unconformable contact (dashed red line) between the mudstones of the Murray formation and the overlying Stimson sandstone. The Murray formation rocks below the unconformity, including the two sandstone lenses, are considered part of the Pahrump Hills interval (PHi). The two sandstone lenses are in the same elevation range as sandstone channel fills seen at Pahrump Hills (for example, Whale Rock, Newspaper Rock; Schieber *et al.*, 2022), and show the same style of cross-stratification (enlarged lower right inset, yellow arrows point to cross-beds). Generally, the Murray is covered with float from the Stimson and wind-blown sand, but low exposures like those in the upper left corner are common, yet inaccessible. Image: MR_004283, acquired on Sol 969.

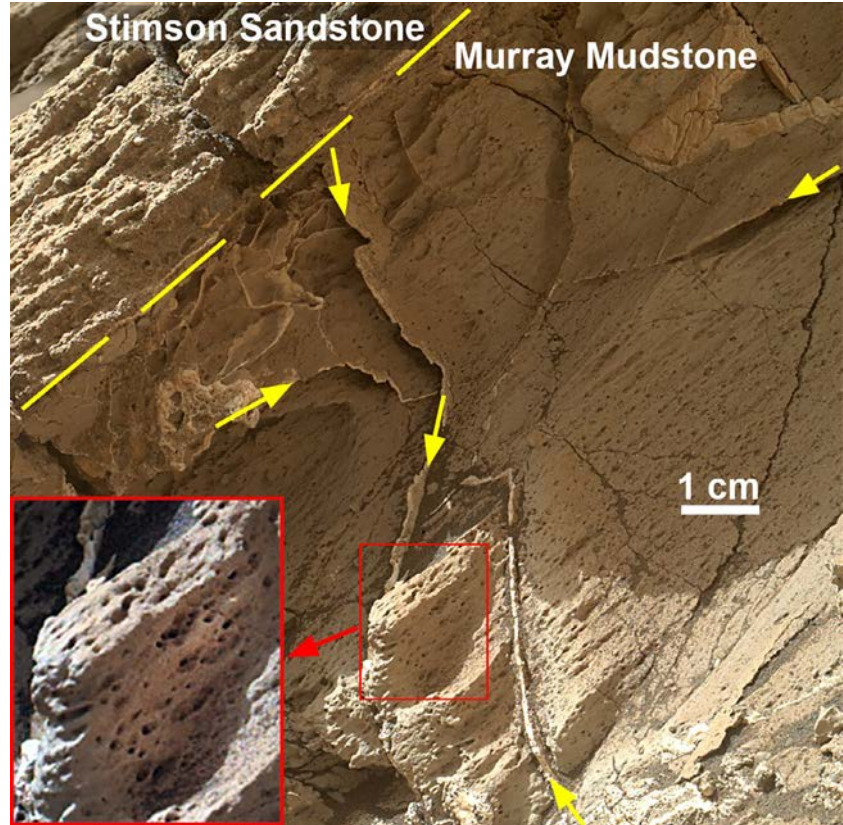


Fig. 4. MAHLI close-up (Sol 1031) of the Murray-Stimson unconformity. The underlying Murray is less erosion resistant than the Stimson sandstone and the Ca-sulphate veins (yellow arrows; Newsom *et al.*, 2018) that rise above the mudstone surface. The Murray shows the holes (enlarged red-framed inset) that at Pahrump Hills signify sites formerly occupied by evaporite minerals or their pseudomorphs (Schieber *et al.*, 2022).

bedding orientation and local slope were quite close, and thus bedding plane views dominate what could be imaged near the rover. Moreover, by the time the rover arrived at the base of the HVi, about three years and 11 km of drive distance had passed since landing, with a craft that was only guaranteed to last for two years and wheels that had seen more wear than anticipated. There was a sense of urgency to reach the mission objective (the clay and sulphate-bearing strata seen from orbit), still another 9 km (and as it turned out more than three years drive time) ahead on an increasingly steep drive. Thus even though most of the scientists on the team would have loved to linger longer, the overriding mood was ‘drive baby – drive’.

Observations of physical attributes (grain size, bedding, sedimentary structures, stratigraphy, geomorphology) relied mainly on the Mastcam 34 mm, Mastcam 100 mm, MARDI, and MAHLI cameras (see table 1 in Schieber *et al.*, 2022). Source information for the images shown in the various figures is listed in Appendix S1.

The image data can also be explored through a wireless holographic computer headset (Microsoft HoloLens) in combination with the OnSight software interface, a technology that enables scientists to explore the surface virtually. With this system, composite images of the Mars surface are used to construct a three-dimensional mesh that allows the user to ‘walk’ virtually around the study area. OnSight superimposes visual information and real rover data onto the HoloLens’s rectangular field of view, where holographic computing generates a realistic environment for exploration (Eldridge, 2018).

Compositional attributes were measured by the CheMin (mineralogy by X-ray diffraction – XRD), APXS (major and some trace elements by X-ray spectroscopy) and ChemCam (major elements by Alpha Particle X-ray Spectrometer) instruments (see table 1 in Schieber *et al.*, 2022). The rover uses a stainless-steel-bristle rotary brush (Dust Removal Tool or DRT; Davis *et al.*, 2012) to remove dust and loose sediment, and its interactions with the rock surface also serve as an empirical indicator of bedrock hardness. The areal coverage of analyses varies by instrument (see table 1 in Schieber *et al.*, 2022). CheMin, APXS and DRT are ‘contact’ tools – they require the target to be ≤ 2.5 m from the rover, on a relatively low slope, and tend to cluster around areas where the rover remained stationary for multiple days. ChemCam can analyse

targets up to *ca* 4 m from the rover and therefore has the most complete vertical coverage.

The capabilities and operations of the various cameras and instruments have already been described in preceding MSL publications and the reader is referred to those publications and references therein for further information (e.g. Maurice *et al.*, 2012; Gellert *et al.*, 2015; Schieber *et al.*, 2017, 2022; Miniti *et al.*, 2019; Thompson *et al.*, 2020; Wiens *et al.*, 2012). Appendix S2 has further information on specific technical details. An effort to better use the Mars Hand Lens Imager camera (MAHLI; Edgett *et al.*, 2012) for mudstone characterization was described previously (Schieber *et al.*, 2022); it uses the concept of ‘random single pixel variability’ (RSPV or ‘pixel salad’; Schieber, 2018). In essence, Martian mudstones that show RSPV in close range MAHLI images are presumed to consist largely of particles ≤ 20 μm in size. Rock and bedding nomenclature follows Lazar *et al.* (2015, 2022). The terms ‘mudstone’ and ‘sandstone’ are defined strictly on grain size; laminae and beds are defined by stratal geometry, not by arbitrary thickness. Because inputs from multiple instruments and geoscience disciplines require an iterative approach to the evaluation of data sets, our process of discovery, discussion and iteration follows the principles summarized in Schieber *et al.*, 2022 (fig. 3).

FACIES TYPES AND STRATIGRAPHIC SUCCESSION

During a preceding investigation of the Pahrump Hills field site by the authors of this study (Schieber *et al.*, 2022), specific locations were visited multiple times and imaged from multiple vantage points and sun angles, and each rock type was analysed often enough to allow further discrimination based on geochemistry interpreted from APXS and ChemCam LIBS (Laser Induced Breakdown Spectroscopy) data. Due to time constraints, such data density was not achievable during the subsequent traverse of the Hartmann’s Valley interval. Yet, the depth to which the Pahrump Hills strata were investigated still pays dividends as the rover ascends Mount Sharp – it honed investigative methodologies, built experience in interpretation, and leverages the extensive PH data set towards more refined interpretations of overlying younger strata. Collectively, these were the factors that enabled recognition of key sedimentary

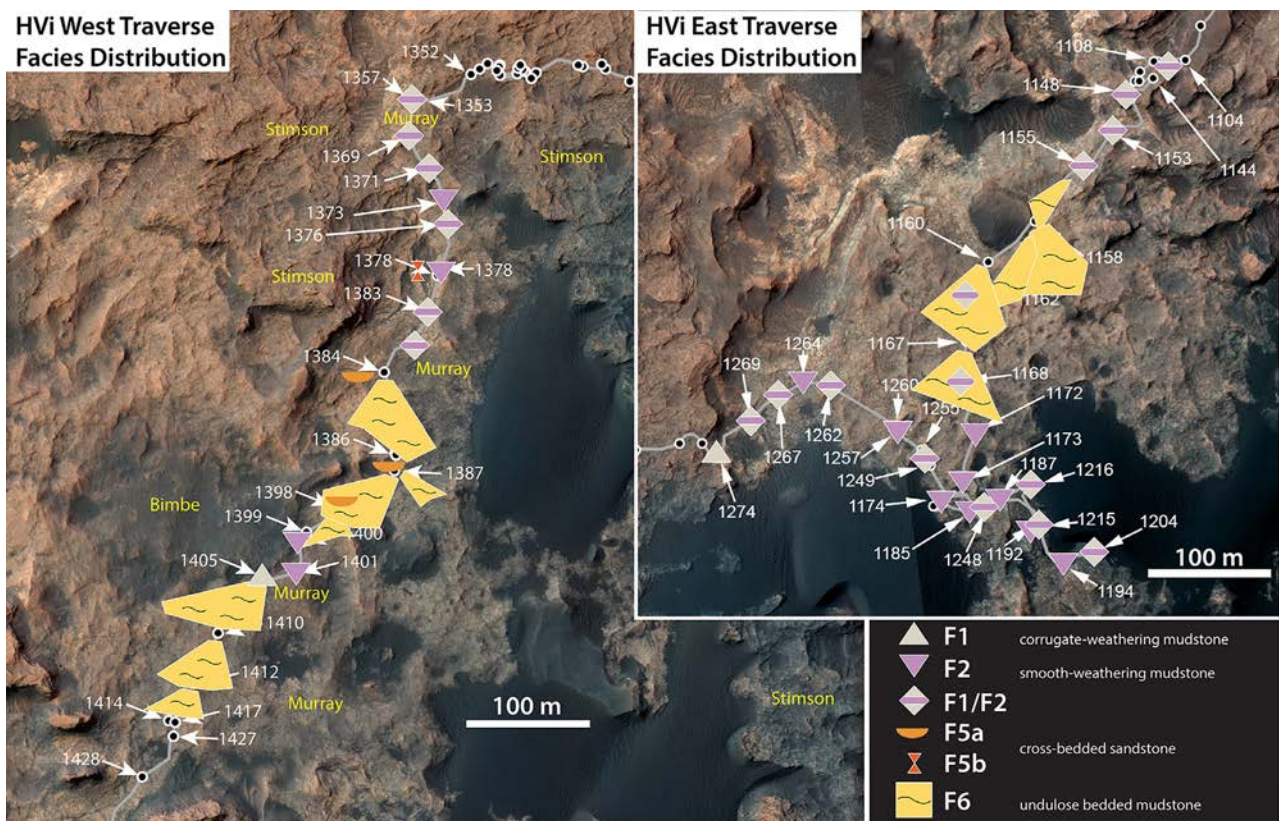


Fig. 5. Distribution of Hartmann's Valley facies along the eastern and western rover traverse (from MARDI, MAHLI and Mastcam images). Symbols indicate prevalent facies at a given location. For facies F6, whose characteristic features are best observed at some distance, the best visibility within a given viewshed is approximated by polygons, with lateral extent indicated by the map scale. Numbered arrows indicate rover arrival Sol. Elevation (and stratigraphic up) increases generally to the south (base map from Calef, F.J. III, and Parker, T., 2016, MSL Gale merged orthophoto mosaic (25 cm per pixel scale); U.S. Geological Survey NASA Planetary Data System (PDS) Annex, https://bit.ly/MSL_Basemap.)

attributes in the sub-optimal exposures of the HVi.

The facies scheme used for the HVi builds on facies defined in the underlying PHi (Schieber *et al.*, 2022). Corrugate-weathering and smooth-weathering mudstones occur along both the Hartmann's Valley eastern and western traverses (Fig. 5), closely resembling facies F1 and F2 from the Pahrump Hills succession (Schieber *et al.*, 2022). In places interstratification of F1 and F2 results in upward cemented parasequences similar to those observed at Pahrump (Fig. 6). Two of the PHi facies (F3 and F4) are absent in the HVi. Sandstone occurrences resemble in context and texture the laterally-discontinuous sandstone facies (F5a) at Pahrump. A new facies element (F6) contains mudstone beds organized into a larger-scale repeated

geometric pattern. All of these facies show coherent mappable patterns (Fig. 5). Even though the accompanying geochemical and mineralogical data are not as extensive, the controlling factors delineated for the depositional system at the Pahrump Hills field site are presumed to also apply to the HV interval. For the HVi facies, designations F1, F2 and F5 were retained as defined at Pahrump (Schieber *et al.*, 2022), and designation F6 was added to arrive at the four facies scheme shown in Table 1.

Based on observations of many lacustrine mudstone successions on Earth (Gierlowski-Kordesch & Kelts, 1994, 2000), and the rather limited range of plausible bedrock compositions in the catchment area around Gale crater (Taylor & McLennan, 2009), it is plausible to expect that there will be no dramatic change in mudstone

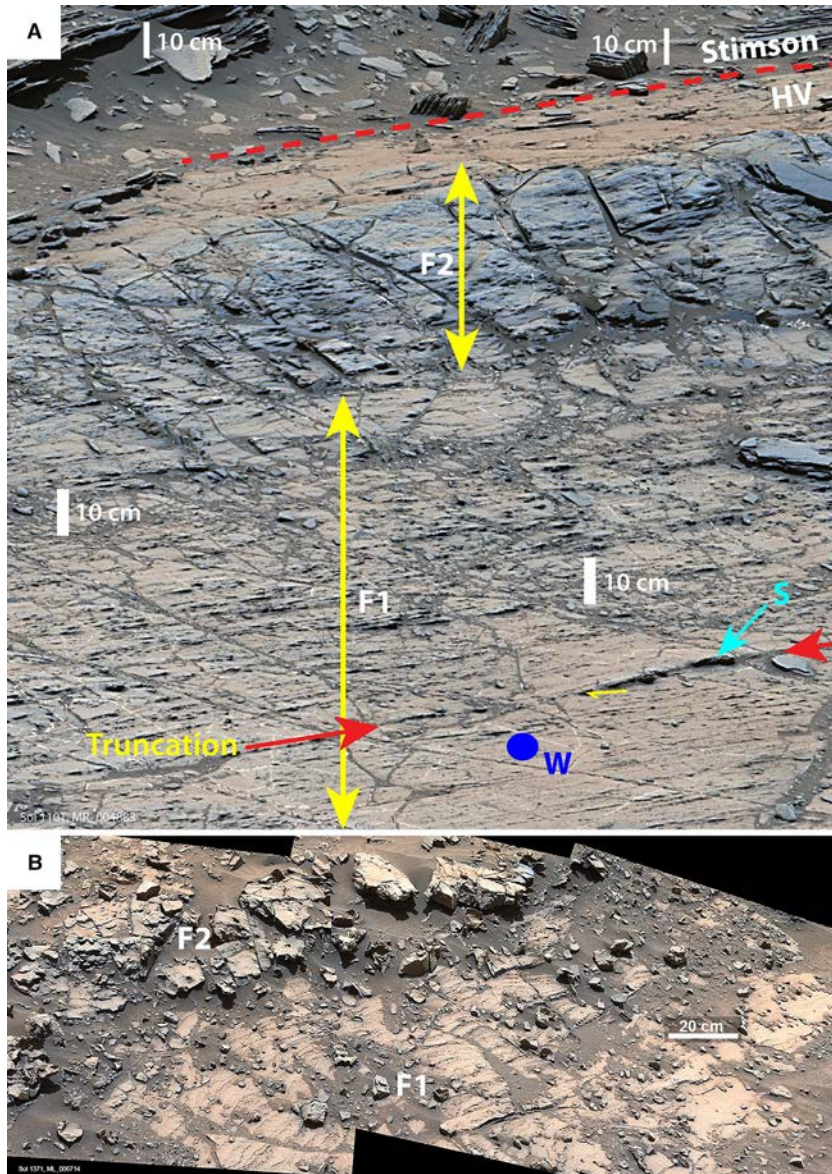


Fig. 6. Two examples of vertical association of F1 and F2, suggestive of parasequence development as seen at Pahrump Hills (Schieber *et al.*, 2022). (A) From base of eastern traverse, Sol 1101. Shows the unconformable contact (dashed red line) with the overlying Stimson sandstone, vertical distribution of facies F1 and F2 (yellow double arrows), W = Winnipeg DRT (area where dust removal tool was deployed), S = Sacajawea target, red arrows point to a low angle truncation surface, and yellow half arrow points to angular truncation of layering at that surface. (B) From lower portion of western traverse (Sol 1371). Corrugate-weathering facies F1 is overlain by smooth-weathering facies F2.

styles, but mostly variations on a limited set of themes going further upward in the Mount Sharp succession. For example, the mudstone-dominated Green River Formation on Earth (Bradley, 1964; Remy, 1992), a 1000 m thick interval of strata that consists of multiple stacked lacustrine depositional sequences, does not consist of a myriad of mudstone facies. Instead, a limited set of mudstone facies, differing in detail, but enduring in substance, recurs in changing configurations throughout that succession, as well as in many other lake-strata successions (Gierlowski-Kordesch & Kelts, 1994, 2000; Bohacs *et al.*, 2007). Examination of images from the HV1 traverses suggest

that this concept is also applicable to Martian mudstone successions.

Facies F1, corrugate-weathering mudstone

There are widespread observations of F1-style bedding along the Hartmann's Valley traverses from the Mastcam, MAHLI and MARDI perspectives. Figure 7 shows a comparison of MARDI images from Hartmann's Valley and Pahrump Hills.

As Fig. 7 illustrates, the laminated mudstones from PH and the HV traverses appear closely related or identical. At Mastcam resolution as

Table 1. Sedimentary facies of the Hartmann's Valley interval, Murray Formation: PH = Pahrump Hills; HV = Hartmann's Valley.

	Facies F1	Facies F2	Facies F5	Facies F6
	Corrugate-weathering mudstone	Smooth-weathering mudstone	Cross-bedded sandstone (F5a = discontinuous lenses; F5b = laterally extensive)	Undulose bedded mudstone
Occurrence	PH & HV	PH & HV	PH & HV	HV
Grain size	Detrital grains: probably dominated by particles <20 mm	Detrital grains: probably dominated by particles <20 mm	Detrital framework grains: 100 mm up to 700 mm (medium to coarse sand; moderately well-sorted); ripup clasts: 0.1 to 24 mm	Detrital grains: with a higher abundance of coarse silt (30 to 63 mm particles) than F1 and F2
	Authigenic particles: <2 mm; 0.4 to 2.6 mm (mode: 1.3 mm) long by 0.15 to 0.35 mm (mode: 0.25 mm) wide in basal 0.5 m of section	Authigenic particles: <2 mm; 0.6 to 1.8 mm (mode: 1.1 mm) long by 0.2 to 0.6 mm (mode: 0.45 mm) wide at Pink Cliffs and Book Cliffs		
Layer thickness	0.4 to 3.0 mm (below Chinle); 0.8 to 4.0 mm (above Chinle)	3 to 20 mm	Laminae: 1 to 10 mm; beds: 20 to 110 mm	Laminae: millimetre-scale; beds: centimetres to decimetres
Lamina/Bed geometry	Continuous planar parallel to discontinuous planar parallel	Continuous planar parallel (horizontal and inclined); continuous curved parallel; discontinuous curved nonparallel	Discontinuous curved nonparallel, with sparse discontinuous wavy nonparallel, discontinuous wavy parallel and continuous planar parallel	Continuous wavy-tabular and subparallel to nonparallel, with sparse discontinuous curved nonparallel
Bedding terminations	Truncation, downlap, onlap	Truncation, downlap, onlap	Truncation, downlap	Truncation, downlap
Sedimentary structures	Scour surfaces, planar-parallel beds	Scour surfaces, planar-parallel beds, current ripples	Scours, planar-parallel beds, current ripples, planar-tabular and trough cross-beds, compound cross-beds, foreset bundles, mud drapes	Undulose, variably dipping beds, may form convex outcrop expressions, decimetre-scale beds may show low-angle cross-stratification
Composition	Feldspars, mafics, Fe-oxides, silica, phyllosilicates, sulphates (Fe, Ca, Mg), ilmenite, pyrite, apatite, shortite, allophane	Feldspars, Fe-oxides, mafics, phyllosilicates, silica, sulphates (Fe, Mg), pyrite, allophane F5	Sand: feldspar (plagioclase), mafic minerals (pyroxene, olivine, magnetite), rock fragments and mud clasts	Feldspars, mafics, Fe-oxides, silica, phyllosilicates, sulphates (Fe, Ca, Mg)
Authigenic components	Crystal pseudomorphs, dendrites, stack concretions, isolated concretions (concretions sparse above Chinle)	Tabular concretions; oblate-spheroidal concretions (Potatoe, Searles)	None observed	None observed

Table 1. (continued)

	Facies F1	Facies F2	Facies F5	Facies F6
	Corrugate-weathering mudstone	Smooth-weathering mudstone	Cross-bedded sandstone (F5a = discontinuous lenses; F5b = laterally extensive)	Undulose bedded mudstone
Crystal shapes	Rhomb, pyramidal-triangular, lath-blade, lozenge (white); rounded-oval (above Chinle only)	Pyramidal-triangular, tabular-rhomb-blade (black), tabular-lozenge hole, lath-blade, lozenge (white)	Not apparent	Not apparent
Grain/Particle origin	Detrital mudstone grains; Authigenic <i>in situ</i> crystal pseudomorphs	Detrital mudstone grains; authigenic particles: <i>in situ</i> and reworked authigenic particles	Detrital mudstone and sandstone grains	Detrital mudstone grains
% of vertical section	20 to 40%	30 to 40%	0 to 10%	30 to 50%

well, lamina styles between Pahrump Hills and Hartmann's Valley are closely comparable (Fig. 8).

At PH, the corrugated appearance of this type of rock reflects alternating layers of greater and lesser resistance to aeolian abrasion. Less resistant layers consist of poorly sorted mud that contains dispersed coarse-silt-size particles and mud aggregates (Schieber *et al.*, 2022), whereas more resistant layers contain sand-sized sediment-incorporative crystal pseudomorphs (Schieber *et al.*, 2022). The HV laminae (Fig. 8A) closely resemble the PH corrugate-weathering mudstone as illustrated in Fig. 8B and C. The resistant parts of the HV laminae contain sand-sized sediment-incorporative crystal pseudomorphs with rhombic, pyramidal-triangular, lath-blade and lozenge shapes similar to those in the resistant laminae at Pahrump (Schieber *et al.*, 2015; Kah *et al.*, 2018).

At the magnification level of the MAHLI camera, the laminated rocks at PH and HV still appear quite similar (Fig. 9). Whereas at the Winnipeg location (HV) the laminae appear less continuous when compared to the Pelona target (PH), in both cases the resistant laminae are defined by rounded as well as angular objects/grains in the millimetre to sub-millimetre size range. At high magnification (Fig. 9C and D) the laminae have a quite similar expression, with the larger grains embedded in a mudstone matrix. At PH, the lamina-defining grains

were interpreted as pseudomorphs of evaporite minerals that grew in water-rich muds as a consequence of high salinity and penecontemporaneous mineral precipitation, based on pseudomorph shapes, distribution and chemical analyses, as well as geochemical modelling (Schieber *et al.*, 2022). The textural similarity of these grains at PH to those at HV (Figs 8 and 9) suggests that this interpretation can be extended to Winnipeg and elsewhere in the HVi.

In multiple HV exposures, MAHLI images taken at very close range (target approximately 30 mm from lens) also show lath-shaped, rhomboidal and triangular shaped particles (Fig. 10), some with fills that contrast with the matrix. Particles like these were interpreted as crystal pseudomorphs and their fills at PH (Schieber *et al.*, 2022), interpreted as evaporite minerals or their pseudomorphs that formed within the shallow sediment at times of hypersalinity.

First-order interpretation of Facies F1

The substantial similarity to corrugate-weathering mudstones at Pahrump Hills (facies F1) suggests, in the absence of any contradictory observations, that F1 mudstones in the HV interval have a comparable origin. Accordingly, softer layers represent poorly cemented detrital mudstone that settled from suspension, whereas erosive features suggest a bottom current component that eroded lake

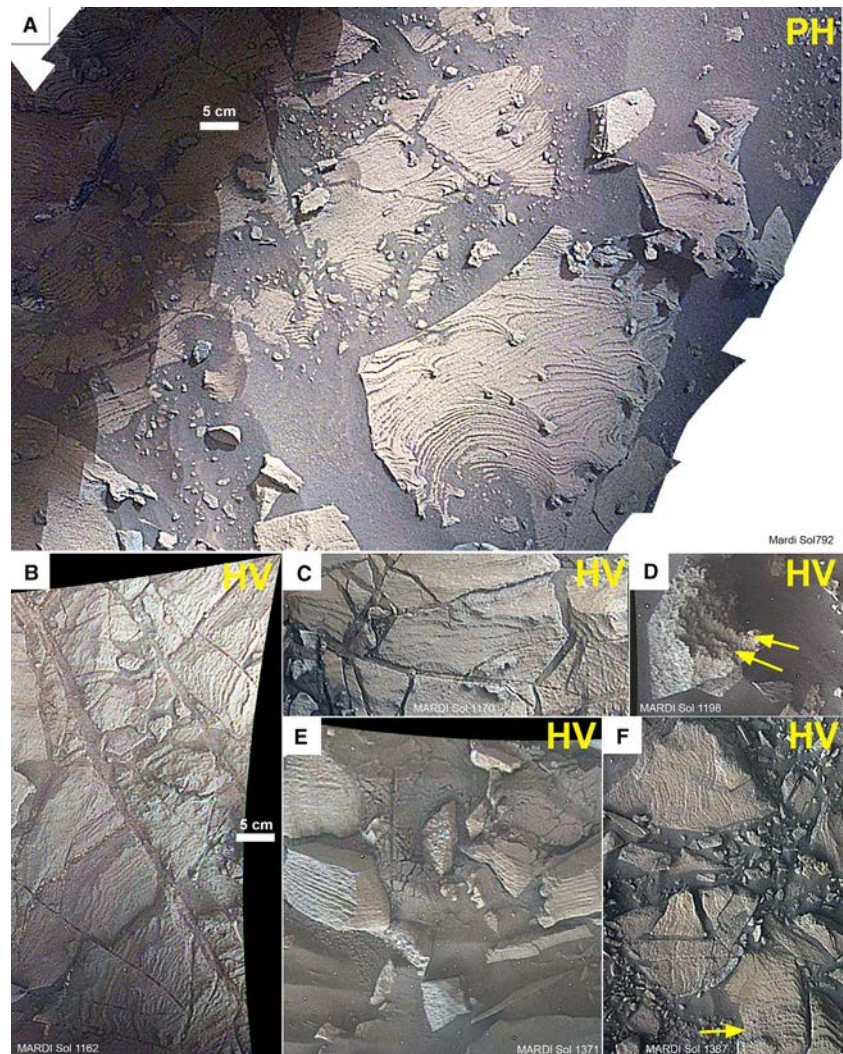


Fig. 7. Sol 729 MARDI frame (A) shows a typical expression of laminated mudstones at Pahrump Hills (PH; facies F1a from Schieber *et al.*, 2022). The rock consists of alternating harder and softer laminae. MARDI subframes (B) to (F), acquisition Sol indicated, show comparable lamina styles from the eastern and western Hartmann's Valley (HV) traverses at the same scale as frame (A). In some images, such as (D) and (F), aeolian abrasion has exposed discrete resistant objects along resistant laminae (yellow arrows).

muds and transported mud aggregates across the lake bed in bedload (Schieber *et al.*, 2022). Harder layers reflect authigenic cementation of these muds associated with evaporitic conditions that led to formation of evaporite minerals that are now preserved as sediment-incorporative crystal pseudomorphs (Schieber *et al.*, 2022).

Facies F2, smooth-weathering mudstone

Along the HV traverses, smooth-weathering F2 mudstones are exposed at multiple locations (Fig. 5) and form decimetre-scale ledges of greater erosion resistance that extend for at least several metres laterally and contain millimetre-scale sharp-sided cavities (Figs 11 and 12). Some intervals contain centimetre-scale

truncation surfaces associated with planar non-parallel steepening-upward laminae (Fig. 12D).

The outcrops of these intervals resemble facies F2 ledges at PH, especially the Book Cliffs location (Fig. 11). MAHLI images show these HV rocks to contain crystal shapes that compare closely with what was observed at Pahrump Hills (Fig. 12). Like at Pahrump, these ledges show better resistance to aeolian abrasion (relative to F1), smoother aeolian polish, variable amounts of embedded concretions, millimetre-size sharp-sided cavities that still showed outlines of pre-existing crystals and small-scale cross-bedding (Schieber *et al.*, 2022, fig. 20).

First-order interpretation of Facies F2

Based on the observations from Figs 11 and 12 and in analogy to Pahrump, the millimetre-size

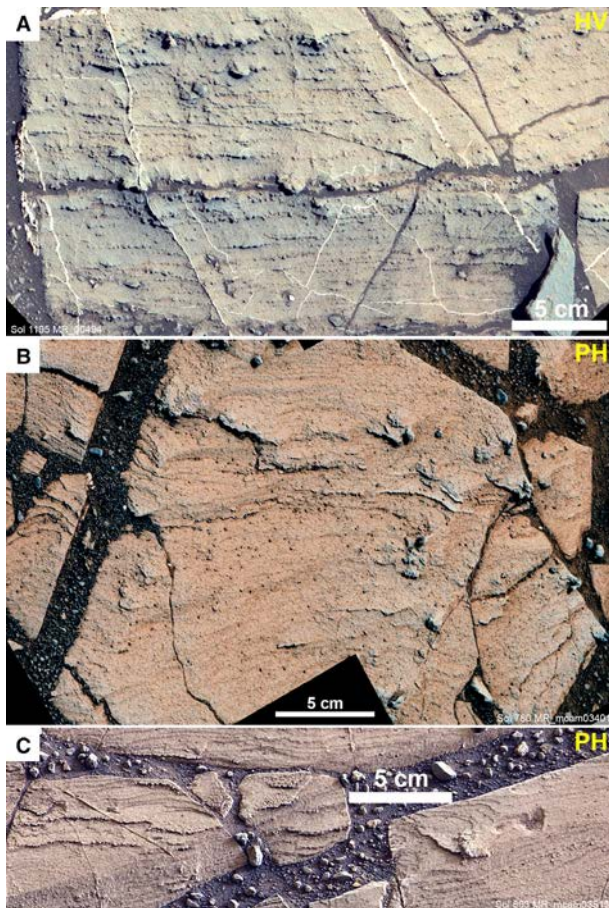


Fig. 8. (A) Typical outcrop expression of laminae at the proposed base of the Hartmann's Valley member (HV; Sol 1105). Laminae are defined by erosion resistant grains and can be traced laterally over 5 to 20 cm, giving the laminae a discontinuous character. (B) In the basal 2 m at Pahrump Hills (PH) comparably discontinuous laminae are seen, and in places there are enough erosion resistant grains available to have them develop into continuous laminae. (C) Also at Pahrump, this example shows mudstone that is dominated by mostly continuous laminae (abundant-resistant grains).

sharp-sided cavities are interpreted as testament to original crystals or crystal pseudomorphs. As postulated for F2 at Pahrump, crystal pseudomorphs in F2 ledges may have originated as a consequence of dissolution–reprecipitation of finer evaporite particles (due to cumulate accumulation; Smoot & Lowenstein, 1991), growing as sediment-incorporative (poikilotopic) crystals in mud layers that acted as a three-dimensionally isotropic medium. Intervals with truncation surfaces and cross-bedding indicate erosion of surface muds, generation of mud

aggregates and currents capable of forming ripples (Schieber *et al.*, 2010; Schieber, 2011), probably due to the interaction of currents and waves with the lake bed (Kelts & Hsü, 1978; Smoot & Lowenstein, 1991).

At Pahrump Hills, the erosion resistance of these layers was attributed to a combination of early diagenetic cementing agents, including opal-CT, Fe-oxides and allophane/imogolite (Schieber *et al.*, 2022), and the same interpretation is adopted for smooth weathering mudstone beds in the Hartmann's Valley interval.

Facies F5, cross-bedded sandstone

Along the western HV traverse (Fig. 1), rocks with decimetre-scale cross-stratification were observed at the Sol 1378 rover location at an area named Baynes Mountain (Fig. 13). The particle size of these rocks was not documented. No outcrops with similar cross-bedding were observed along the eastern HV traverse. Because decimetre-scale cross-stratification is not usually observed in mudstones (Schieber, 1998; Schieber *et al.*, 2019), and is comparatively easy to see at a distance in sandstones, the authors consider the Baynes Mountain cross-stratification as an indicator of sandy strata. The well-defined cross-bedding and variable resistance of the laminae to weathering suggests the additional presence of some finer-grained sediment.

Along the western HV traverse, discontinuous resistant features observed from a distance (Fig. 14) are interpreted as sandstone lenses, analogous to Whale Rock and Newspaper Rock at Pahrump Hills (facies F5a; Schieber *et al.*, 2022).

In one location (Sol 1386), where a small crater afforded steep exposures of HVi strata, a closer view of these resistant layers was possible (Fig. 15). Even though the MastCam resolution for this image is 0.22 mm/pixel (insufficient for differentiation of mudstone versus sandstone), the fractured rock surface shows a roughness that is unlike that seen in adjacent mudstones, suggesting a coarser lithology, probably sandstone. Figure 15 shows examples of these presumed sandstones that show internal lamination, cross-stratification and, in places, truncation surfaces and current-ripple cross-lamination.

Whereas the observed rock bodies show the general characteristics (laterally discontinuous, lens-shaped geometry, cross-bedding) that were observed in association with sandstone lenses in

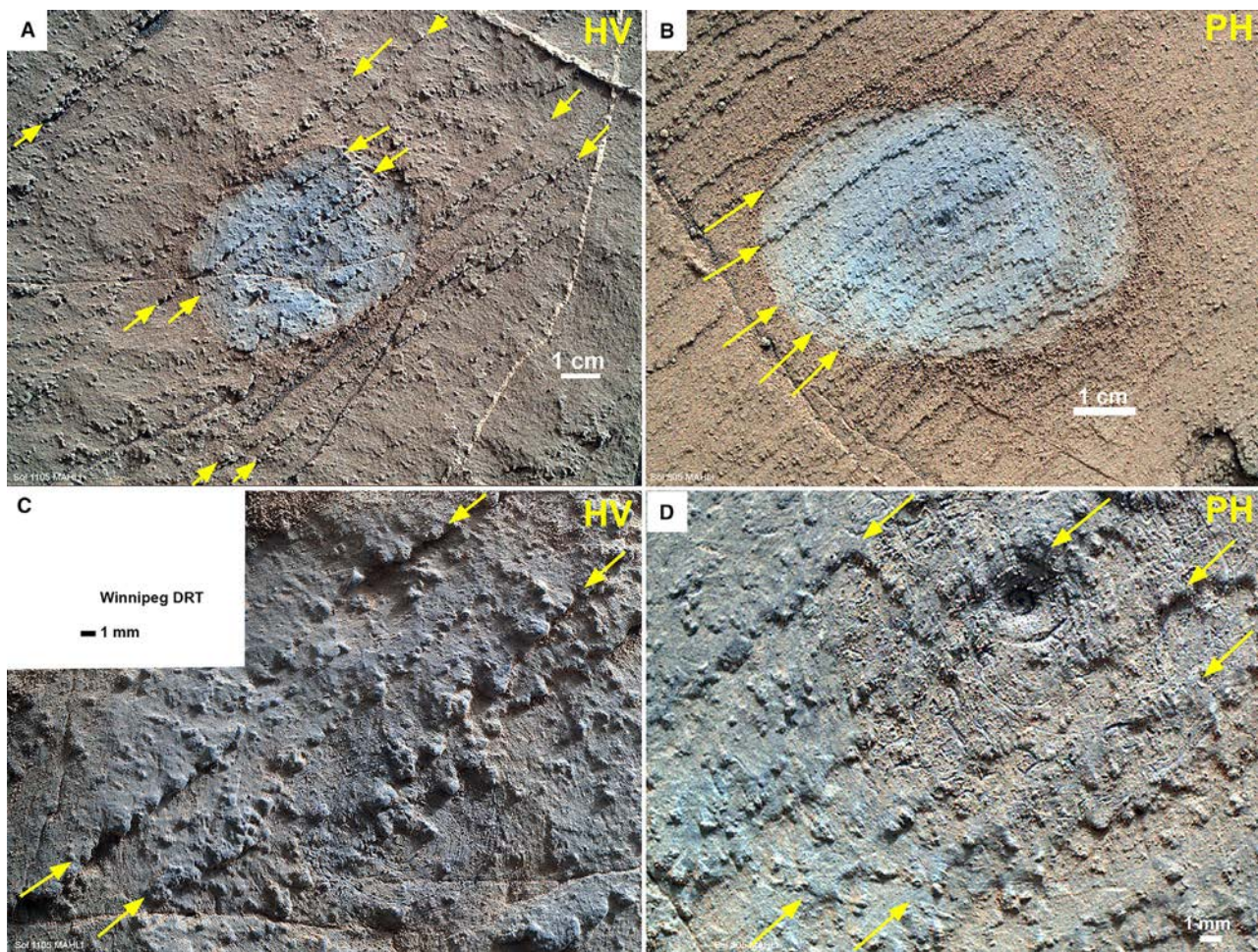


Fig. 9. Images on the left side (A) and (C) show erosion-resistant laminae at target Winnipeg in the Hartmann's Valley interval (HVi), Sol 1105 location. For comparison, images (B) and (D), displayed at the same scale, show erosion-resistant laminae at target Pelona at the Sol 805 location in Pahrump Hills.

the Pahrump Hills interval (Whale Rock, Newspaper Rock, etc.; Schieber *et al.*, 2022), at Baynes Mountain there is an additional intriguing association of the cross-bedded lens shown in Fig. 13 with thinner, laterally extensive (presumed) sandstone beds (Fig. 16).

First-order interpretation of Facies F5

Just as at PH, the general interpretation of cross-bedded lenses (presumed to be sandstone) in the HV interval is that they record fluvial channels incised into lacustrine mudstones associated with times when lake levels dropped. Whereas these channels probably received some sand infill associated with lake lowstands, complete infill probably reflects increasing stream flow and enhanced sediment transport during

subsequent rises of lake level (Bohacs *et al.*, 2000, 2003). In this context, the sandstone beds extending away from the main sandstone lens at Baynes Mountain (Fig. 16) can be interpreted as overbank-flow/crevasse splay deposits that were shed away from the main channel during peak flow episodes (Schumm, 1977, 1981; Campo *et al.*, 2022).

Facies F6, undulose bedded mudstone

The undulose bedded mudstone facies (F6) comprises those exposures along the Hartmann's Valley traverse where variable and shallowly inclined dips are visible over lateral distances of tens of metres, as in Fig. 17, and in other areas marked as F6 with polygons in Fig. 5. In places

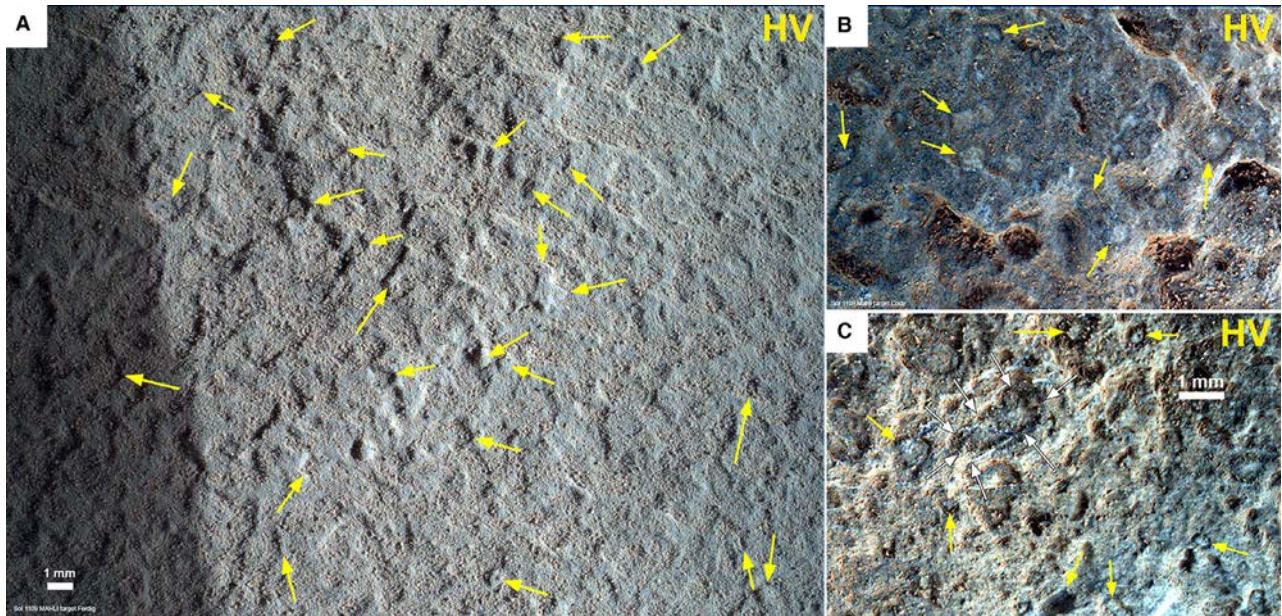


Fig. 10. Examples of crystal shapes in Hartmann's Valley interval (HVi) laminated mudstones. (A) Target Ferdig (Sol 1109), though somewhat dusty, shows multiple geometric shaped pits and surface features (lath, rhombic, triangular; yellow arrows). (B) and (C) are close-up images from target Cody (Sol 1109) that show rhombic shaped features (yellow arrows) that differ in colour (lighter) from the surrounding mudstone matrix. An exceptionally large example is marked by white arrows. These closely resemble F1 examples shown in figs 10, 11A and 17 in Schieber *et al.*, 2022.

these multi-decimetre-scale shallowly dipping layers are clearly seen as continuous and convex-up across the crests of metre-scale anticlinal/roll-over features (Fig. 18); HoloLens observations suggest long-axis azimuths between 180 and 210 degrees (north–south to south/south-west – north/north-east) for these convex-up features. Beds mostly dip to the east and west, generally perpendicular to the long axes of the convex-up structures, and at dip angles that are well below the angle of repose of sand in air. The lamina geometries within most of the beds appear to be planar and parallel to the bed-bounding surfaces. Some F6 layers show decimetre-scale intervals with higher-dip-angle curved non-parallel laminae that lap down onto their basal larger-scale bed surfaces (Fig. 19).

The essential characteristics of the F6 undulose bedded mudstones, such as variable and opposing dips and convex-up structures are best observed from a distance at a low viewing angle (where the strata are at ‘eye’, or camera, level). In the rover vicinity (a few metres distance), when the viewing geometry is at a comparatively steep angle relative to bedding, these

features are not apparent and thus there is some uncertainty with regard to positive identification of occurrences of facies F6. After careful consideration of imaged areas in which facies F6 occurs (Fig. 5), relative to rover stops and close-up MAHLI imaging, it appears that the MAHLI target Swartkloofberg (Sol 1162 location, eastern traverse; images collected on Sol 1167) most likely shows an example of these undulose bedded mudstones. These MAHLI images were collected in the middle of a stretch of the eastern traverse where F6 dominates (Fig. 5), and rocks with ‘undulose’ attributes appear to extend without obvious interruption towards the rover’s location (Fig. 19).

The near-rover outcrop view of this material is shown in Fig. 20, where it exhibits millimetre-scale lamination that is more subtle in expression than the distinct corrugate laminae of facies F1 (Fig. 7) and also lacks the preferentially cemented lamina, small nodules and crystal shapes of facies F1 (Fig. 8).

At Gale crater aeolian abrasion is the dominant modern modus of outcrop erosion, and enhances subtle textural details of the eroded

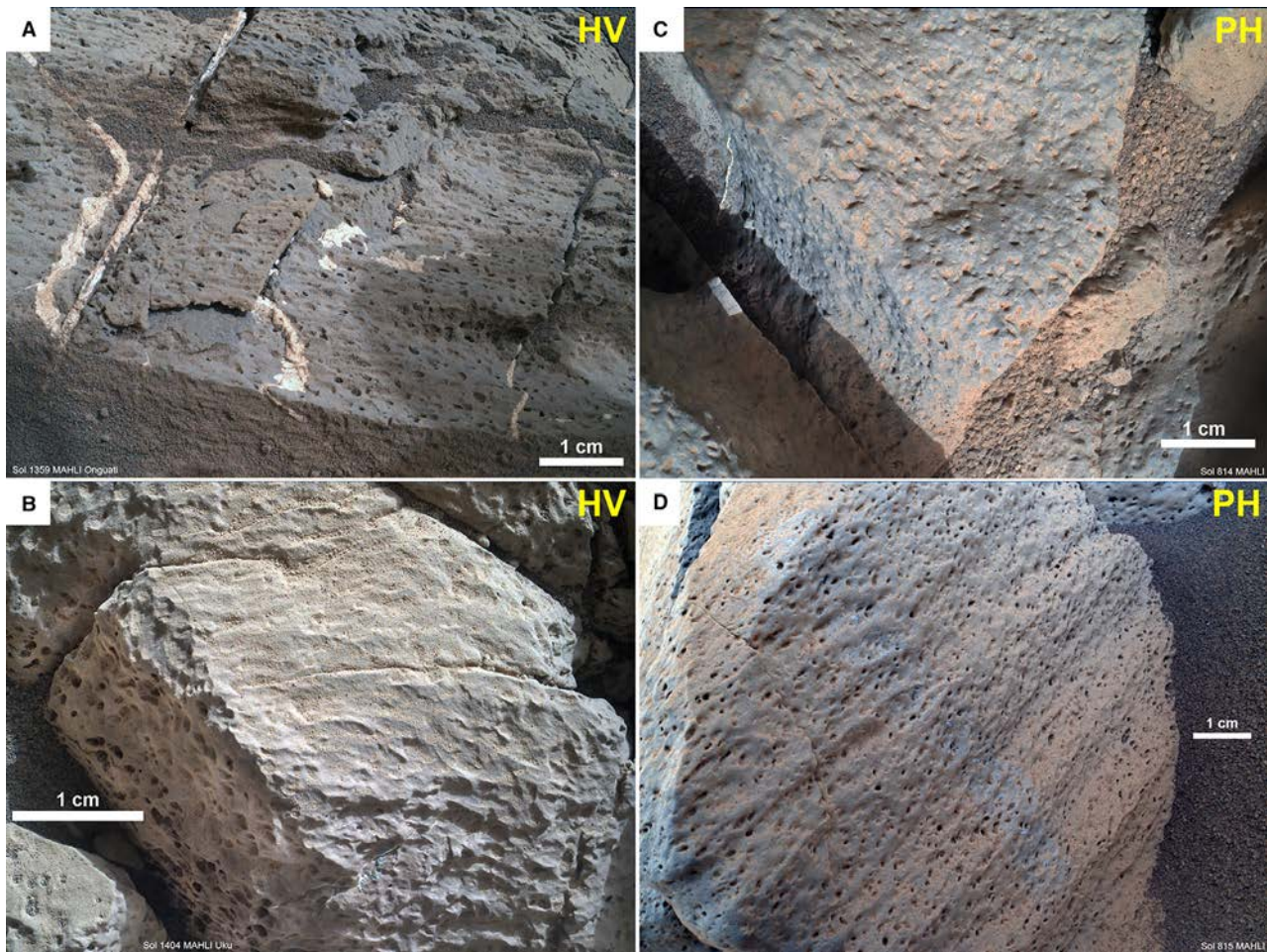


Fig. 11. Comparison of smooth-weathering, cavity-rich mudstones from Hartmann's Valley [HV; images (A) and (B); Sol 1369 target Onguati and Sol 1404 target Uku] with examples from Pahrump Hills (PH) – images (C) and (D). The rock matrix is comparable in grain size to F2 at Pahrump, and the shape and size of holes suggest once embedded sand size objects.

rocks (Schieber *et al.*, 2020). At Swartkloofberg it produced a stepped pattern of laminae (Fig. 20), and careful examination of the highest magnification images (Fig. 21) suggests a mudstone with an appreciable coarse silt component. This range of grain sizes, along with the general lack of F1 or F2 characteristics and its larger-scale undulose bedding led the authors to interpret these rocks as a different facies, F6.

First-order interpretation of Facies F6

The F6 intervals lack pervasive and widespread stratal terminations that characterize cross-bedding, especially at the decimetre to metre-scale (Campbell, 1967; Rubin, 1987). The smaller-scale cross-bedding in some intervals is confined to layers that are continuous over the

crests of the convex-up features (Fig. 18). The interbedding of decimetre-scale high-angle cross-beds with metre-scale low-angle continuous parallel beds is most characteristic of subaqueous deposition (Reineck & Singh, 1980), and not widely reported from purely aeolian strata (Rubin & Hunter, 1983; Rubin, 1987). The consistent azimuths of the long axes of the convex-up features, the consistent strikes of the larger layers on their limbs, and the widespread occurrence of F6 (Fig. 5) are also inconsistent with an origin by slumping and soft-sediment deformation or impact deformation (Kenkmann *et al.*, 2014; cf. Edgar *et al.*, 2018).

The F6 intervals are considered the record of distal subaqueous mudstone tongues in a pro-delta setting, connected to streams that supplied

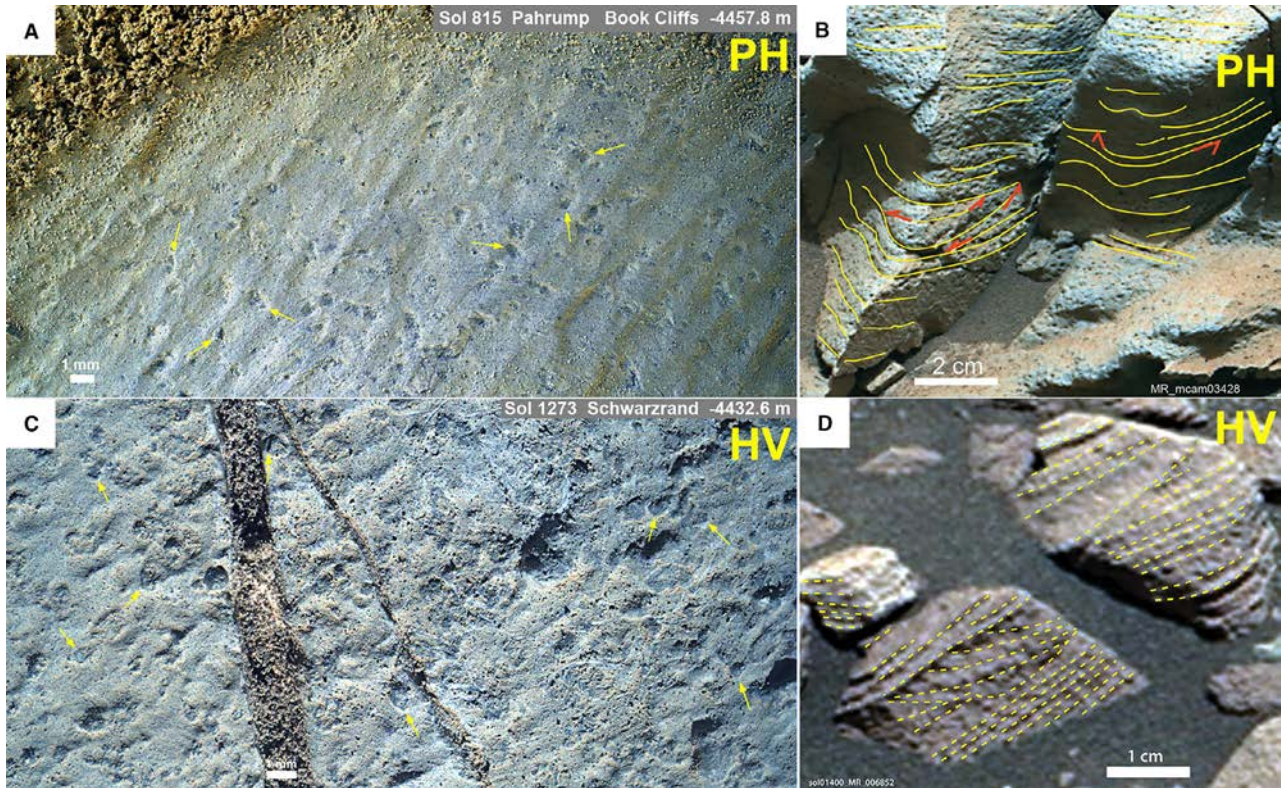


Fig. 12. Comparison of DRT (dust removal tool)-brushed and aeolian-abraded mudstones from Pahrump Hills (PH; upper images) and Hartmann's Valley (HV; lower images). Images (A) and (C) show a wide variety of crystal shapes (interpreted as evaporite pseudomorphs; Schieber *et al.*, 2022), that are either flush with or standing slightly above the abraded surface. Some euhedral examples are marked with yellow arrows. Images (B) and (D) show internal truncation surfaces, scouring and cross-lamination.

sediment to the lake. The azimuths of anticlinal features along both the eastern and western HVi traverse (Fig. 18) are consistent with sediment introduced by streams from the north and the detailed palaeogeography interpreted from Pahrump Hills exposures (Schieber *et al.*, 2022, fig. 41). Dip variations across broad fields of view (Figs 17 and 19) may reflect stacked prodeltaic mud lobes that prograded into the lake as sediment-rich suspensions were injected along the lake margins. The larger-scale convex-up geometry and variable but lower-angle dips record the overall undulating bathymetric configuration of these subaqueous tongues. The latter are considered expressions of depositional lobes and are discussed further in the next section in the context of Earth analogues. The smaller-scale cross-stratification that occurs in some of the F6 layers (Fig. 19) may represent mesoscale bedforms composed of mud-dominated composite particles (Schieber

et al., 2019; Li *et al.*, 2021), filling locally rugose bathymetry (e.g. Johnson & Graham, 2004). Alternatively, these smaller scale, higher angle cross-strata might record episodes of persistent sediment transport across the tongues, probably as subaqueous-dune-scale bedforms from concentrated/winnowed silts (Southard & Boguchwal, 1990). The intercalation of planar bedding with smaller-scale cross-beds records alternating benthic-energy levels, potentially related to flood influx, relaxation and fair-weather conditions.

Earth analogues for facies F6

The undulose geometry of F6 appears to record a lake floor with undulating bathymetry. Non-flat and non-smooth but undulating lake floors are quite common in modern lakes on Earth, particularly in underfilled lake systems (Gierlowski-Kordesch & Kelts, 1994, 2000;

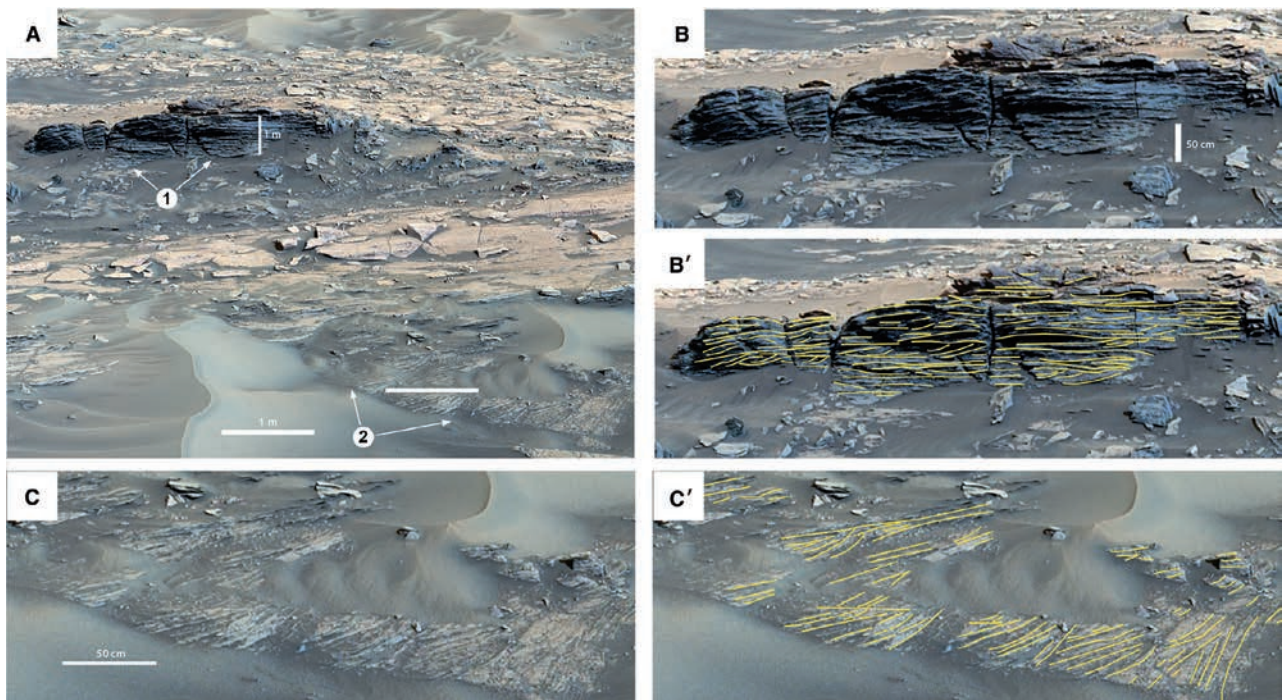


Fig. 13. Detail from Sol 1381 Mastcam Baynes Mountain mosaic (ML_006768). (A) Shows outcrop overview of cross-bedded scarp (marked '1') and a horizontal exposure of cross-bedded strata (area marked '2'). (B) An enlarged view of the cross-bedded scarp in area '1'. (B') Same area as (B), but with bedding traced out with yellow lines. (C) An enlarged view of the cross-bedded strata from area '2', exposed between modern, light grey, aeolian bedforms. (C') Same area as (C), but with bedding traced out with yellow lines. This type of texture (rib and furrow structure) suggests horizontal erosion of a trough cross-bedded sandstone (Campbell, 1967).

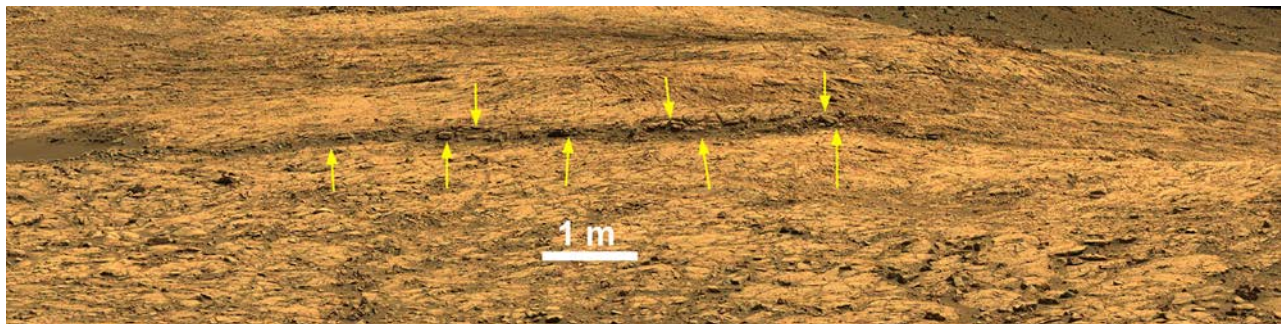


Fig. 14. Potential erosion-resistant sandstone lens within mudstone strata is marked with yellow arrows. Mastcam mosaic acquired from the Sol 1384 rover location.

Cohen, 2003), such as illustrated in Fig. 22. Comparable depositional topographies also occur in modern coastal lakes that are infilled by mud-dominated subaqueous deltas (e.g. Shaw *et al.*, 2016; Whaling, 2018).

The present-day bathymetry and recent lake deposits of Lake Bogoria, Kenya, provide another

pertinent example of non-flat lake floor topography (Hickley *et al.*, 2003; De Cort, 2016) (Fig. 23). Located in the eastern Rift valley of Kenya, it is an underfilled-discharge alkaline-hypersaline lake system (Benavente and Bohacs, 2024), supplied by perennial springs and seasonal fluvial input (Cioni *et al.*, 1992; Hickley *et al.*, 2003). Although

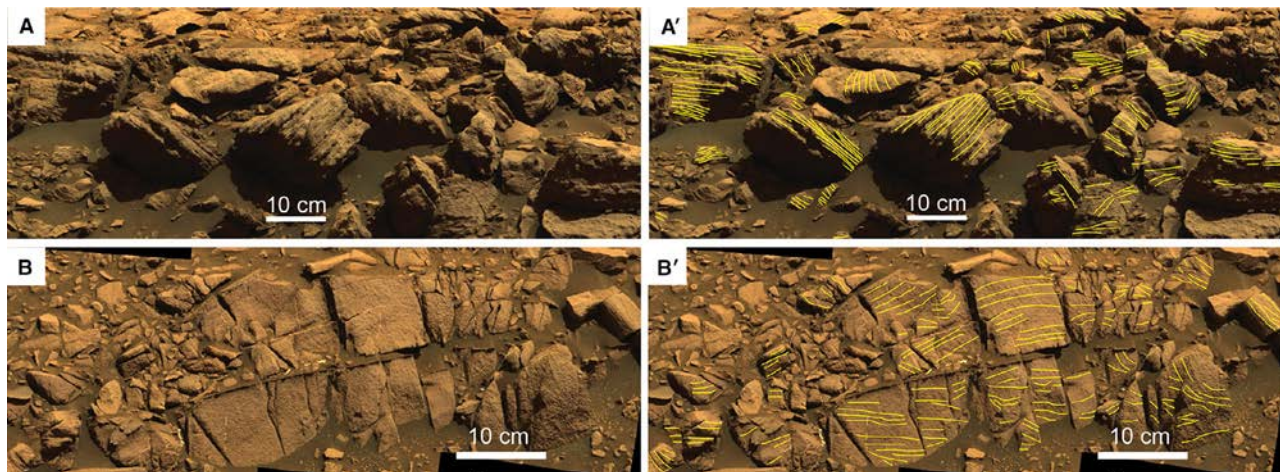


Fig. 15. Detail of presumed sandstone outcrops at the Sol 1386 location. Image (A) shows MastCam target Hardap, and (A') shows the same location with yellow lines that mark bedding features. Image (B) shows MastCam target Hochfeld, and (B') shows the same location with yellow lines that mark bedding features.

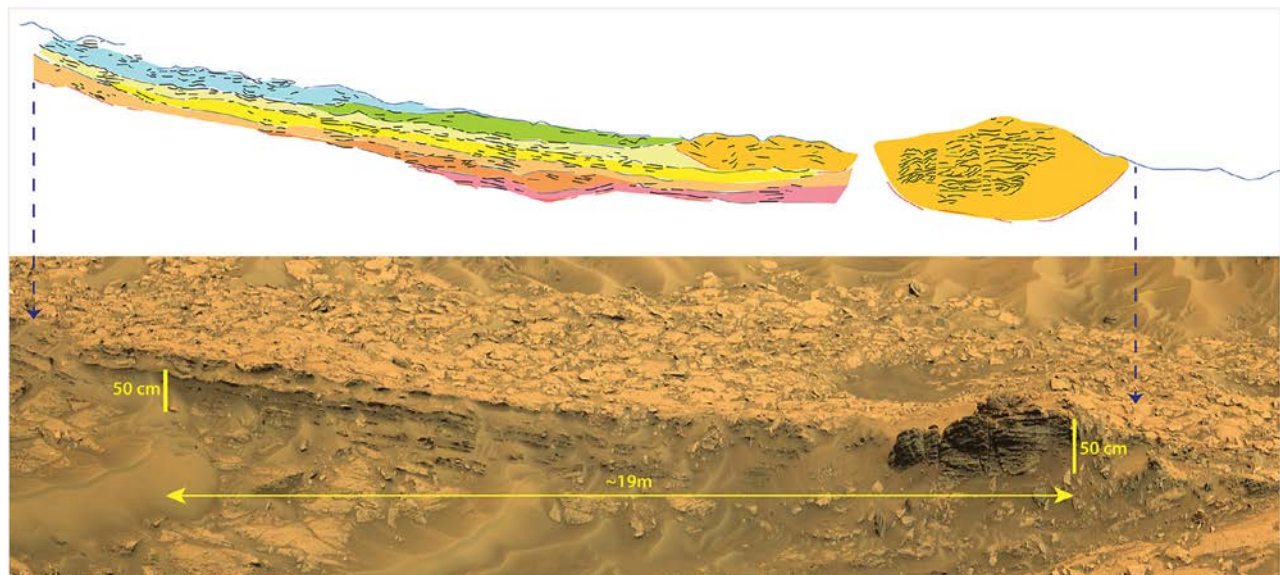


Fig. 16. At the bottom a vertically exaggerated ($2\times$) view of the Baynes Mountain sandstone lens (at the right; see Fig. 13) and a laterally equivalent package of even-bedded sandstone (to the left) exposure. Above an interpretive sketch shows lateral facies relations and their presumed relative ages (main channel – orange; lateral beds to left are coloured in stratigraphic order from red to blue). The lateral beds at the left are interpreted to represent overbank deposition from the main channel at the right.

most of the lake floor is relatively smooth (local relief ≤ 0.5 m; Hickley *et al.*, 2003), in certain areas lake-floor undulations of up to 2.5 m relief and 100 to 200 length occur in water depths of 6

to 12 m offshore of stream input points. The upper metre of lake-centre deposits is silt dominated; one metre below the lake floor evaporite-bearing interbeds (centimetre to decimetre-scale)

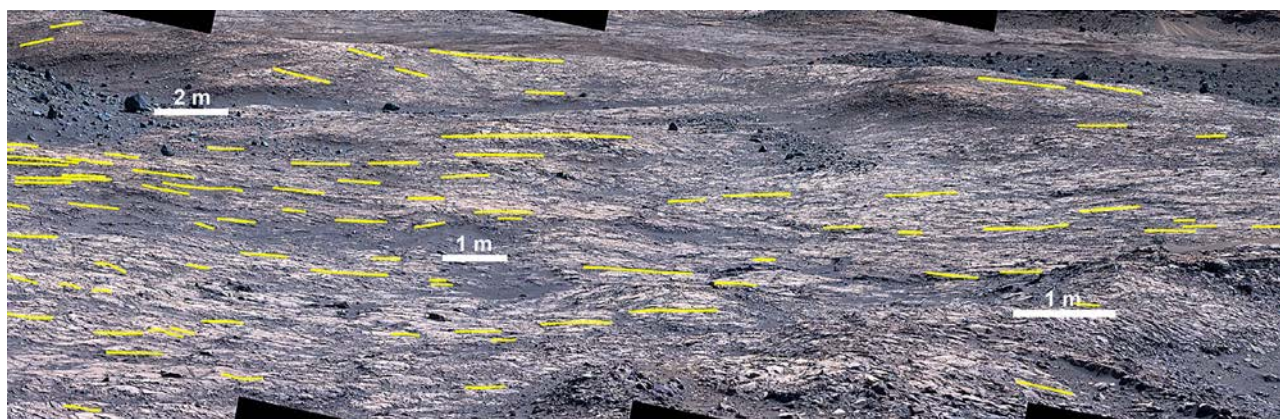


Fig. 17. Undulose bedded mudstone with variable apparent dips of beds, marked with yellow lines. Sol 1387 Mastcam mosaic ML_006817.

occur due to early diagenetic mineralization (2000 years old or younger; De Cort, 2016). Hickley *et al.* (2003) considered the undulose topography to be the cumulative outcome of clastic sediment supply via shoreline deltas, dispersal across prodelta lobes, reworking by storm-induced currents and frequent changes of lake level. Evaporites accumulated during short-lived lake-level lowstands.

The metre-scale undulose bathymetry and associated strata of the modern Lake Bogoria underfilled-lake system corresponds in scale and geometry to the undulating F6 mudstone facies in Hartmann's Valley. The added observation of actively cementing evaporite interbeds (similar to F1 and F2 herein) is another parallel that gives credence and feasibility to this current interpretation of the HV lacustrine mudstone succession.

Comparable stratal geometries have also been observed in ancient lake deposits on Earth (Figs 24 and 25), such as the Upper Jurassic Har Hotol synrift strata of Mongolia (Johnson & Graham, 2004), the Eocene Green River Formation, USA (Stanley & Surdam, 1978) and Lake Lisan (Dead Sea; Inbar, 1987; Hall, 1996).

Hartmann's Valley interval facies summary

The Hartmann's Valley interval (HVi) continues a sedimentary regime that had been established in the underlying Pahrump Hills interval. Corrugate-weathering (F1) and smooth-weathering (F2) mudstone facies dominate the succession, with a poorly sorted

detrital silt matrix and sand-size pseudomorphs of evaporite minerals that likely formed on and within lake-floor sediments (Schieber *et al.*, 2022). Although exposures are rarely of the quality and continuity to clearly identify stratigraphic discontinuities, intermittent lenses and channels filled with cross-bedded sandstone (facies F5) can be interpreted as Lowstand Systems Tracts (Schieber *et al.*, 2022), and indicate that lake levels and salinities likely fluctuated and imprinted the accumulating muds with episodic accumulation of authigenic minerals that gave rise to the observed millimetre-scale (evaporite-rich laminae), centimetre-scale (concretions) and metre-scale bedding (top-cemented parasequences). The newly observed facies element F6, undulose bedded mudstone, likely represents subaqueous prodeltaic mud tongues that extended into the lake basin from river deltas along the margins of the lake. This facies was recognizable in the HV interval because F6 forms packages several metres thick. Had only occasional beds or thin intervals of F6 been present, it is likely that it would not have been recognized as such. It is therefore quite possible that F6 beds are present in the PH interval as well, but were not recognized because they were too thinly developed or poorly exposed (as in the interval below Sal-sberry Peak; Schieber *et al.*, 2022). The 'difference' between PH and HV in terms of relative abundance of sedimentary facies may simply be a fortuitous byproduct of the choice of rover traverse. This is a phenomenon familiar

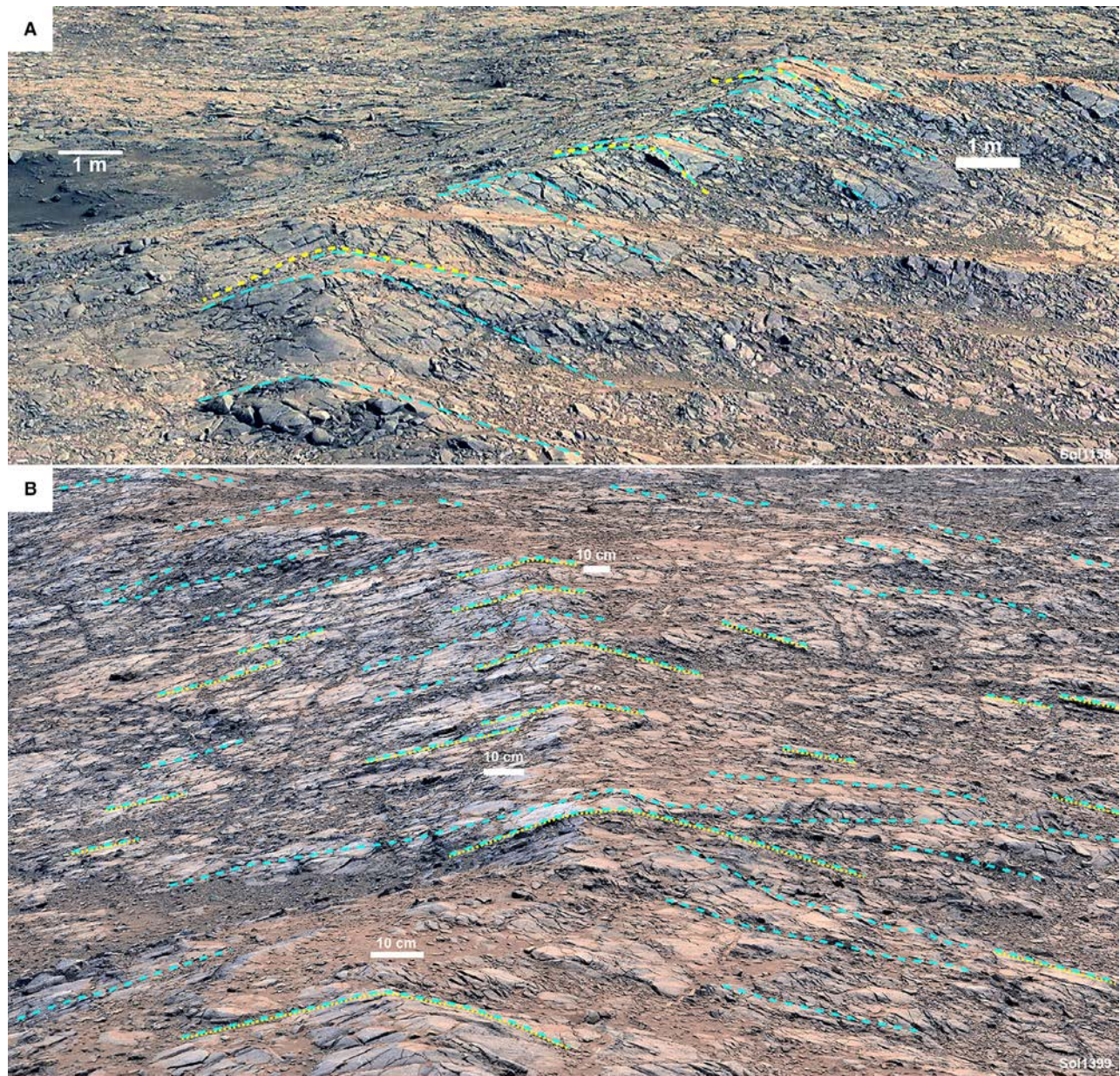


Fig. 18. Undulose mudstone facies (F6) imaged from (A) the Sol 1158 location along the eastern Hartmann's Valley (HV) traverse, and (B) the Sol 1399 location along the western HV traverse. Dashed yellow and turquoise lines mark rollovers across the crests of continuous convex-up layers. HoloLens observations suggest a long axis azimuth between 180 and 210 degrees for the crests of these features. Because image interpretation is subject to subconscious biases of the observer (Schieber & Shao, 2021), two of the authors (JS & KB) traced out the perceived convex layers independently (the yellow and turquoise dashed lines) for the sake of cross-validation. The two sets of lines are in close agreement.

to sedimentary geologists working on Earth, namely that one can measure multiple sections across the same escarpment, or up various

sides of the same mountain, and end up with distinctly different stratigraphic sections, signifying lateral facies change in a broader setting.

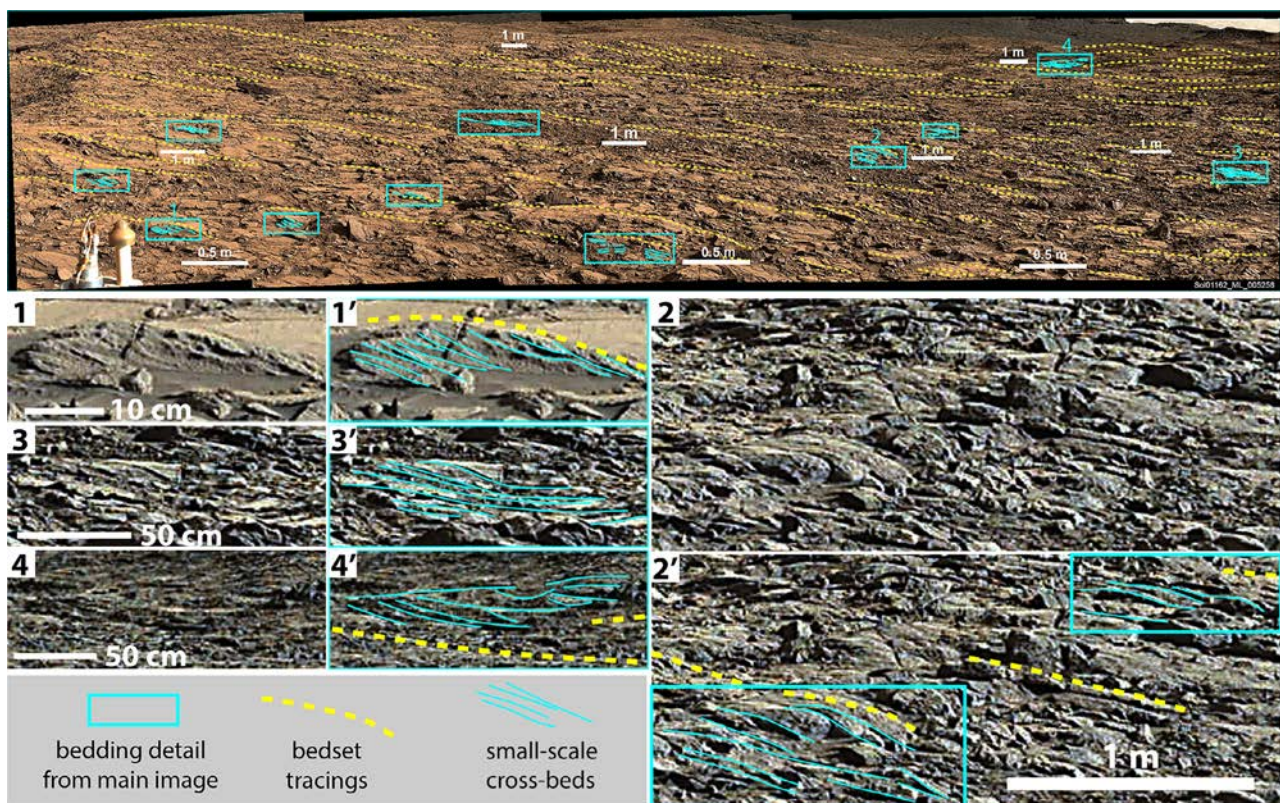


Fig. 19. Undulose bedded mudstone (top image), looking southward from the Sol 1162 location. The Sol 1167 MAHLI observations of target Swartkloofberg (Fig. 20) were made at this location. Top image shows typical outcrop of undulose bedded mudstone with bedsets highlighted by dashed yellow lines. Blue rectangular boxes mark areas where low angle cross-stratification (blue lines) is visible. Five of these boxes are shown underneath in enlarged form with cross-stratification marked with blue lines. They correspond to areas in the top image that are numbered 1 through to 4 (with area 2 showing two boxes), and the enlargements consist of the original image (contrast enhanced, labelled “1, 2, … etc.”) and a companion image where cross-strata are marked with blue lines (labelled “1’, 2’, … etc.”). Portions of Sol 1162 Mastcam mosaic ML_005258.

STRATIGRAPHIC SUCCESSION AND LATERAL FACIES DISTRIBUTION – PHYSICAL SEDIMENTOLOGY AND STRATIGRAPHY

The observed facies do not occur randomly across the Hartmann’s Valley outcrop area, but show ordered vertical successions. With an east–west separation of approximately 700 m between the two traverses, the distinct differences between their vertical facies successions (Figs 5 and 26) are an indication of lateral changes in depositional conditions.

The western traverse spans the larger range of elevation and the widest variety of facies and facies stacking. The lowermost 7 m interval (Fig. 26) consists of interbedded decimetre-scale intervals of F1 and F2 mudstone facies, and

resembles the basal 6 m of the Pahrump section (Schieber *et al.*, 2022). In addition, panoramic images reveal discrete multi-decimetre resistant intervals that are interpreted as lenses of F5a sandstone. A thicker interval of cross-bedded F5b sandstone occurs between –4429 m and –4428 m at the Baynes Mountain location (Fig. 13). This interval appears to have a wavy top, with up to 30 cm relief over a few metres laterally, and decimetre-scale bedsets of sandstone or muddy sandstone which appear to be laterally associated with the main F5a sandstone body (Fig. 16). Bedsets stack in a progradational pattern and contain centimetre to decimetre-scale planar-parallel and cross-beds.

The overlying 1 to 2 m western traverse interval contains interbedded F1 and F2 mudstones, and is in turn overlain by about 6 m of dominantly

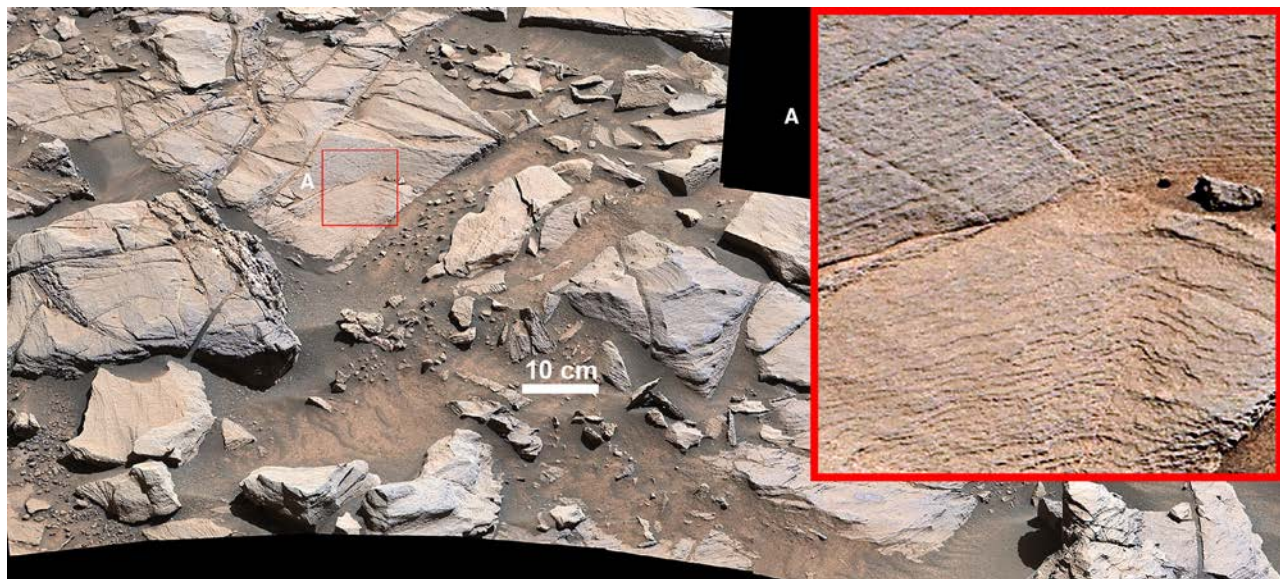


Fig. 20. Outcrop image in rover vicinity from the Sol 1162 rover location. MAHLI target Swartkloofberg is located just a few centimetres below the lower edge of the image (obstructed by rover hardware). Image taken on Sol 1166 (MR_005275). Red framed inset (A) (10 cm by 10 cm; upper right) shows an enlarged version of red frame (A) (upper left) to illustrate bedding.

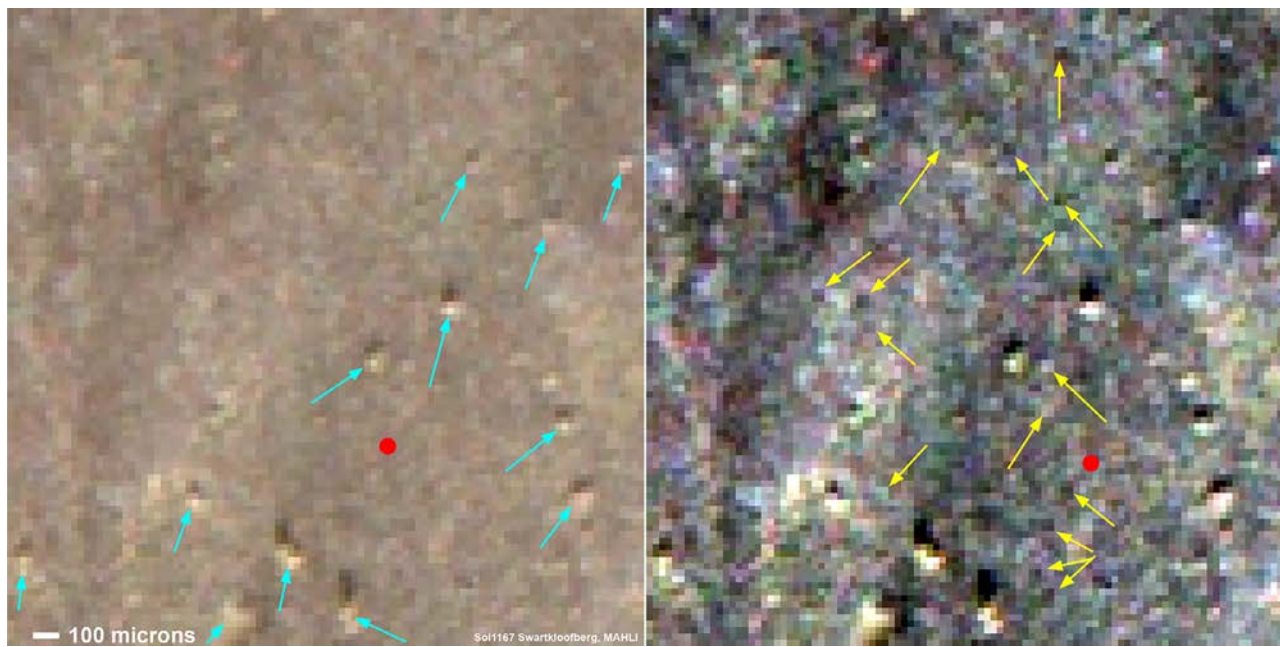


Fig. 21. MAHLI close-ups from target Swartkloofberg (Sol 1167) at high magnification. At the left, a 100 pixel by 100 pixel area from a spot that is largely free of surface dust (blue arrows indicate dust grains or aggregates). Scale bar at lower left, red dot is 63 microns in diameter, the maximum size of mudstone particles. At the right, same field of view but strongly contrast enhanced. The surface dust grains/aggregates are clearly visible, and the surface generally shows RSPVV ‘pixel salad’ texture, a sign that the rock has a finer mudstone matrix (Schieber, 2018). Coarse silt particles are scattered through this matrix (yellow arrows point to examples), and appear more common than in other Hartmann’s Valley mudstones (see below).

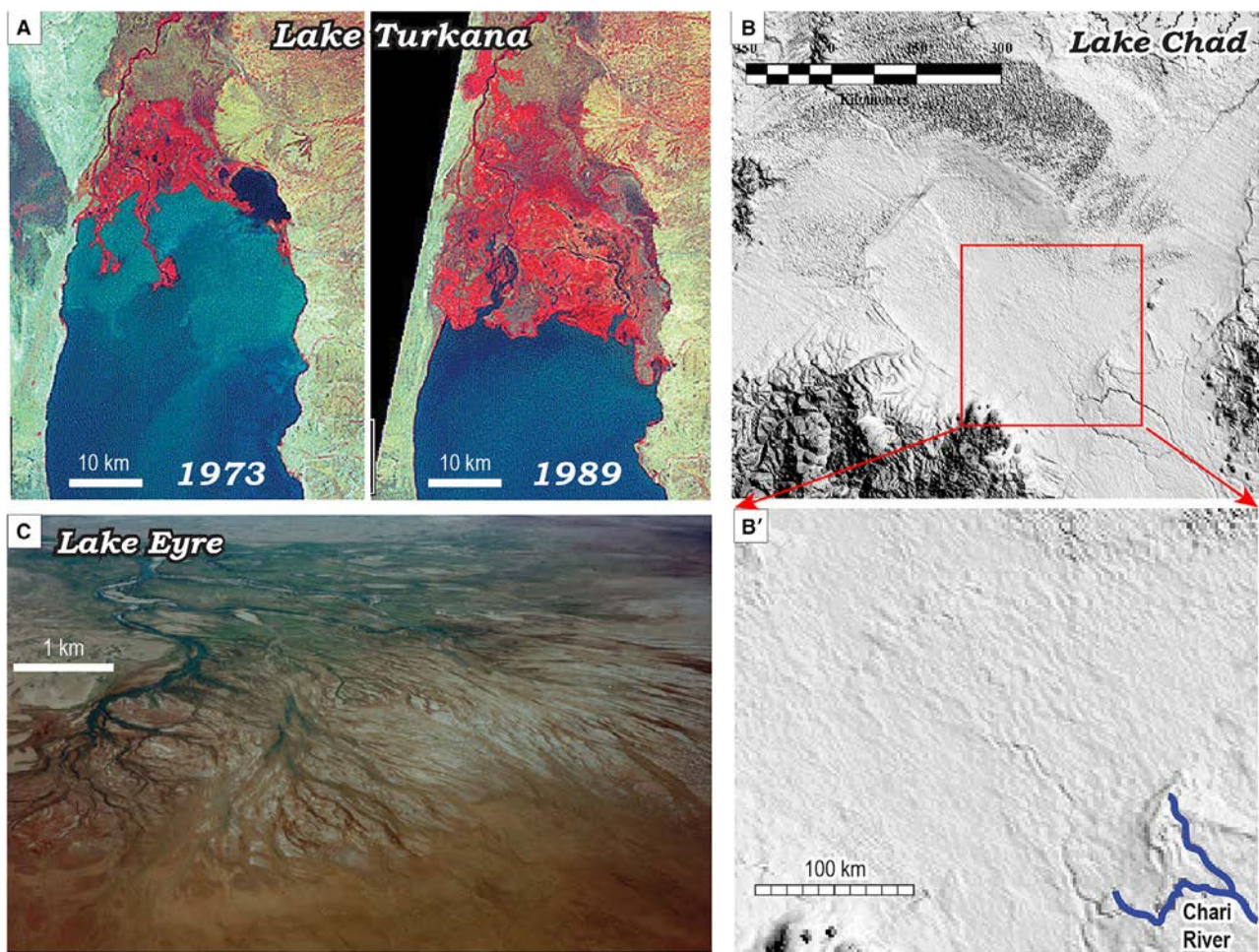


Fig. 22. (A) Lake Turkana (Kenya), over time, provides an Earthly example of infilling of a lake by fluvio-deltaic processes. Hues of red indicate the undulating topography of a highly dynamic landscape. The 1989 image shows the lake-floor topography that was submerged in 1973 (USGS, 1989, EROS History Project; <https://www.usgs.gov/media/images/1989-landsat-mss-lake-turkana>; accessed 31 January 2024). (B) and (B') The dry lakebed surface of Lake Chad displays undulose topography at the kilometre scale (image courtesy of Dr David Reynolds based on NASA Shuttle Radar Topography Mission data). (C) A view of the Neales delta along the shores of Lake Eyre, Australia. When Lake Eyre floods all of this undulose channelled topography is submerged (image courtesy of Dr Simon Lang; see also Lang *et al.*, 2004).

facies F6 (−4427 to −4421 m) which appears to host a few multi-decimetre-thick lenses of F5a sandstone. Although most of these lenses are seen from a distance (for example, Fig. 14), when seen from closer range (Figs 13 and 15) they show cross-bedding typical for F5a. Another interval of dominantly interbedded F1 and F2 occurs from −4421 to −4418 m, which is followed by another thick interval dominated by F6 (Fig. 26). The interpreted contact with the overlying Karasburg member (Fig. 2) is not well-exposed and placed here at the elevation previously proposed (e.g. Gwizd *et al.*, 2022).

The eastern traverse (Fig. 26) shows similar facies and thicknesses of facies intervals, but at different elevations, resulting in a visibly different stratigraphic pattern. The eastern Hartmann's Valley section is also significantly thinner than its western equivalent, most likely due to uneven erosion that removed the upper portion of the HV interval prior to the unconformable emplacement of the overlying Stimson sandstone. Although it is difficult to confidently assess relative proportions of F1 and F2 in the upper part of the remaining section (−4426 to −4419 m) owing to the shallow slope of the

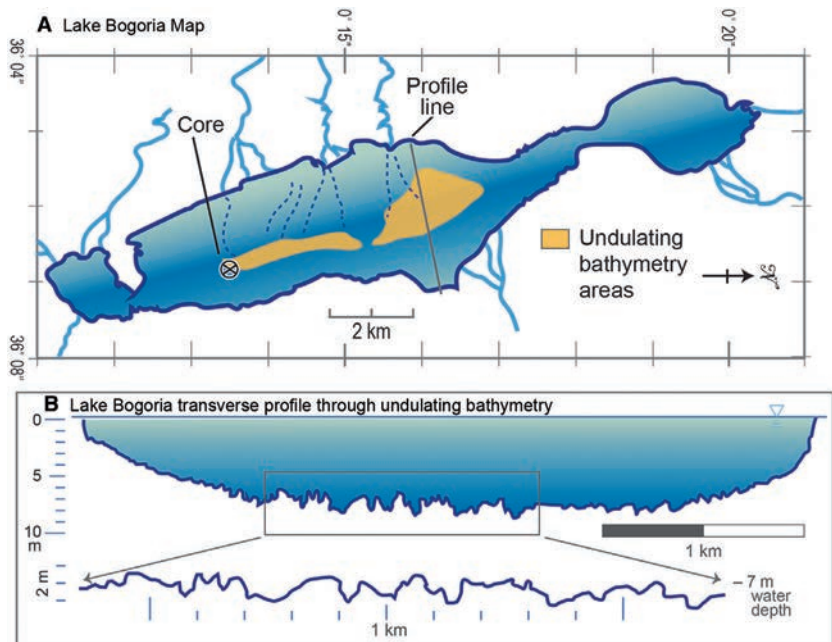


Fig. 23. (A) Map of Lake Bogoria, Kenya, noting points of fluvial sediment supply and occurrence of undulating lake bed topography. (B) Detailed view of bathymetry along the profile line from (A). After Hickley *et al.* (2003).

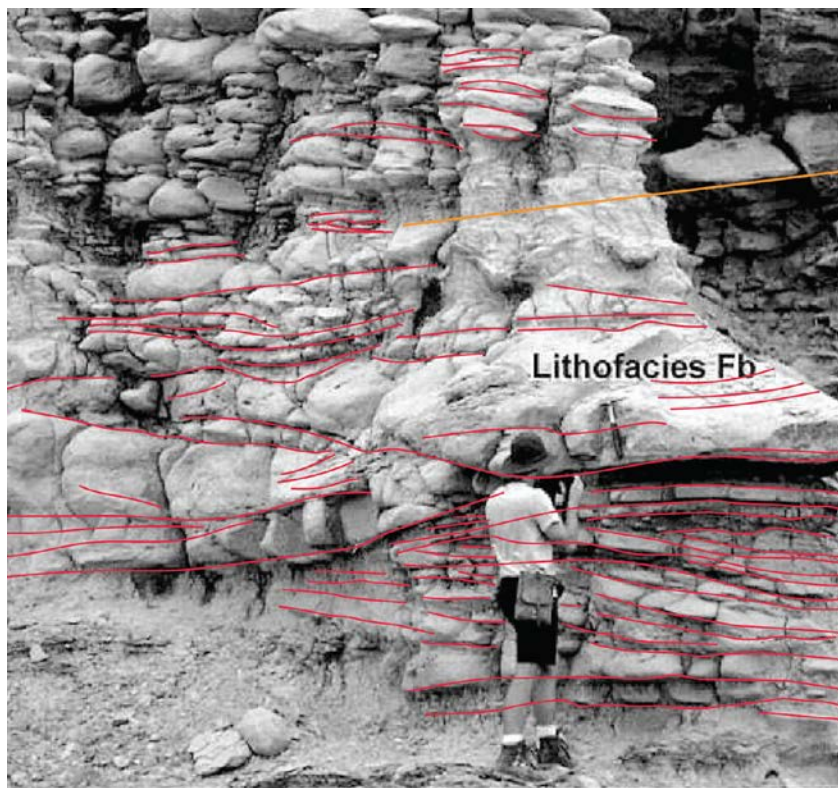


Fig. 24. Prodelta-marginal lacustrine strata from Har Hotol in Mongolia. This outcrop shows lithofacies Fb, centimetre to decimetre-scale interbedded grey siltstone and claystone that show minor erosional surfaces and inclined strata. Base image from Johnson & Graham (2004), red lines are tracings of observed bedding for this study. Person for scale is ca 1.8 m tall.

rover traverse, the F2 intervals appear to be thicker and more extensive than along the western traverse.

Two possible interpretations of the lateral relations between the strata exposed in the eastern and western areas of Hartmann's Valley are

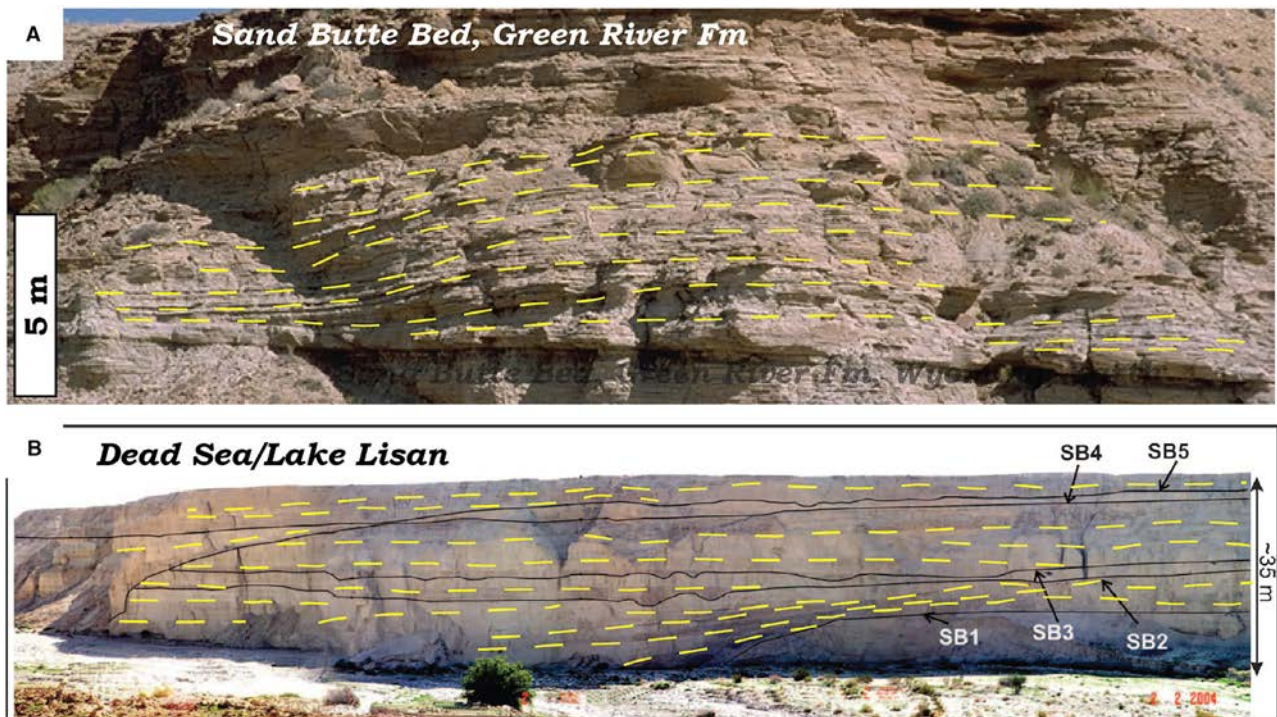


Fig. 25. (A) Undulating lake bed topography displayed in an outcrop of the Sand Butte Bed of the Green River Formation (Bohacs *et al.*, 2002). (B) Mudstone strata of Lake Lisan, Dead Sea. The outcrop shows a stack of five stratigraphic sequences that are separated by undulose (scoured) sequence boundaries, which record past lake floor topographies (Bartov *et al.*, 2012). In this case depositional lobes are interspersed with erosion surfaces, adding to the undulosity of these strata.

portrayed in Fig. 27. One alternative (Fig. 27A) is based on sequence stratigraphy and the other (Fig. 27B) reflects a purely facies-based interpretation. Both interpretations are plausible on the basis of currently available data.

The basal interval in the western traverse area (-4436 m to about -4429 m) is conceptualized to contain F1-F2 type parasequences as seen at PH, with interspersed multi-decimetre-scale bedsets of F5. This interval is interpreted as a highstand systems tract, and it is posited here that the coeval interval in the eastern area is not exposed. The apparently abrupt basal surface of the overlying sandstone interval at Baynes Mountain (Fig. 16) is interpreted as a depositional-sequence boundary. The overlying sandstone-dominated strata represent a lowstand systems tract that pinches out towards the east. The abrupt upper surface of this interval is overlain by a metre-scale interval of F1 and F2 and represents the Transgressive Surface. The overlying interval, dominated by multiple metres of F6 with intercalated decimetre-scale intervals of

both F5 and F1, is interpreted as a transgressive systems tract. The top of this interval ($ca -4421$ m in the west and -4427 m in the east) represents the maximum flooding surface based on the change in stratal stacking patterns that occurs across it, and its distinctive character along both the western and eastern traverses. The overlying interval, up to the top of both sections, is interpreted to contain parasequences that appear to stack in a progradational pattern.

Stratigraphic patterns such as these are quite characteristic of underfilled lake basins on Earth (Bohacs *et al.*, 2000): moderately developed highstand systems tracts, a poorly developed basal sequence boundary (with minimal erosion, probably being due mostly to lake water withdrawal and subaerial exposure) overlain by a relatively thin lowstand systems tract (because lake-level fall was due to decreased water discharge which implies decreased sediment discharge), a well-expressed maximum flooding surface, and a relatively thick transgressive systems tract (because lake-level rise is caused by

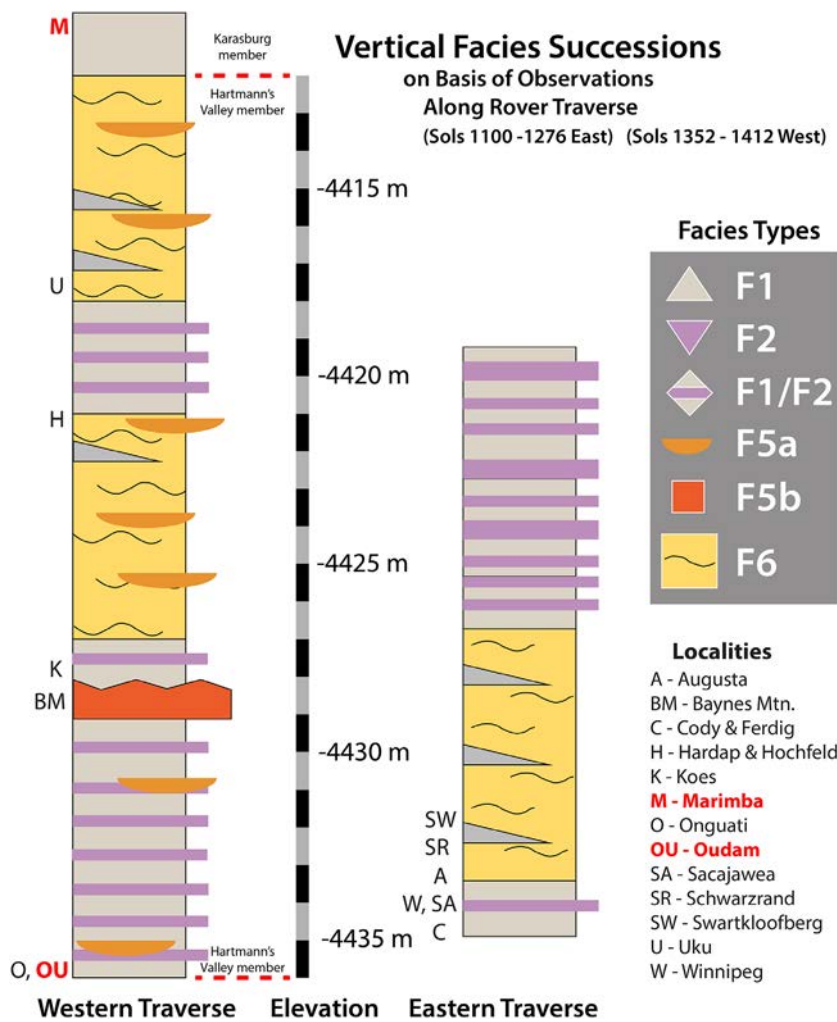


Fig. 26. A comparison of presumed vertical succession of facies for the eastern and western Hartmann's Valley traverse. 'Localities' refers to locations and target names mentioned in the text. 'Bold Red' localities indicate CheMin drill locations. Elevation scale and red dashed horizontal lines mark the presumed vertical extent of the Hartmann's Valley interval (MSL Sedimentology and Stratigraphy Working Group).

increased water discharge and concurrent increased sediment discharge). These stratigraphic patterns also resemble those interpreted in the underlying interval of the Murray formation at Pahrump Hills (Schieber *et al.*, 2022).

Figure 27B portrays a facies-based interpretation of the lateral distribution of rock types between eastern and western traverse areas based on analogous systems on Earth, particularly Lake Bogoria (Bohacs *et al.*, 2000; Hickley *et al.*, 2003; De Cort, 2016; Bohacs *et al.*, 2014). This perspective emphasizes lake-floor bathymetry and its effect on facies distribution via compensational stacking while honouring the lateral changes in rock types observed and assuming that regional depositional dip was relatively low-angle. The resulting patterns indicate that the earliest depositional axis was in the east, and shifted to the west in the middle of the section with a thick interval of F5 (Baynes Mountain) overlain by multiple metres of F6 and

persisting in the west throughout the upper part of the section with intercalated F1/F2 and F5. The aforementioned interpretation suggests that the lateral extent of individual intervals of F6 is rather limited (*ca* 500 m). This style of limited lateral extent of lacustrine facies accords with the scale of undulating bathymetric features in Lake Bogoria (Fig. 23), a not uncommon feature in lacustrine systems on Earth (Baganz *et al.*, 2013; Bohacs *et al.*, 2014).

STRATIGRAPHIC SUCCESSION AND ALLIED MINERAL & CHEMICAL DATA

The facies descriptions given above relate to processes that produce characteristic sedimentological features as a result of water flow, water quantity, extent of evaporation and grain size of the particles. In a prior study, introduction of other data sets/observations was essential

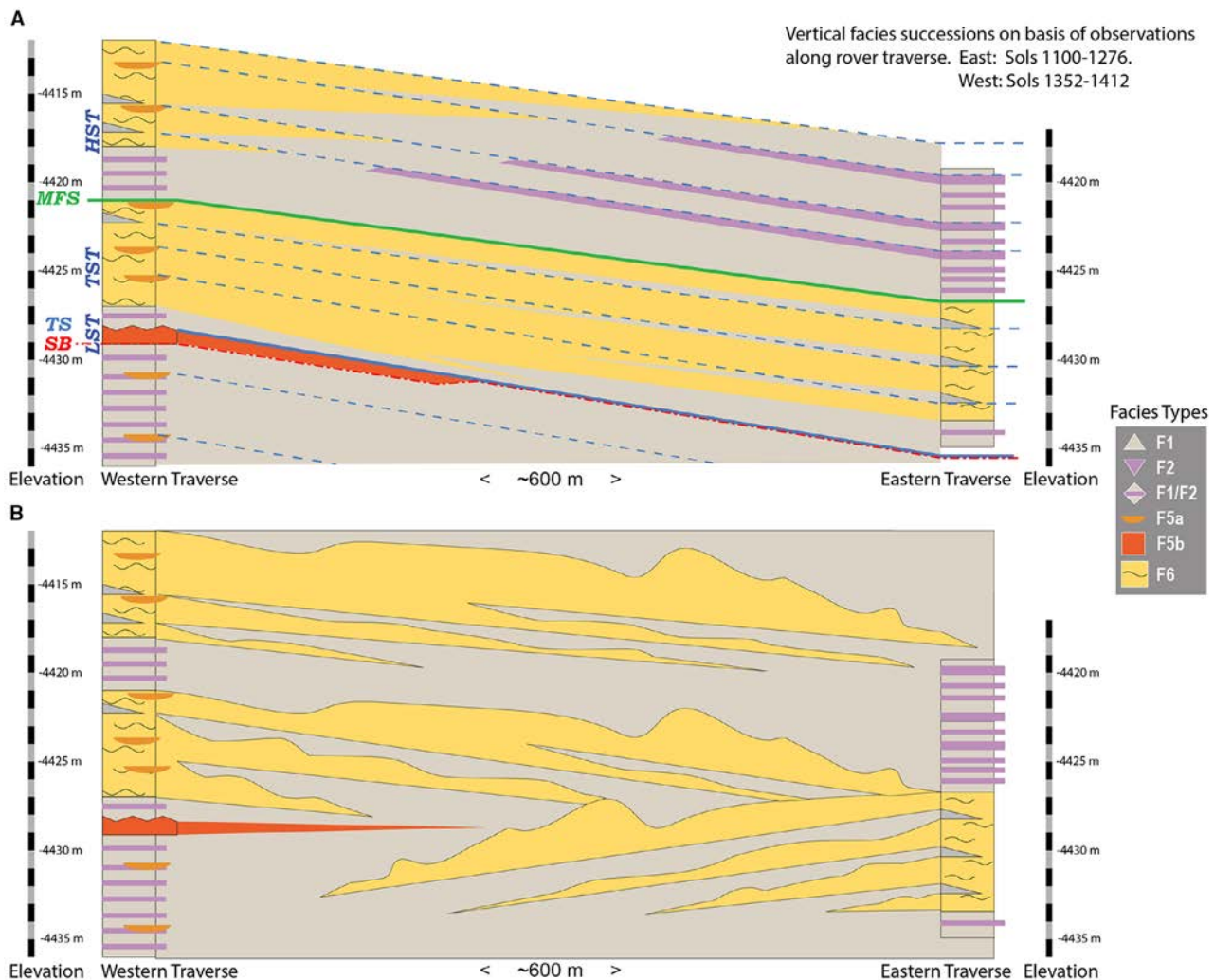


Fig. 27. Schematic rendering of possible west–east facies relations in the Hartmann's Valley interval. (A) West–east cross-section portrays a sequence-stratigraphic correlation of the two areas inspired by stratal stacking patterns in analogous systems on Earth (Gierlowski-Kordesch & Kelts, 1994, 2000; Bohacs *et al.*, 2000, 2014). It emphasizes stratal continuity and correlation without attempting to portray lake-floor bathymetry. The key horizon that connects the eastern and western areas is what appears to be a major flooding surface exposed at –4421 m in the west and –4427 m in the east. The relief on this surface is about 1 m per 100 m – quite within the range of lake-floor relief seen in similar systems on Earth (Fig. 23). All other flooding surfaces are interpreted to have similar slopes because their stratal character does not indicate any major reorganization of the coeval landscape. The other readily recognizable flooding surface is the top of the sandstone interval at Baynes Mountain (Figs 13 and 26). More subtly expressed flooding surfaces occur at the base of multi-decimetre-scale intervals of F1 intercalated with thicker intervals of F6, as well as at the tops of thicker intervals of F2 in the upper part of the eastern section. (B) A purely facies based interpretation of lateral relationships, where the surfaces of the F6 mudstone tongues show undulosity scaled in analogy to the Lake Bogoria lake-floor topography (Fig. 23). LST = lowstand systems tract; TST = transgressive systems tract; HST = highstand systems tract; MFS = maximum flooding surface; TS = transgressive surface; SB = sequence boundary.

in understanding the changes that produced the facies observed in the Pahrump Hills succession (Schieber *et al.*, 2022). There, integration of mineral (CheMin) and compositional (APXS, ChemCam) data was invaluable for a deeper understanding of the accumulating succession

(Schieber *et al.*, 2022). That approach, however, is not readily applicable to the HV interval because fewer data were collected over a much larger area (Fig. 1), rendering vertical context less constrained. Nonetheless, the following sections integrate the comparatively sparse

compositional and mineralogical data available from the HartV interval.

Observations – CheMin

Strictly speaking, there is only one CheMin analysis in the HVi, target Oudam, collected at the very base of the interval (-4435.7 m). The next higher CheMin analysis (target Marimba – MB) was collected directly above the Hartmann's Valley interval as defined by the MSL Sedimentology and Stratigraphy Working Group (Fedo *et al.*, 2018), but it is included in this analysis (stratigraphic position of CheMin samples marked in Fig. 26). Because the HVi shares essential sedimentological elements with the underlying Pahrump Hills interval, these data were compared with the CheMin analyses from Pahrump Hills [Confidence Hills (CH), Mojave (MJ), Telegraph Peak (TP); Schieber *et al.*, 2022] and Buckskin (BK; Morris *et al.*, 2016). All of these data are summarized in Table 2.

Comparing Oudam (OU) with the PH samples (Table 2), one obvious difference is the significantly lower amount of pyroxene in Oudam. The ratios of plagioclase to olivine are *ca* 14 at PH (samples CH, MJ, TP) and *ca* 20 at Oudam and Marimba. Likewise, the ratio of plagioclase to pyroxene is *ca* 2.5 at PH, and comparatively elevated at Oudam (6.4) and Marimba (10.6). The Buckskin sample (upper PHi) is in a category all its own by containing no olivine or pyroxene, even though the plagioclase abundance is in keeping with other PHi samples. Buckskin contains an unusual abundance of tridymite (17.1%, Morris *et al.*, 2016), but tridymite was also detected at TP (6 m below, 1%) and at OU (11 m above, 0.8%), although at lower abundances. The parallel occurrence of cristobalite in the three tridymite-bearing samples (TP, BK, OU) suggests a source that contained both of these high-temperature silica polymorphs. Matrix Ca-sulphate is much more abundant at OU and MB (*ca* 5% or more) than in the PHi samples (*ca* 1% or less). Similarly, opal-CT and Al-bearing diagenetic phases (kerolite, allophane) are significantly more abundant at OU and MB when compared with the PHi (Table 2).

Observations – Alpha particle X-ray spectrometer (APXS)

The APXS analyses were published in Thompson *et al.* (2020) and Schieber *et al.* (2022). For this paper, the most salient PH and HV APXS data are summarized in Fig. 28, and the

complete data set can be seen in Appendix S3 (Figs S3-1 and S3-2). Overall, APXS analyses show lower SiO_2 , Al_2O_3 , TiO_2 , Cr_2O_3 , MnO , Na_2O , P_2O_5 and Zn , and higher FeO , MgO , K_2O , Ni , CaO , SO_3 and Cl concentrations than at PH (Thompson *et al.*, 2020). Notable shifts in composition for several elements at the Chinle unconformity (Schieber *et al.*, 2022) and the presumed Baynes Mountain sequence boundary are intriguing. There are no obvious differences between the two transects east and west of the Naukluft plateau (Fig. 1).

Observations – ChemCam

ChemCam analyses from the PHi show notable shifts at the Chinle depositional-sequence boundary, one of the stratigraphic breaks discussed above (Fig. 29).

The ChemCam bedrock analyses (Fig. 29) indicate that the content of Ca-bearing and Al-bearing phases is generally lower in HV samples relative to PH. These lower abundances have been attributed to open-system weathering of the sedimentary materials that accumulated during HV deposition, either prior to or during their emplacement, with some degree of plagioclase and feldspar dissolution (Mangold *et al.*, 2019). A fraction of the leached Al ions may have contributed to formation of colloidal Al-bearing phases such as allophane (Table 2), and a portion of the Ca ions possibly crystallized in the form of Ca-sulphates due to later evaporation (Rapin *et al.*, 2019).

When averages are computed for PH below and above Chinle (Fig. 29), the ChemCam bedrock data show a clear increase in CaO and a clear decrease in Al_2O_3 across that boundary. The Al_2O_3 data match the shift already observed for the APXS data (Fig. 28), whereas the CaO shift is not apparent in APXS data. This contrast illustrates the systemic difference between the APXS and ChemCam data sets. Unlike APXS that integrates over an area *ca* 1.5 to 2.5 cm in diameter, ChemCam highlights small-scale differences in elemental distribution, and in HV this is attributed to scattered Ca-sulphate grains in the rock matrix (Figs 30 and 31). No significant compositional changes are seen by ChemCam at the elevation of the Baynes Mountain sandstone interval.

The submillimetre spatial resolution of ChemCam analyses shows that, although the Hartmann's Valley bedrock has an overall CaO content that is similar to the Pahrump Hills bedrock below Chinle,

Table 2. CheMin analyses of Oudam and Marimba in the context of Pahrump Hills interval (Phi) data.

	Pahrump Hills				Hartmann's Valley	
	Mineralogy, normalized Confidence Hills (CH)	Mineralogy, normalized Mojave (MJ)	Mineralogy, normalized Telegraph Peak (TP)	Mineralogy, normalized Buckskin (BK)	Mineralogy, normalized Oudam (OU)	Mineralogy, normalized Marimba (MB)
Elevation (m)	-4460.5	-4459.6	-4453.0	-4447.0	-4435.7	-4410.7
Σ Plagioclase	24.0	25.0	23.0	21.4	27.7 (3.2)	14.8 (6.4)
Andesine	20.0 (2)	22.0 (1)	20.0 (2)		20.8 (1.3)	9.5 (3.2)
Oligoclase	4.0 (2)	2.8 (4)			7.0 (2)	5.3 (3.2)
Albite			3.0 (1)			
Anorthoclase			7.0 (3)			
Sanidine	4.0 (4)		0.0	4.2		5.3 (3.2)
Forsteritic olivine	1.5 (4)	1.6 (4)	2.1 (7)		1.3 (0.6)	0.8 (0.6)
Σ Pyroxene	14.8	6.1	7.6	0.0	4.3 (1.5)	1.4 (1.0)
Augite	7.0 (6)	2.7 (5)	0.0			
Hedenbergite			1.6 (6)			
Pigeonite	5.4 (7)	3.4 (6)	6.0 (1)		2.0 (0.6)	
Orthopyroxene	1.8 (7)				2.3 (0.9)	1.4 (1.0)
Magnetite				3.5		
Maghemite	3.7 (3)	4.2 (3)	9.0 (1)		0.6 (0.2)	
Hematite	7.3 (5)	3.5 (2)	1.3 (4)		15.9 (0.8)	5.6 (1.4)
Quartz	0.4 (1)	0.5 (1)	0.5 (3)		0.6 (0.2)	0.3 (0.1)
Cristobalite			8.0 (1)	3.0	1.2 (0.2)	
Tridymite			1.0 (1)	17.1	0.8 (0.3)	
Opal-CT	1.8 (6)	2.1 (9)	1.4 (7)		20.0 (10)	10.0 (5)
Kerolite	2.4 (5)	0.8 (4)	2.7 (4)		5.9 (0.9)	
Fe-allophane						10.0 (5)
Phyllo/Clays	1.5 (6)	2.6 (9)			2.0 (1)	25.0 (10)
Amorphous	36.0	48.0	31.0	50.0	15 (5)	20.0 (10)
Apatite		1.2 (2)	0.5 (0.5)			
Σ Ca-sulphate	0.4	0.0	1.2		4.7	5.6 (1.4)
Anhydrite	0.4 (1)		0.8 (2)	0.9	2.6 (0.2)	2.8 (0.6)
Bassanite			0.1 (1)			0.9 (0.3)
Gypsum			0.3 (2)		2.1 (0.2)	1.9 (0.5)
Ilmenite	1.2 (3)					0.7
Parabutlerite		0.6 (1)	0.3 (2)			
Rozenite	0.2 (2)					

Table 2. (continued)

	Pahrump Hills				Hartmann's Valley	
	Mineralogy, normalized Confidence Hills (CH)	Mineralogy, normalized Mojave (MJ)	Mineralogy, normalized Telegraph Peak (TP)	Mineralogy, normalized Buckskin (BK)	Mineralogy, normalized Oudam (OU)	Mineralogy, normalized Marimba (MB)
Jarosite	0.9 (2)	2.6 (3)	1.2 (4)			0.9 (0.5)
Pyrite	0.5 (2)	1.4 (3)	0.5 (3)			
Shortite	0.5 (2)		1.1 (6)			
Thenardite			0.7 (5)			
Kieserite	0.4 (2)	0.2 (2)	0.2 (3)			
SO ₃ (wt. %)	4.9	6.3	2.5		5.6	7.7

Data for CH, MJ and TP are from Schieber *et al.* (2022); data for BK are from Morris *et al.* (2016). Data for Oudam and Marimba have been newly analysed for this study. Values in parentheses represent the estimated standard deviation (1 sigma) in the last quoted number. Green shaded columns indicate data from published sources. Beige shading indicates totals for mineral groups, such as plagioclase, pyroxene, and Ca-sulfates. The bold values are used for data that have been analyzed for this paper and were not previously published. Gray shading indicates minerals that are discussed together in the text.

HV shows sporadic Ca-sulphate detections that were not observed at Pahrump (Fig. 29). This Ca-sulphate enrichment is highlighted by the CaO and SO₃ association illustrated in Fig. 30, which can be modelled to infer disseminated Ca-sulphate grains of about 200 µm size in the mudstone matrix throughout the entire vertical extent of the HV interval (Appendix S4). Scattered submillimetre-sized light-toned grains are commonly observed in ChemCam RMI (Remote Microscopic Imager) target images from HV bedrock (Fig. 31) and may represent evaporitic Ca-sulfates (Rapin *et al.*, 2019). ChemCam data analysis has also indicated the presence of sporadic, minor amounts of halite disseminated in HV bedrock (Thomas *et al.* 2019).

Compositional trends

The observation that both APXS and ChemCam data show compositional shifts within the PHi (Chinle) and HVi (Baynes Mountain) suggests that the common practice of comparing chemical averages at the ‘formation’ or ‘member’ level is not useful in deciphering the depositional history of Mount Sharp strata.

Some exceptions to the ‘general’ HV bedrock compositions have been observed in F1/F2 facies near –4423 m elevation with increased Al, Ca and Na but low hydration (Fig. 29). These data could point to a slightly different sediment provenance within a specific F1/F2 bedrock

interval at this location. The data are consistent with less altered source materials and more plagioclases and feldspars.

GEOLOGICAL HISTORY

The strata of the Hartmann’s Valley interval closely resemble those described from the Pahrump Hills interval and appear to record a continuation of the underfilled evaporative lake system proposed for the Pahrump Hills strata (Fig. 2; Schieber *et al.*, 2022). Particular similarities include provenance lithotypes and changes, as well as erosion and transportation. Subtle differences include type and intensity of source rock weathering, depositional sub-environments and early diagenesis.

Provenance lithotypes and weathering

At Pahrump Hills (samples CH, MJ and TP), careful consideration of chemical and mineralogical data, in combination with geochemical modelling (Schieber *et al.*, 2022), led to the conclusion that the sedimentary materials supplied to the basin were dominated by detrital minerals derived from basaltic bedrock and glass that were pulverized by meteor impacts (Arp *et al.*, 2019).

Because Mars has long been considered as a planet dominated by aeolian processes (e.g.

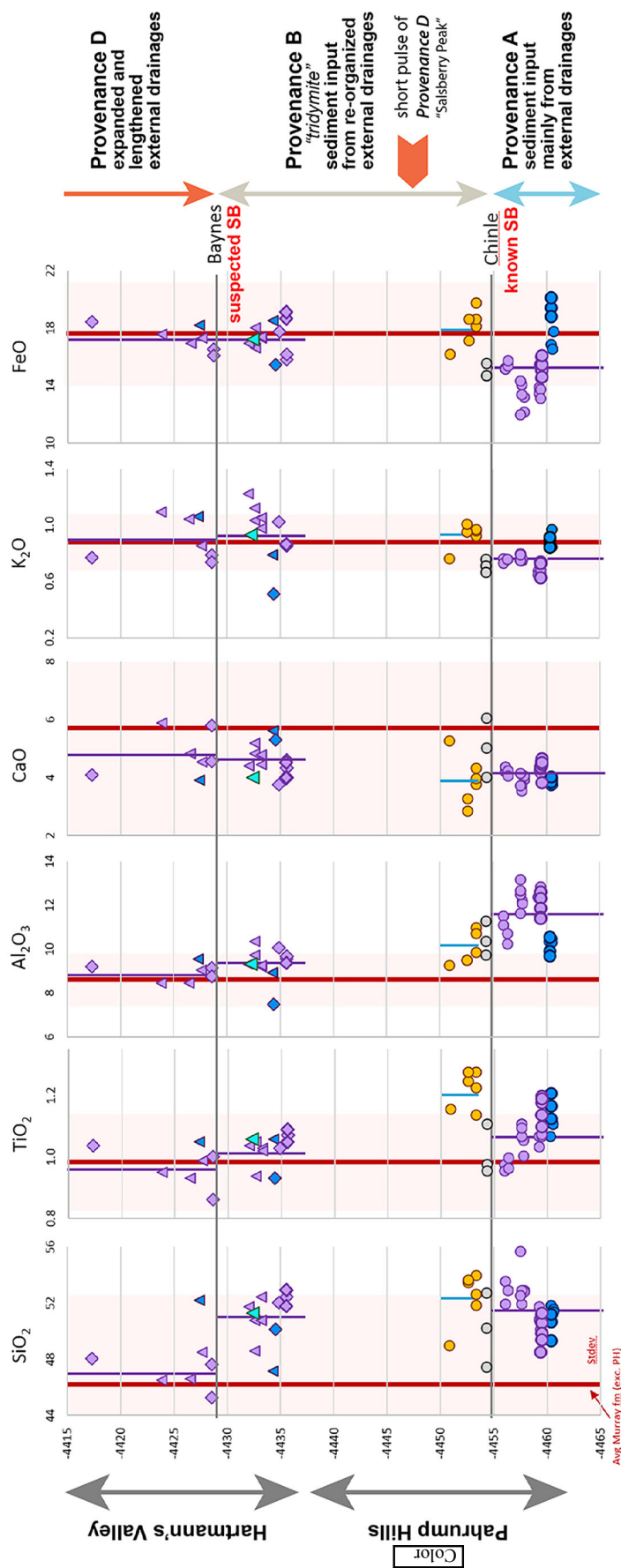


Fig. 28. SiO_2 , TiO_2 , Al_2O_3 , CaO , K_2O and FeO as measured by APXS (Alpha Particle X-ray Spectrometer) on bedrock as a function of elevation for Pahrump Hills and Hartmann Valley mudstone targets. Also marked are the known Chine sequence boundary (SB) and the Baynes Mountain (candidate) SB. Provenance types A, B, and D were discussed by Schieber *et al.* (2022) and are adopted for this study. Explanation of symbols: circles – Pahrump Hills; diamonds – Hartmann's Valley east of Naukluft Plateau; triangles – Naukluft Plateau; triangles – Hartmann's Valley west of Naukluft Plateau.

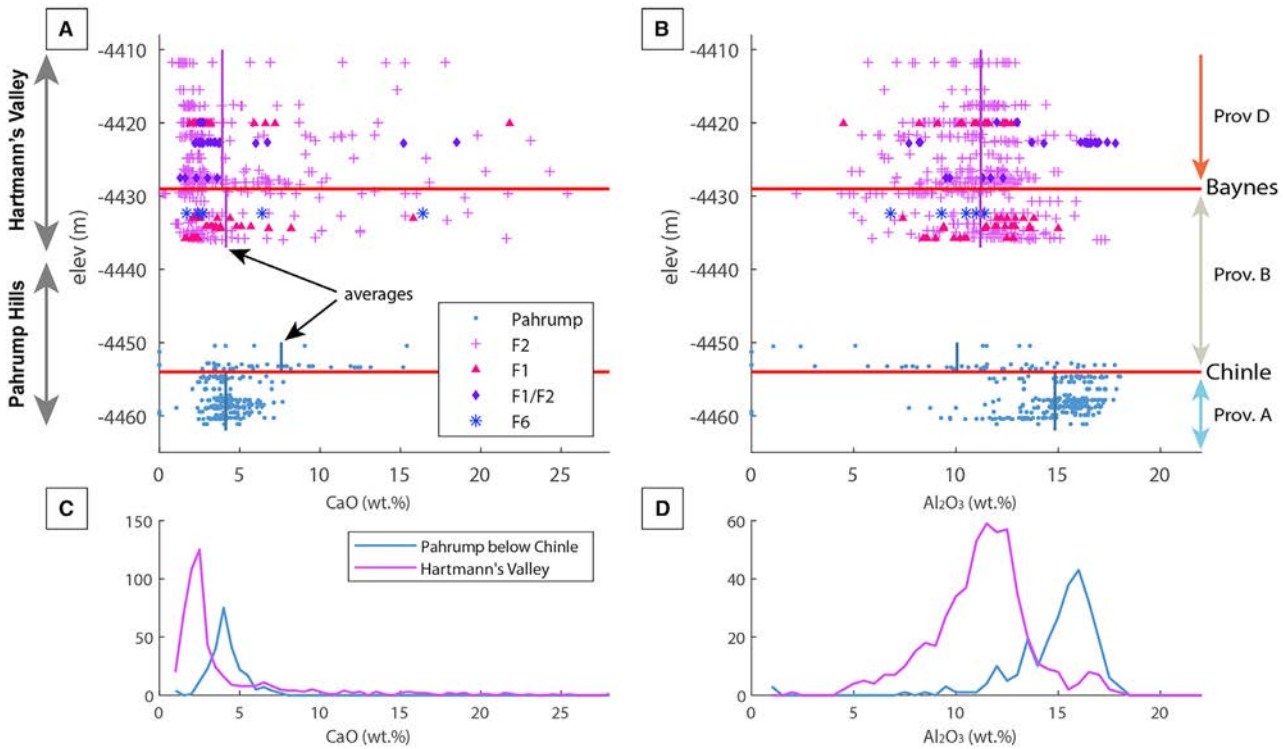


Fig 29. (A) and (B) CaO and Al₂O₃ content as measured by ChemCam on bedrock as a function of elevation for Pahrump Hills and Hartmann Valley targets. Vertical bars (black arrows) indicate average abundances of corresponding stratigraphic intervals. (C) and (D) Distribution of CaO and Al₂O₃ abundances in Pahrump below Chinle and in the Hartmann's Valley interval. Note that in (C), HV data are intermittently skewed towards higher CaO values due to laser shots that intercepted matrix sulphate grains. This provides a nearly Ca-sulphate free bedrock modal CaO abundance, showing it to be lower than at Pahrump (below Chinle) even though the CaO averages of the strata are quite similar. (D) Shows clearly lower Al₂O₃ abundances for HV relative to Pahrump, and also that this drop in Al₂O₃ abundances actually occurred at the Chinle unconformity, just as seen in the APXS (Alpha Particle X-ray Spectrometer) data (Fig. 28).

Fenton *et al.*, 2003), aeolian supply to crater basins of fine particles from far away is always a considered possibility for many Mars researchers. Yet, for an early Mars with an active hydrosphere it is worth looking at present-day Earth for guidance. There, the volume of fine-grained sediments that enter the oceans via rivers is several orders of magnitude larger than any conceivable aeolian input (e.g. Prospero, 1981). As a specific example, the floodplain of the Copper River delta is known for spectacular aeolian dust plumes that can be carried far offshore into the Gulf of Alaska (Crusius *et al.*, 2011), yet the river itself pumps out more suspended sediment in a single day (Brabets, 1992) than the estimated aeolian flux from its floodplain for an entire year. Thus, it is reasonable to assume that streams supplied the

bulk of fine-grained sediments that form the Murray formation of Aeolis Mons.

Examining the origin of mineral components in the Pahrump Hills succession, Schieber *et al.* (2022) concluded that diagenetic products such as opal-CT, kerolite, Fe-allophane and phyllosilicates/smectite reflected open-system weathering (in catchment or at site of deposition). An increase of these components in the HV interval, as well as the increase in hematite (OU and MB) suggests increased open-system weathering for Hartmann's Valley compared to samples lower in the section. This CheMin-based assessment is supported by Ca-sulphate-corrected APXS data that suggest CIA (chemical index of alteration, Nesbitt & Young, 1982) values between 42 and 62 and low to moderate weathering (Gwizd *et al.*, 2022), as well as by evaluation of ChemCam

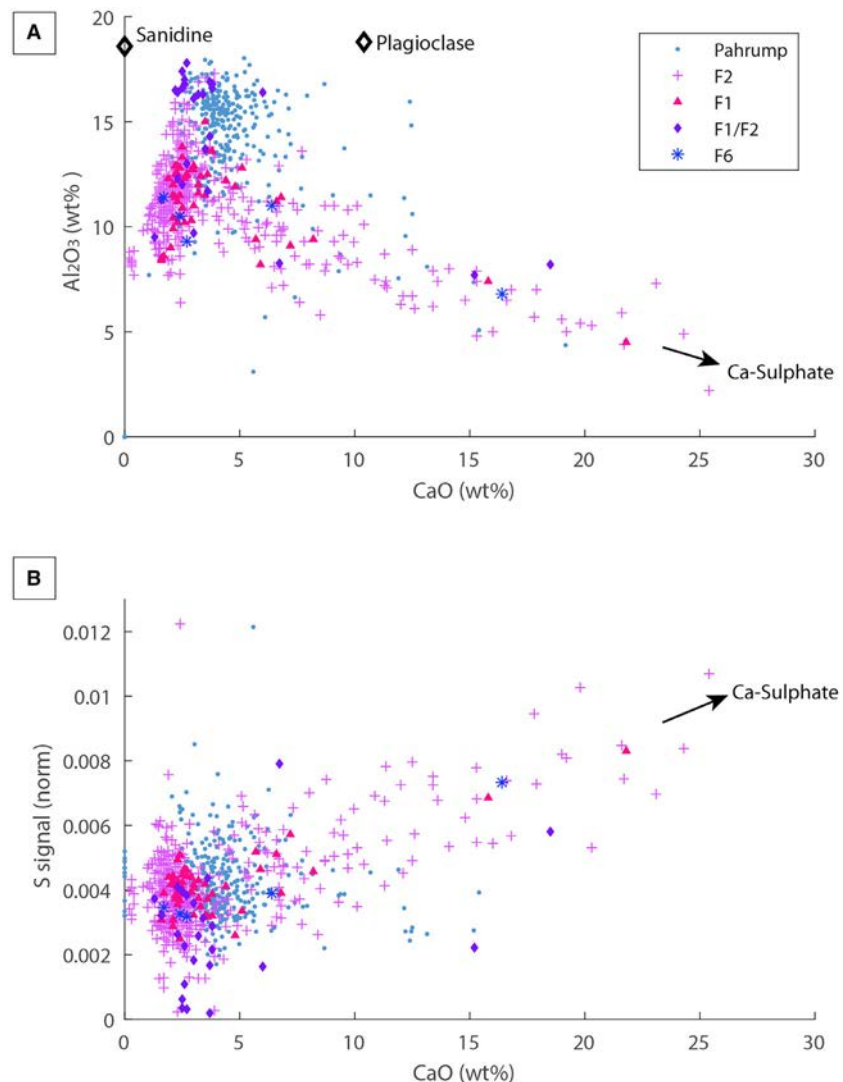


Fig. 30. ChemCam bedrock data that show CaO content as a function of Al₂O₃ (A) and sulphur (B) content (S signal). Whereas most data cluster in the low CaO portion of these diagrams, there is systematic scattering towards higher CaO values, due to laser shots interacting with Ca-sulphate grains in the rock matrix (Fig. 31).

compositional data (Mangold *et al.*, 2019). That this change from minimal to moderate weathering is detected across an unconformity (Chinle), implies that a significant amount of time had to pass (to allow for weathering) between the formation of the Chinle erosion surface and the subsequent deposition of notably more weathered clastic detritus, providing further support for our perspective on subdividing the studied succession.

The composition of the Buckskin sample (Morris *et al.*, 2016) (Table 2) signals a significant change in provenance during deposition of the Pahrump Hills interval. The complete lack of Fe–Mg mafic silicates, in addition to the abundance of tridymite and cristobalite, suggests a significant provenance re-arrangement. That this shift may

already have been underway when the strata of the upper part of the Pahrump Hills outcrop were deposited and continued farther up-section from Buckskin is suggested by the parallel detection of tridymite and cristobalite in the TP sample (6 m below BK) and the OU sample (at the base of the HVi, 12 m above BK). Detection of this tridymite–cristobalite duopoly across 18 m of strata suggests a widespread source rock type of unique composition in the catchment that supplied sediment to the northern portion of Gale crater (Palucis *et al.*, 2014). Although tridymite and cristobalite at BK have previously been ascribed to silicic volcanics (Horwell *et al.*, 2013; Morris *et al.*, 2016), *in situ* hydrothermal alteration (Yen *et al.*, 2021) and meteorite impacts (Schieber *et al.*, 2022), the here observed stratigraphic range of tridymite and

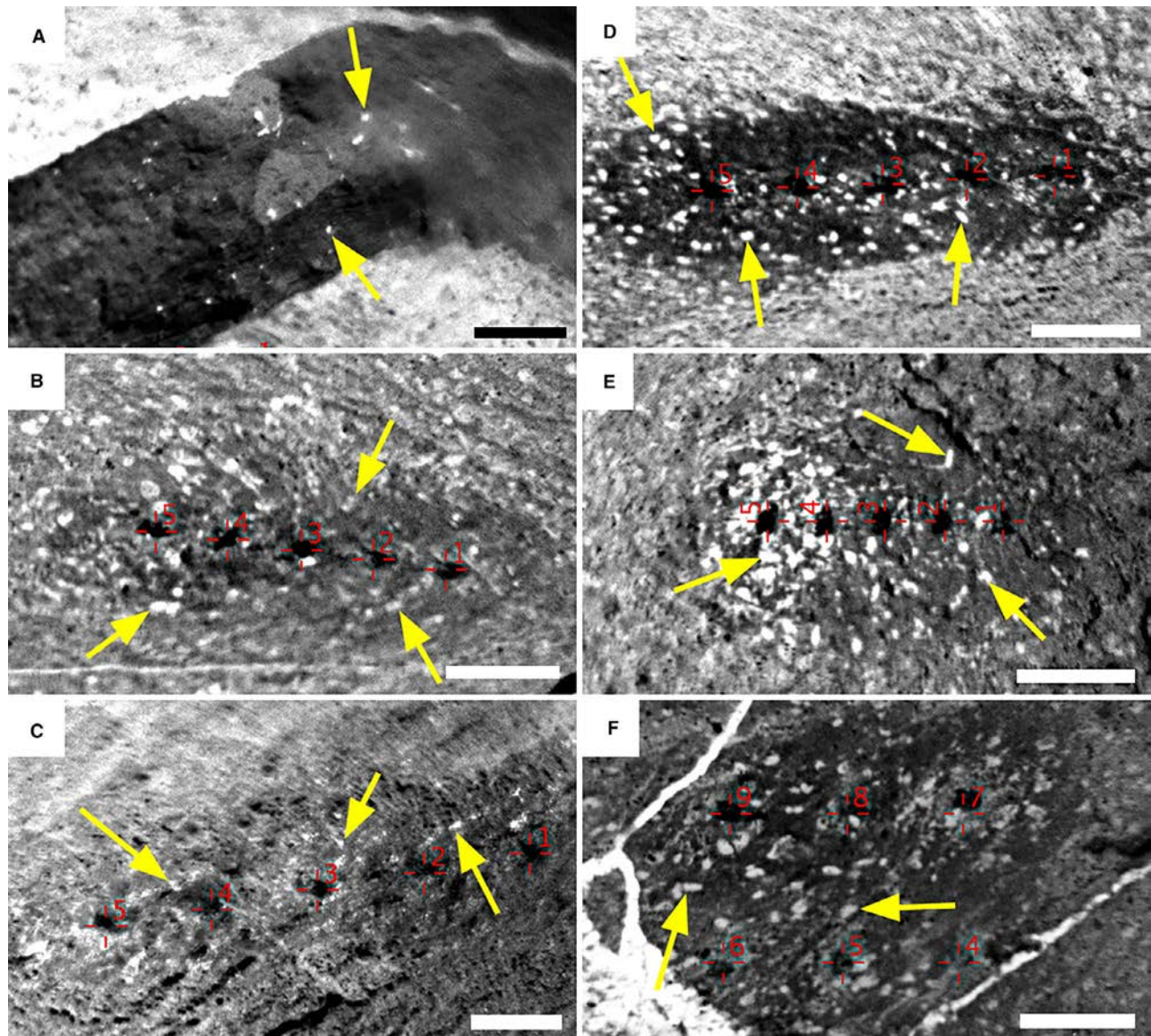


Fig. 31. ChemCam RMI (Remote Microscopic Imager) images associated with analysis of bedrock targets. Yellow arrows mark crystal shapes and red crosses mark ChemCam laser shots. Scale bars are 5 mm long. Images (A) to (C) are from the eastern Hartmann's Valley traverse, and images (D) to (F) are from the western HV traverse. (A) Sol 1214, target Hunkab. Rover rolled over this rock and cracked it. Small light toned crystal shapes can be seen on the broken surface. (B) Sol 1264, target Awahab. ChemCam laser shots cleaned dust from the surface and exposed small light toned crystal shapes. (C) Sol 1166, target Swakop. This is a different facies (F6) from the other images (F1 and F2) and the crystal shapes are comparatively tiny. (D) Sol 1412, target Huambo, showing abundant light toned crystal shapes. (E) Sol 1380, target Onawana, showing abundant light toned crystal shapes. (F) Sol 1363, target Onganja, showing abundant light toned crystal shapes. ChemCam RMI images are greyscale images, and as such do not convey colour information. However, in places where RMI and MAHLI images coincide (e.g. Rapin *et al.*, 2019), light toned crystal shapes are invariably whitish in appearance, and this colour assumption is extended to the light toned crystal shapes seen in (A) to (F).

cristobalite input and the fact that the Martian upper crust represents a heavily 'cratered volume' (Hartmann & Neukum, 2001; Edgett & Malin, 2002)

with a sizeable volume of impact modified rocks, makes it almost certain that both minerals came from impact-related debris and melt sheets

(Jackson *et al.*, 2011; Trepmann *et al.*, 2020; Cavigie *et al.*, 2022; Zamiatina *et al.*, 2023) rather than any other source.

This latter viewpoint is consistent with observations on crystallite size and strain parameters for tridymite and cristobalite, that indicate very small crystallites (*ca* 50 nm) and highly strained material (Schieber *et al.*, 2022). The complete lack of olivine and plagioclase at BK and significantly higher plagioclase-to-olivine and plagioclase-to-pyroxene ratios at OU and MB suggest increasing sediment contribution from sources that experienced significant open-system weathering in hydrated surface or near-surface environments (e.g. Mangold *et al.*, 2019).

The provenance implications suggested by the CheMin data are corroborated by the associated APXS and ChemCam data. For example, Fig. 28 shows the APXS abundances distribution of SiO₂, TiO₂, Al₂O₃, K₂O and FeO plotted as a function of elevation. For the known sequence boundary/unconformity at Chinle (Schieber *et al.*, 2022), Fig. 28 shows abrupt compositional shifts for several elements, most notably for TiO₂, Al₂O₃ and FeO, a minor increase for K₂O, and not much change for SiO₂. As detailed above, examination of the HV sedimentary succession suggests that the Baynes Mountain sandstone interval (Figs 16, 26 and 27) potentially marks another stratigraphic break, and this inference is supported (Fig. 28) by a clear shift for SiO₂ as well as minor changes for TiO₂ and Al₂O₃. Provenances A and B (as summarized in Fig. 28) were already deduced from the more extensive data set at Pahrump Hills (Schieber *et al.*, 2022) and CheMin data, on the basis of the tridymite ‘tracer’, strongly suggest that influx from provenance B extends above Pahrump Hills and into the Hartmann’s Valley interval.

Provenance D (as summarized in Fig. 28) is tentatively carried over from the earlier Pahrump Hills study (Schieber *et al.*, 2022), where a drop in SiO₂ and TiO₂ suggested a provenance change for the Salsberry Peak interval. That a provenance shift occurred is suggested by the APXS data (Fig. 28) and disappearance of tridymite in Marimba (Table 2), but whether it is, indeed, a return of provenance D is only speculative because of sparse data coverage.

The changes in sediment composition that are observed over comparatively short timescales in stratigraphic sections at HV and PH (Fig. 28) are most probably due to changes in sediment routing across the catchment area that tap different

provenance lithofacies of varying compositions, as well as weathering, alteration and mineral segregation during transport (e.g. Heins & Kairo, 2007; Mangold *et al.*, 2011; Siebach *et al.*, 2017; Bedford, 2019).

Variations in bedrock character are possible over short spatial and temporal scales because infilled impact craters and intercrater areas allow for lateral variation in composition over short distances (Edgett & Malin, 2002). This is a common situation for Earth as well, where for example lava composition in volcanic complexes can vary substantially over short time and spatial scales (i.e. years to centuries; Pietruszka & Garcia, 1999; Vlastelic *et al.*, 2007). Martian bedrock has also been interpreted as varying over comparable spatial scales (McSween *et al.*, 2006; Schmidt *et al.*, 2009; Ehmann & Edwards, 2014). For the Murray formation, at least five different provenance lithotypes have been inferred: (i) subalkaline basalt; (ii) trachybasalt; (iii) potassium-rich volcanic source; (iv) highly evolved, silica-rich igneous rock; and (v) fractionated, relatively SiO₂-rich subalkaline basalt (Bedford, 2019).

Because significant tectonic uplift was not a factor on Mars, changes in sediment routing were probably due to landscape evolution, volcanic activity or meteorite impact. Landscape evolution affects sediment sources, routing and volumes through autogenic stream piracy, and drainage blockage and diversion (e.g. Schumm, 1981). On Earth, volcanism can change sediment-supply character and rates rapidly and significantly by increasing the volume of readily erodible sediment or by stream blocking and drainage diversion (Rhodes *et al.*, 2002; Manville *et al.*, 2009; Rhodes & Carroll, 2015). Meteorite impact can produce landscape modifications analogous to those effected by volcanic eruptions. On Mars, although the effects of volcanism and water-driven landscape evolution varied through time and space, meteorite-impact activity was ubiquitous early in the planet’s history (Edgett & Malin, 2002; Osinski, 2006).

Abrupt changes in lacustrine sediment composition related to changes in provenance in volcanic source terranes, analogous to compositional changes observed in the Murray formation, have been reported from numerous lacustrine systems on Earth (Yuretich, 1979; Palmer & Shawkey, 1997; Aydar, 1998; Stockhecke *et al.*, 2014; Mtelela *et al.*, 2016; Kataoka & Nagahashi, 2019; Ocampo-Díaz *et al.*, 2021).

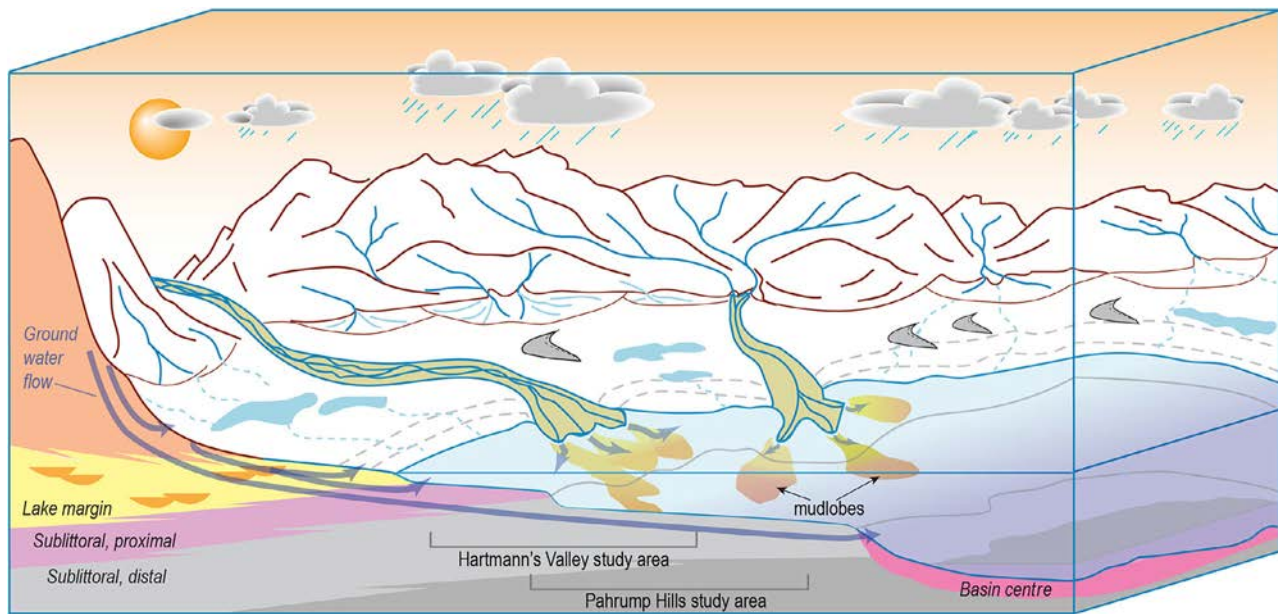


Fig. 32. Depositional setting of the Hartmann's Valley succession in the context of a larger lake system. In this model, water supply to the lake is due to a combination of river and groundwater flow that discharged both sub-aerially and subaqueously (blue arrows). The mudlobes are prodeltaic sediments that accumulated as undulose-bedded macroforms (facies F6). Bedded evaporites are restricted to central portions of the lake. The figure depicts system components, not a specific point in time of lake basin evolution.

Erosion, transport and deposition

Longer-term wet periods accumulated F1, whereas F2 intervals developed during shorter-term dry periods with increased lake-water salinity. Longer-term, larger-scale dry periods lowered lake level and exposed the lake-floor sediments to desiccation and possible aeolian reworking with the remnant lake waters becoming hypersaline (Rapin *et al.*, 2019; Schieber *et al.*, 2022). At the end of such longer-term dry periods, the initial episodes of meteoric precipitation mobilized mechanically weathered sediments, and rejuvenated rivers carried these clastics and accumulated channel-fill and overbank sediments (F5) on land. At and near the lake shoreline, coarser-grained sediments accumulated. Finer-grained sediments accumulated as undulose-bedded macroforms (F6) in the pro-delta regions (Fig. 32). Later on, when the coarse detritus had been flushed through the system, only smaller volumes of finer-grained sediments were carried into the lake, resulting in accumulation of F1 and F2.

The facies observed in the HVi are characteristic of underfilled lake systems, with lake waters of elevated but variable salinity, frequent changes

in lake level and sediment accumulation rates, and accumulation of evaporite minerals. The dominant F1 and F2 mudstone facies record deposition in distal sublittoral to profundal settings, with relatively distal and low-benthic-energy conditions, frequent pauses in sediment accumulation and increases of bottom-water salinity, similar to those interpreted for Pahrump Hills (Bohacs *et al.*, 2000; Schieber *et al.*, 2022). The F1 to F2 intervals appear to stack in aggradational to weakly progradational patterns. Interbedded F6 intervals appear to record accumulation in moderately distal prodelta settings. Streams entering the hypersaline lake waters generated hypopycnal flows which developed buoyant jets with associated plumes capable of transporting fine-grained sediment in turbulent suspension. Coarse bedload grains were retained in distributary channels and very close to river mouth, forming stream-mouth bars and linear sand bodies (Renaut & Gierlowski-Kordesch, 2010). Such deposits are reported from the present-day Sandai and Emsos river deltas in Lake Bogoria (Kenya; Hickley *et al.*, 2003), the Jordan River Delta in the Dead Sea (Inbar, 1987; Hall, 1996), the Amu Darya Delta in the Aral Sea

(Uzbekistan; Conrad *et al.*, 2013), the Denton Creek delta (Texas; Tomanka, 2013; Howe, 2017), the Cretaceous Rayosa Formation, of the Neuquén Basin (Argentina; Zavala *et al.*, 2006) and the Upper Jurassic Har Hotol Synrift Sequence (Mongolia; Johnson & Graham, 2004). Shoreline progradation and nearshore bathymetric relief is enhanced in such situations and offshore bathymetric relief subdued. At Pahrump Hills, F6 would have mostly likely occurred in the interval just below Salsberry Peak (−4411 to −4408 m) but was undetectable because of limited access, extensive talus cover and disruptions by late-stage veins. Offshore, in the prodelta region, depositional processes are dominated by suspension fallout with some minor bedload transport. Sediment accumulates in macroforms with highly aggradational patterns of decimetre to metre-scale thick strata with continuous wavy subparallel to nonparallel bedding geometry (similar to F6). These strata commonly comprise dominantly interbedded coarse and fine mudstone (silt and clay size) in tabular to wavy laterally continuous beds (tens of metres); sedimentary structures include horizontal to inclined planar beds, graded beds, climbing current ripples and suspensational rhythmites, along with sparse and low-relief scour surfaces (Nemec, 1995; Johnson & Graham, 2004).

Facies F5 records channelized flow, probably on the subaerially exposed lake plain, similar to the setting of F5a at Pahrump Hills (Schieber *et al.*, 2022). In addition, apparent overbank-flow deposits are exposed in the HVi at Baynes Mountain (Fig. 16), suggesting a palaeogeographical position slightly farther downstream than at PH.

Diagenesis

At Pahrump Hills, diagenetic phases in CheMin samples (opal-CT, phyllosilicates, sulphates) provide essential insights into environmental conditions during accumulation and early burial, and their presence points to the operation of evaporation processes (Schieber *et al.*, 2022). Likewise, diagenetic phases deduced for the HVi (Table 2) span a wide range of solubilities, from calcium sulphates and silica (opal-CT) through kerolite (Mg-silicate) to iron sulphates, and suggest variable activities of Al, Fe and Si as well as neutral to low-pH waters. The diagenetic products such as opal-CT, Mg-smectites, Mg-sulphates, Fe-sulphate and colloidal alumino-silicates such as allophane plausibly reflect input of dissolved species from open-

system weathering (in the catchment or at the site of deposition). Variable point-to-point compositions of mudstones analysed by ChemCam are consistent with this scenario of dissolved-component origin and remineralization.

Elevated Al_2O_3 concentrations in erosion-resistant horizons of smooth weathering mudstone at PH (facies F2) suggested that Al-rich amorphous material (in the form of poorly ordered colloidal hydrous aluminosilicates, for example, allophane or imogolite) contributed to the relative erosion resistance of smooth weathering mudstone ledges (Schieber *et al.*, 2022). As Fig. 28 shows, notably lower Al_2O_3 concentrations make this an unlikely explanation for the resistant F2 mudstones in the HVi. However, HVi F2 mudstones show an approximate ten-fold increase in opal-CT content (Table 2), a plausible alternative cement.

Some minerals may have both detrital and diagenetic origins, depending on their stratigraphic context (phyllosilicates, hematite). The poorly ordered or amorphous component seen in CheMin analyses likely contains both detrital (volcanic and impact glass) and diagenetic constituents (allophane, imogolite, etc.).

Stratigraphic evolution and sequence stratigraphy

The stratigraphic succession and sequence stratigraphy of the HVi is interpreted to contain a complete depositional sequence overlying a highstand systems tract at base (Fig. 33). This depositional sequence is composed of lacustrine parasequences interbedded with fluvial channel fill strata. Parasequences with successions of F1–F2–F6 occur in areas directly connected to deltaic input points whereas parasequences with only F1–F2 represent areas between deltaic influx. As detailed in the *Stratigraphic succession and allied mineral & chemical data* section, the interval below Baynes Mountain is interpreted as a highstand systems tract, the F5 Baynes Mountain interval is a lowstand systems tract, and the overlying interval is a transgressive systems tract overlain by a highstand systems tract.

At the larger scale, although the strata of Pahrump Hills and Hartmann's Valley closely resemble one another and appear to record a persistent underfilled lake system, there appear to be two significant breaks in this interval. These breaks, at the base of Chinle and Baynes Mountain, are marked by changes in facies,

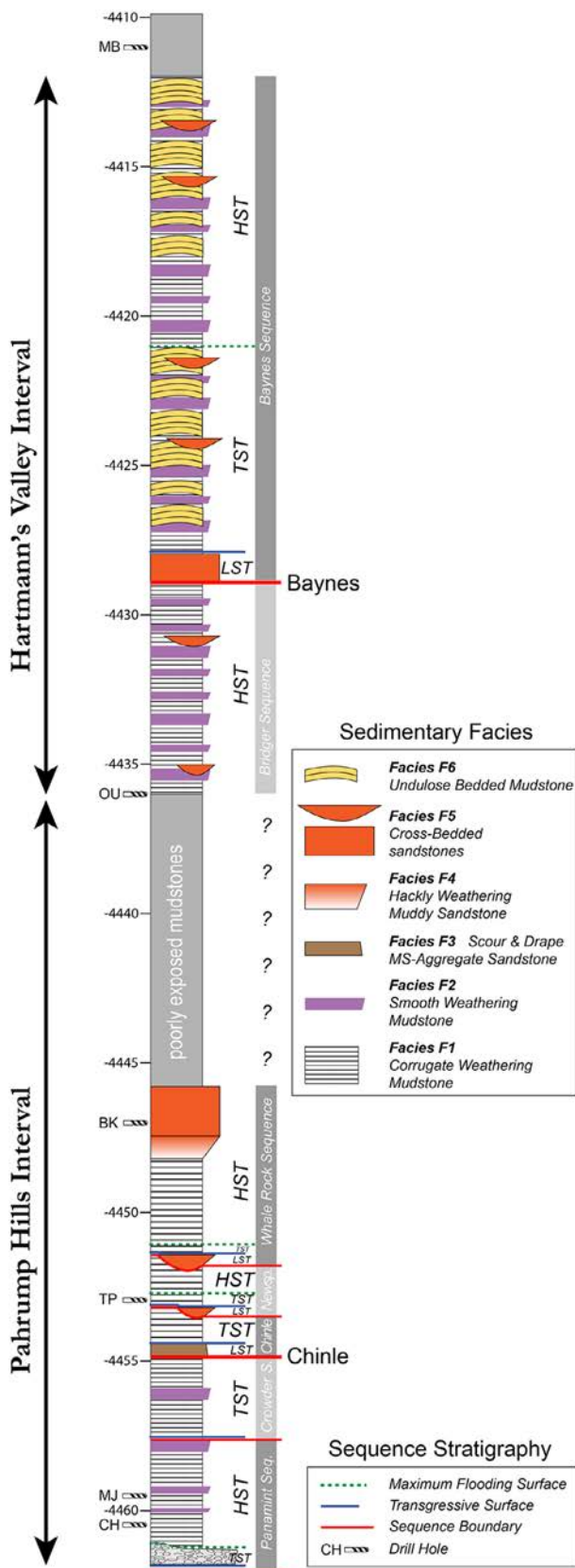


Fig. 33. Summarized stratigraphic succession and facies distribution in the Pahrump Hills through to Hartmann's Valley stratigraphic interval. Interpreted sequence stratigraphic elements and subdivisions are noted right of the column. Note that sequence stratigraphic resolution is significantly higher for the Pahrump Hills outcrop (Schieber *et al.*, 2022) than for the HVi. This difference is largely due to lower exposure quality and data density for the HVi, and thus increased uncertainty about stratigraphic context along a much longer traverse. CheMin analyses are marked to the left of the column (Drill symbol). Note that the BK sample was drilled at the given elevation, but in mudstone lithology (not sandstone) 500 m to the south-west.

stratal stacking patterns and rock composition (related to provenance changes). Thus, the PHi to HVi can be interpreted as containing one complete composite sequence (Abreu, 2010), underlain and overlain by parts of two other composite sequences. At the depositional-sequence-set scale (Fig. 33), the interval below the Chinle SB, composed of F1–F2 parasequences in two depositional sequences (Panamint and Crowd; Schieber *et al.*, 2022, fig. 39) that stack retrogradationally, is interpreted as a transgressive sequence set. The interval between Chinle and Baynes Mountain is interpreted as a composite sequence: the Chinle and Newspaper Rock depositional sequences stack aggradationally, overlain by the Whale Rock progradational depositional sequence, the retrogradational interval between Salsberry Peak and the base of the HVi west, and the progradational basal interval exposed in HVi west. The interval above Baynes Mountain, composed of aggradationally to retrogradationally to progradationally stacked F1–F2–F6 parasequences, is interpreted as the basal interval of a transgressive sequence set (Fig. 33).

DISCUSSION

In an earlier study (Gwizd *et al.*, 2022) the Hartmann's Valley interval was interpreted as an aeolian sandstone unit, a perspective that has been discussed within the Mars Science Laboratory (MSL) team for several years (e.g. Gwizd *et al.*, 2018; Schieber, 2018). Main areas of disagreement are the presumed dominance of

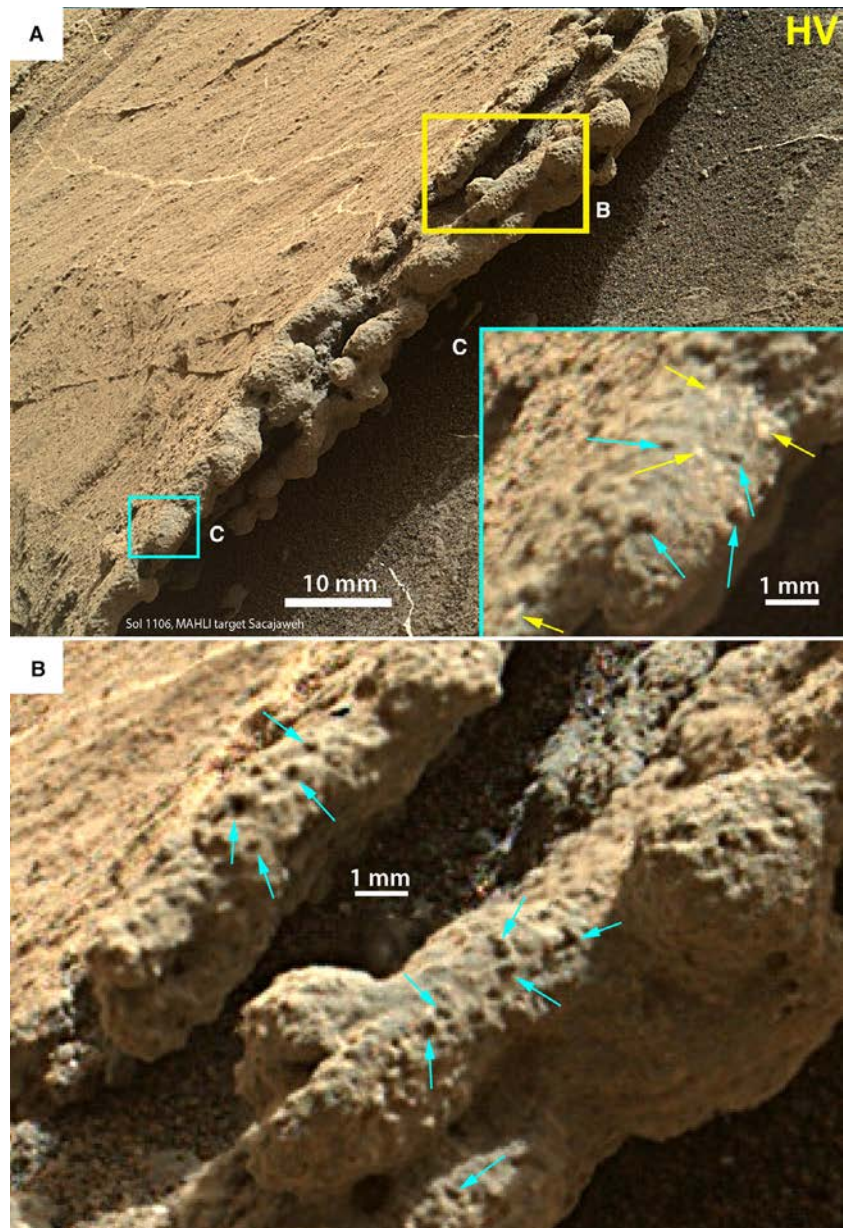


Fig. 34. A closer look at target Sacajawea. (A) An overview that shows its nature of coalescing stratiform concretions. Subframes (B) and (C) show enlarged views of portions of Sacajawea. (B) Concretion surface with numerous sub-millimetre angular holes (blue arrows). (C) Concretion with holes as seen in (B), and in addition whitish objects (interpreted as sand grains by Gwizd *et al.*, 2022) that are in the same size range as the holes that the authors interpret as evaporite grains formed *in situ*.

sandy strata and of aeolian cross-stratification. These interpretations can be re-evaluated via careful examination of high resolution MAHLI images, consideration of ChemCam Gini analyses (Rivera-Hernández *et al.*, 2020), and the identification criteria for large-scale aeolian cross-bedding. As detailed in the following paragraphs, the available observations clearly point to an alternative interpretation of dominantly lacustrine mudstone deposition for the Hartmann's Valley interval.

High spatial resolution image analyses

Gwizd *et al.* (2022) argued that presumed sand grains are not resolvable in MAHLI images of the HVi because of: “resolution limitations and a lack of ubiquitous visible grain boundaries.” Gwizd *et al.* (2022) point to a location near the base of the HVi as a place with medium sand-size grains, the Sol 1106 Sacajawea target. Sacajawea, however, appears to be a lens-shaped body of coalescing concretions (Figs 6 and 34).

The surface of these concretions shows numerous sub-millimetre angular holes as well as whitish objects with straight margins that are in the same range of size and shape as the holes. The whitish objects were interpreted as sand grains by Gwizd *et al.* (2022). Yet, the context (subjacent and superjacent strata) and the rock textures suggest that the Sacajawea target closely resembles mudstone facies F2 at Pahrump (Schieber *et al.*, 2022, fig. 23). By analogy it can be surmised that the holes and white objects at Sacajawea are equivalent to those in facies F2, where the holes record removal of a soluble fill, and the white objects are preserved evaporite minerals or their pseudomorphs. About 20 cm to the left of Sacajawea, a comparable feature (target Blackjack) was analysed by ChemCam, and white objects returned a Ca-sulphate signal, suggesting by extension that the white objects at Sacajawea are plausibly composed of (or contain) Ca-sulphate. In the context of the Sacajawea target, Gwizd *et al.* (2022) suggested that: “greater resistance to erosion may correlate with a coarser grain-size”. This is completely reasonable because sandstones on Earth tend to be better cemented than intervening mudstones, but such an interpretation fails when concretions and cemented flooding surfaces come into play (Taylor & Macquaker, 2014; Schieber *et al.*, 2022). For example, the erosion resistant ledges in the lower half of the Pahrump Hills exposure (Comb Ridge, Book Cliffs, etc.) are not sandstones, they are well-cemented mudstone horizons (Schieber *et al.*, 2022).

A systematic examination of all high-resolution MAHLI targets from the eastern and western Hartmann’s Valley interval traverses (13 targets in total) did not show any visible sand grains (Fig. 35). Application of the concept of ‘random single pixel variability’, or RSPV (Schieber, 2018; Schieber *et al.*, 2022), to these images suggests that these targets overall are dominated by a mudstone matrix that consists of particles $\leq 20 \mu\text{m}$. None of these images supports the presence of sandstone in the HVi. Building on observations made at Pahrump Hills (Schieber *et al.*, 2022), sub-millimetre to millimetre-scale objects embedded in this matrix are considered likely evaporite mineral pseudomorphs.

ChemCam Gini analyses

In support of their assertion that the HVi consists of sandstones, Gwizd *et al.* (2022), cite a paper by Rivera-Hernández *et al.* (2020), who

used the Gini Index Mean Score (GIMS) calculated from ChemCam LIBS data to derive grain-size information for the Murray formation. Yet, whereas Rivera-Hernández *et al.* (2020) do indeed posit that the GIMS data for the HVi suggest the presence of sandstones, their actual data for the HVi show a narrower spread than for the Pahrump Hills interval, with the majority of data points falling within the GIMS range assigned to mudstones for both intervals. With the PHi clearly mudstone dominated, notwithstanding a few sandstone lenses (Stack *et al.*, 2019; Schieber *et al.*, 2022), this implies that the HVi should be at least as muddy as the PHi while allowing for some sandstone bodies of limited extent. The GIMS approach is in essence an assessment of compositional (chemical) heterogeneity, where in the case of a sandstone, successive ChemCam laser shots (*ca* 0.5 mm diameter ablation spots) may show stronger differences in composition than if a mudstone was targeted where the laser spot is much larger than the grain size. As such, GIMS is not really a sandstone detection tool, because a mudstone with disseminated sand grains or pseudomorphs of evaporite minerals could give comparable GIMS values. Indeed, as discussed above, the sporadic Ca-sulphate detections throughout the entire vertical extent of the HVi by ChemCam can be modelled as disseminated Ca-sulphate sand-sized grains (about 200 μm) in the mudstone matrix (Appendix S4).

Absence of large-scale aeolian cross-bedding

The main rationale for the proposed sandstone dominated nature of the HVi (Gwizd *et al.*, 2022) seems to have been the interpretation that a significant proportion of HVi outcrops are cross-stratified at a multi-metre scale, a circumstance that would indeed call for sand-size grains. However, as detailed in the *Facies F6, undulose bedded mudstone* section, the layering that is interpreted as aeolian cross-beds does not even exhibit the essential characteristics of cross-bedding: pervasive and widespread stratiform terminations (Campbell, 1967; Rubin, 1987). Instead the variably dipping layers in the F6 intervals are clearly continuous and convex-up across the crests of anticlinal/roll-over features (Figs 18) and no decimetre to metre-scale downlapping laminae were observed. Moreover, even if these strata contained cross-bedding at the decimetre to metre-scale, simple and even compound cross-beds at such scales are quite

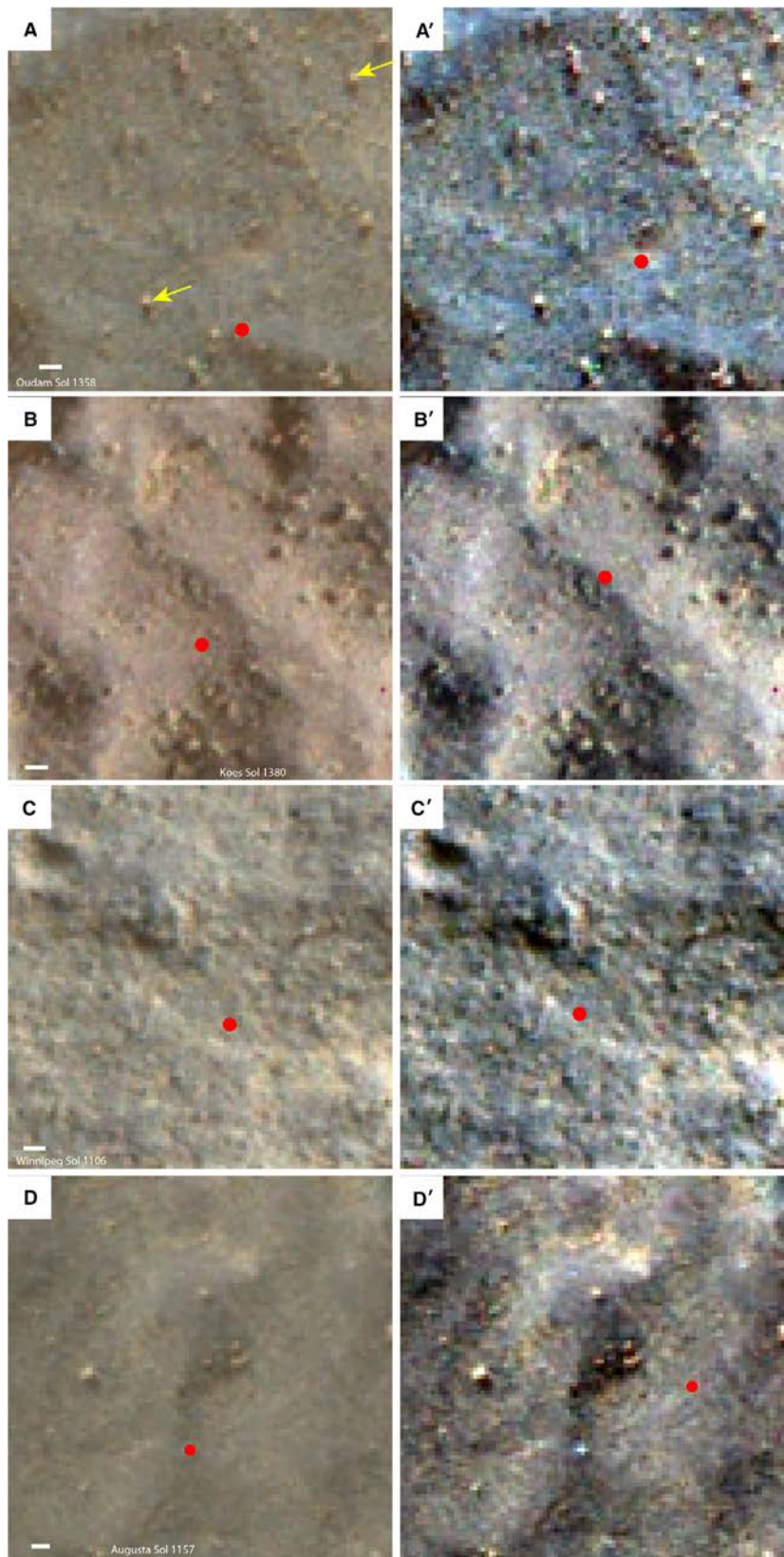


Fig. 35. Examples of Hartmann's Valley MAHLI targets at the pixel scale that the authors interpret as mudstones. Images in the left column are largely dust-free subsamples (100 by 100 pixels) from high magnification MAHLI targets. (A) From target Oudam (Sol 1358); (B) from target Koes (Sol 1380); (C) from target Winnipeg (Sol 1106); and (D) from target Augusta (Sol 1157). The white scale bar in each image is 100 μm long and the red circles are the size of a coarse silt grain (62.5 μm). Surface dust particles (yellow arrows) are easily identified because of dark shadows that are all on the same side of particles. There are abundant areas in these frames that show the RSPV characteristics that indicate a medium mudstone matrix, although they may contain scattered objects of coarse silt size. The column of images on the right (A', B', C' and D') are versions with strongly enhanced contrast relative to the originals on the left, and even at high contrast the RSPV characteristics persist.

common in subaqueous flows on Earth (Reineck & Singh, 1980; Rubin, 1987; Southard & Boguchwal, 1990). More confident interpretation of an aeolian origin for compound cross-bedding relies not only on the scale of the bedding but, more critically, on the presence of closely associated grain flow, grain fall and climbing translatent (wind-ripple) bedding (Hunter, 1977; Kocurek & Dott, 1981; Pye & Tsoar, 2009) – none of which are observed and reported to occur in the HVi. In addition, the MAHLI images of F6 (target Swartkloofberg, Fig. 21) do not reveal sand grains but suggest that the undulose bedded strata are a coarse mudstone (*Facies F6, undulose bedded mudstone* section), *sensu* Lazar *et al.* (2015).

Thus, a predominantly aeolian sandstone interpretation for the HVi is unlikely because of the lack of both sand and pervasive cross-stratification. Instead, the prevalence of mudstones with characteristics familiar from the underlying PHi suggest that the HVi overall represents a continuation of the lacustrine conditions observed in the underlying Pahrump Hills interval (underfilled evaporitic lake system). Subtle differences between the PHi and the HVi are an apparent increase in the intensity of evaporitic conditions (Fig. 29), and the addition of undulose bedded mudstones (facies F6) as a consequence of intermittent freshening and deposition of prodeltaic mudlobes.

CONCLUSIONS

In contrast to prior studies (Gwizd *et al.*, 2022), the presented observations show that sandstones constitute only a minor proportion of the strata in the Hartmann's Valley stratigraphic interval and that it is instead strongly dominated by mudstones. The majority of these mudstones very closely resemble the evaporitic lacustrine mudstones (facies F1 and F2) already described from the underlying Pahrump Hills succession (Schieber *et al.*, 2022), fine to coarse detrital mudstones with abundant sediment-incorporative evaporite pseudomorphs. A new mudstone facies, the undulose bedded mudstones (facies F6), is interbedded with these evaporitic mudstones and is interpreted to record prodeltaic mudlobes that were deposited during time periods of increased water and sediment supply to the lake.

Distinct differences between the vertical facies successions of the eastern and western rover

traverses (Figs 26 and 27) indicate substantial lateral changes in depositional conditions, i.e. areas offshore of deltaic depocentres versus areas between depocentres where deposition was dominated by lacustrine laminites (facies F1 and F2). The absence of obvious compositional differences between Hartmann's Valley strata examined along the eastern versus western transects (Figs 1, 28 and 30; Thompson *et al.*, 2020), suggests sediment homogenization in extensive external catchments that fed water and sediment into the crater.

Rather than recording a significant change in depositional conditions from the underlying Pahrump Hills strata (Gwizd *et al.*, 2022), it appears that boundary conditions during deposition of the HVi largely remained the same. Upward compositional changes in the Pahrump Hills through to Hartmann's Valley succession are likely due to adjustments of drainage and changing source materials over time. The most conspicuous compositional change, plausibly reflecting a change from minimally to moderately weathered source material, occurs across the Chinle unconformity (Fig. 28). Because of the time needed to provide a reservoir of notably more weathered detritus for deposition above Chinle, a significant hiatus in sediment supply is implicated. Fluvial sediment supply to Gale crater's interior is conditioned on flowing water, thus this gap of deposition implies a long post-Chinle dry spell that may have planet-wide implications.

A major system reset above Chinle is supported by the first detection of tridymite and cristobalite, a pair of tracer minerals that were detected from just above Chinle to the base of the HVi. Tridymite and cristobalite in the Murray formation have been variably ascribed to silicic volcanics, *in situ* hydrothermal alteration, or meteorite impacts. In light of the ubiquity of meteorite impact activity early in Martian history and the heavily cratered Noachian upper crust, the considerable stratigraphic range (17 m) as well as the small crystallite size and high strain parameters of these high-temperature silica polymorphs makes it most plausible that both minerals were sourced from impact-related debris and melt sheets.

Documentation of common matrix sulphate in the HVi points to an increase in the intensity of evaporitic conditions relative to the PHi, whereas intercalated prodeltaic mudlobes suggest intermittent freshening and increased sediment supply. As such, salinity variations and

water level fluctuations may have been greater during deposition of the HVi, even though the system boundary conditions were largely the same and the lake system remained in a stable underfilled lake-basin mode – as commonly observed for such systems on Earth. Thus, given the relatively stable physical-boundary conditions at Gale, the large volume of potential accommodation of the crater, and the emergent behaviour typical of lake systems, such environmental continuity can be expected to span even more of the Murray formation, enhancing potential habitability.

ACKNOWLEDGEMENTS

This work results from MSL science activities performed at the Jet Propulsion Laboratory, California Institute of Technology, under contract with the National Aeronautics and Space Administration. The authors are grateful to the entire MSL Science team and the MSL engineering and operations teams, for generating these exceptional data. The Malin Space Sciences operations team is thanked for the high quality images that form the basis of this project. Our sincere thanks also go to the reviewers and editors, Drs Kevin Taylor, Jeff Pietras and V.P. Wright, who provided us with abundant and helpful suggestions on how to streamline the manuscript and much improved readability. We extend a very special thanks to Ken Edgett for agreeing to look over an earlier version of this manuscript, and by drawing on his deep well of operational and tactical knowledge, provided some guard rails to keep us from straying too far into the realm of wishful thinking.

DATA AVAILABILITY STATEMENT

The data utilized for preparation of this study are archived in the NASA Planetary Data System (pds.nasa.gov).

REFERENCES

- Abreu, V.** (Ed.) (2010) *Sequence Stratigraphy of Siliciclastic Systems: The ExxonMobil Methodology; Atlas of Exercises*, Vol. 9. SEPM Society for Sedimentary Geology, Tulsa, OK.
- Anderson, R.B.** and **Bell, J.F., III** (2010) Geologic mapping and characterization of Gale crater and implications for its potential as a Mars Science Laboratory landing site. *Mars*, **5**, 76–128.
- Arp, G., Schultz, S., Karius, V.** and **Head, J.W., III** (2019) Ries impact crater sedimentary conglomerates: sedimentary particle 'impact pre-processing', transport distances and provenance, and implications for Gale crater conglomerates, Mars. *Icarus*, **321**, 531–549.
- Aydar, E.** (1998) Early Miocene to quaternary evolution of volcanism and the basin formation in western Anatolia: a review. *J. Volcanol. Geoth. Res.*, **85**, 69–82.
- Baganz, O., Bartov, Y., Bohacs, K.M.** and **Nummedal, D.** (Eds) (2013) Lacustrine sandstone reservoirs and hydrocarbon systems. *AAPG Mem.*, **95**, 517.
- Banham, S.G., Gupta, S., Rubin, D.M., Bedford, C.C., Edgar, L.A., Bryk, A.B., Dietrich, W.E., Fedo, C.M., Williams, R.M., Caravaca, G., Barnes, R., Paar, G., Ortner, T.** and **Vasavada, A.R.** (2022) Evidence for fluctuating wind in shaping an ancient Martian dune field: the Stimson formation at the Greenheugh pediment, Gale crater. *J. Geophys. Res. Planets*, **127**, e2021JE007023.
- Banham, S.G., Gupta, S., Rubin, D.M., Edgett, K.S., Barnes, R., Van Beek, J., Watkins, J.A., Edgar, L.A., Fedo, C.M., Williams, R.M., Stack, K.M., Grotzinger, J.P., Lewis, K., Ewing, R.C., Day, M.** and **Vasavada, A.R.** (2021) A rock record of complex aeolian bedforms in a Hesperian desert landscape: the Stimson formation as exposed in the Murray buttes, Gale crater, Mars. *J. Geophys. Res. Planets*, **126**, e2020JE006554.
- Banham, S.G., Gupta, S., Rubin, D.M., Watkins, J.A., Sumner, D.Y., Edgett, K.S., Grotzinger, J.P., Lewis, K.W., Edgar, L.A., Stack-Morgan, K.M., Barnes, R., Bell, J.F., III, Day, M.D., Ewing, R.C., Lapotre, M.G.A., Stein, N.T., Rivera-Hernandez, F.** and **Vasavada, A.R.** (2018) Ancient Martian aeolian processes and palaeomorphology reconstructed from the Stimson formation on the lower slope of Aeolis Mons, Gale crater, Mars. *Sedimentology*, **65**, 993–1042.
- Bartov, Y., Stein, M., Enzel, Y., Kendall, C.** and **Moore, P.** (2012) Modeling the sensitivity to environmental controls of the Late Pleistocene Lacustrine Delta sequences in the Dead Sea Basin. In: *Lacustrine Sandstone Reservoirs and Hydrocarbon Systems* (Eds Baganz, O.W., Bartov, Y., Bohacs, K. and Nummedal, D.), *AAPG Mem.*, **95**, 417–431.
- Bedford, C.** (2019) Distinguishing the geochemical effects of sedimentary processes and source region characteristics in Gale Crater, Mars. Doctoral dissertation, The Open University.
- Benavente, C.** and **Bohacs, K.** (2024) Advances in Limnogeology: The lake-basin-type model revisited 25 years after... anomalies, conundrums and upgrades. *Depositional Rec.* <https://doi.org/10.1002/dep2.280>.
- Bohacs, K.M., Carroll, A.R.** and **Neal, J.E.** (2003) Lessons from large lake systems—thresholds, nonlinearity, and strange attractors. In: *Extreme Depositional Environments: Mega End Members in Geologic Time* (Eds Chan, M.A. and Archer, A.W.), *Geol. Soc. Am. Spec. Pap.*, **370**, 75–90.
- Bohacs, K.M., Carroll, A.R., Neal, J.E.** and **Mankiewicz, P.J.** (2000) Lake-basin type, source potential, and hydrocarbon character: an integrated sequence-stratigraphic–geochemical framework. In: *Lake Basins Through Space and Time* (Eds Gierlowski-Kordesch, E.H. and Kelts, K.R.), *AAPG Stud. Geol.*, **46**, 3–33.
- Bohacs, K.M., Carroll, A.R., Pietras, J., Rhodes, M.** and **Smith, M.** (2002) Evolution of the great lakes system of the Green River Formation: tectonically and topographically conditioned records of climate change. In: *Geological Society of America Abstracts with Programs* (Vol. 34, 478 pp.).

- Bohacs, K.M., Grabowski, G.J., Jr., Carroll, A.R., Miskell-Gerhardt, K.J. and Glaser, K.** (2007) Lithofacies architecture and sequence stratigraphy of the Green River Formation, greater Green River Basin, Wyoming and Colorado. *Mt. Geol.*, **44**, 39–60.
- Bohacs, K.M., Lazar, O.R. and Demko, T.M.** (2014) Parasequence types in shelfal mudstone strata—quantitative observations of lithofacies and stacking patterns, and conceptual link to modern depositional regimes. *Geology*, **42**, 131–134.
- Brabets, T.P.** (1992) Hydrologic Data for the Lower Cooper River, Alaska – May to September 1991: USGS Open File Report 92-89, 15 pp.
- Bradley, W.H.** (1964) Geology of Green River Formation and associated Eocene rocks in southwestern Wyoming and adjacent parts of Colorado and Utah. Geological Survey professional paper: 496-A.
- Campbell, C.V.** (1967) Lamina, laminaset, bed, bedset. *Sedimentology*, **8**, 7–26.
- Campo, B., Morelli, A., Amorosi, A., Bruno, L., Scarponi, D., Rossi, V., Bohacs, K. and Drexler, T.** (2022) Chapter 15: Last-glacial-maximum depositional sequence, Po River Plain, Italy—ultra-high resolution sequence stratigraphy of a Cenozoic coastal-plain-to-shallow-marine foreland basin. In: *Sequence Stratigraphy: Applications to Fine-Grained Rocks* (Eds Bohacs, K.M. and Lazar, O.R.), AAPG Mem. **126**, 537–598.
- Cavosie, A.J., Spencer, C.J., Evans, N., Rankenburg, K., Thomas, R.J. and Macey, P.H.** (2022) Granular titanite from the Roter Kamm crater in Namibia: product of regional metamorphism, not meteorite impact. *Geosci. Front.*, **13**, 101350.
- Cioni, R., Fanelli, G., Guidi, M., Kinyariro, J.K. and Marini, L.** (1992) Lake Bogoria hot springs (Kenya): geochemical features and geothermal implications. *J. Volcanol. Geoth. Res.*, **50**, 231–246.
- Cohen, A.S.** (2003) *Paleolimnology: The History and Evolution of Lake Systems*, p. 528. Oxford University Press, Oxford.
- Conrad, C., Rahmann, M., Machwitz, M., Stulina, G., Paeth, H. and Dech, S.** (2013) Satellite based calculation of spatially distributed crop water requirements for cotton and wheat cultivation in Fergana Valley, Uzbekistan. *Glob. Planet. Chang.*, **110**(A), 88–98.
- Conrad, C.P.** (2013) The solid Earth's influence on sea level. *Bulletin*, **125**, 1027–1052.
- Crusius, J., Schroth, A.W., Gasso, S., Moy, C.M., Levy, R.C. and Gatica, M.** (2011) Glacial flour dust storms in the Gulf of Alaska: hydrologic and meteorological controls and their importance as a source of bioavailable iron. *Geophys. Res. Lett.*, **38**, L06602.
- Davis, K., Herman, J., Maksymuk, M., Wilson, J., Chu, P., Burke, K., Janduara, L. and Brown, K.** (2012) Mars Science Laboratory's Dust Removal Tool. 41st Aerospace Mechanisms Symposium, Pasadena, CA, May 16–18, 2012. NASA Conf. Proc. NASA/CP-2012-217653, pp. 279–292.
- Day, M. and Kocurek, G.** (2016) Observation of an aeolian landscape: from surface to orbit in Gale crater. *Icarus*, **280**, 37–71.
- De Cort, G.** (2016) Holocene hydroclimate reconstruction in East Africa, based on multi-proxy analysis of lake sediments. Doctoral dissertation, Ghent University, 190 pp.
- Edgar, L.A., Gupta, S., Rubin, D.M., Lewis, K.W., Kocurek, G.A., Anderson, R.B., Bell, J.F., III, Dromart, G., Edgett, K.S., Grotzinger, J.P., Hardgrove, G., Kah, L.C., Leveille, R., Malin, M.C., Mangold, N., Milliken, R.E., Miniti, M., Palucis, M., Palucis, M., Rowland, S.K., Schieber, J., Stack, K.M., Sumner, D.Y., Wiens, R.C., Williams, R.M.E. and Williams, A.J.** (2018) Shaler: in situ analysis of a fluvial sedimentary deposit on Mars. *Sedimentology*, **65**, 96–122.
- Edgett, K.S. and Malin, M.C.** (2002) Martian sedimentary rock stratigraphy: outcrops and interbedded craters of northwest Sinus Meridiani and southwest Arabia Terra. *Geophys. Res. Lett.*, **29**, 2179.
- Edgett, K.S., Yingst, R.A., Ravine, M.A., Caplinger, M.A., Maki, J.N., Ghaemi, F.T., Schaffner, J.A., Bell, J.F., III, Edwards, L.J., Herkenhoff, K.E., Heydari, E., Kah, L.C., Lemmon, M.T., Miniti, M.E., Olson, T.S., Parker, T.J., Rowland, S.K., Schieber, J., Sullivan, R.J., Sumner, D.Y., Thomas, P.C., Jensen, E.H., Simmonds, J.J., Sengstacken, A.J., Willson, R.G. and Goetz, W.** (2012) Curiosity's Mars hand lens imager (MAHLI) investigation. *Space Sci. Rev.*, **170**, 259–317.
- Ehlmann, B.L. and Edwards, C.S.** (2014) Mineralogy of the Martian surface. *Annu. Rev. Earth Planet. Sci.*, **42**, 291–315.
- Eldridge, L.** (2018) Working on Mars – an immersive encounter through the screen. In: *Image – Action – Space: Situating the Screen in Visual Practice* (Eds Feiersinger, L., Friedrich, K. and Queisner, M.), pp. 103–113. de Gruyter, Berlin.
- Ewing, R.C., Lapotre, M.G.A., Lewis, K.W., Day, M., Stein, N., Rubin, D.M., Sullivan, R., Banham, S., Lamb, M.P., Bridges, N.T., Gupta, S. and Fischer, W.W.** (2017) Sedimentary processes of the Bagnold Dunes: implications for the eolian rock record of Mars. *J. Geophys. Res. Planets*, **122**, 2544–2573.
- Fedo, C.M., Bryk, A.B., Edgar, L.A., Bennett, K.A., Fox, V.K., Dietrich, W.E., Banham, S.G., Gupta, S., Stack, K.M., Williams, R.M.E., Grotzinger, J.P., Stein, N.T., Rubin, D.M., Caravaca, G., Arvidson, R.E., Hughes, M.N., Fraeman, A.A., Vasavada, A.R., Schieber, J. and Sutter, B.** (2022) Geology and stratigraphic correlation of the Murray and Carolyn Shoemaker formations across the Glen Torridon region, Gale crater, Mars. *J. Geophys. Res. Planets*, **127**, e2022JE007408.
- Fedo, C.M., Grotzinger, J.P., Gupta, S., Fraeman, A., Edgar, L., Edgett, K., Stein, N., Rivera-Hernandez, F., Lewis, K., Stack, K.M., House, C., Rubin, D. and Vasavada, A.R.** (2018) Sedimentology and stratigraphy of the Murray formation, Gale crater, Mars. 49th Lunar and Planetary Science Conference, The Woodlands, Texas, USA, March 19–23, 2018, 2078 pp.
- Fenton, L.K., Bandfield, J.L. and Ward, A.W.** (2003) Aeolian processes in Proctor Crater on Mars: sedimentary history as analyzed from multiple data sets. *J. Geophys. Res. Planets*, **108**, 5129.
- Gellert, R., Clark, B.C., III and MSL and MER Science Teams** (2015) In situ compositional measurements of rocks and soils with the alpha particle x-ray spectrometer on NASA's Mars rovers. *Elements*, **11**, 39–44.
- Gierlowski-Kordesch, E. and Kelts, K.** (1994) *Global Geological Record of Lake Basins*, p. 427. Cambridge University Press, Cambridge.
- Gierlowski-Kordesch, E. and Kelts, K.** (2000) Lake basins through space and time. *AAPG Stud. Geol.*, **46**, 648.
- Grant, J.A., Wilson, S.A., Mangold, N., Calef, F., III and Grotzinger, J.P.** (2014) The timing of alluvial activity in Gale crater, Mars. *Geophys. Res. Lett.*, **41**, 1142–1149.

- Grotzinger, J.P., Crisp, J., Vasavada, A.R., Anderson, R.C., Baker, C.J., Barry, R., Blake, D.F., Conrad, P., Edgett, K.S., Ferdowski, B., Gellert, R., Gilbert, J.B., Golombek, M., Gómez-Elvira, J., Hassler, D.M., Jandura, L., Litvak, M., Mahaffy, P., Maki, J., Meyer, M., Malin, M.C., Mitrofanov, I., Simmonds, J.J., Vaniman, D., Welch, R.V. and Wiens, R.C. (2012) Mars science laboratory mission and science investigation. *Space Sci. Rev.*, **170**, 5–56.
- Grotzinger, J.P., Gupta, S., Malin, M.C., Rubin, D.M., Schieber, J., Siebach, K., Sumner, D.Y., Stack, K.M., Vasavada, A.R., Arvidson, R.E., Calef, F., III, Edgar, L., Fischer, W.F., Grant, J.A., Griffes, J., Kah, L.C., Lamb, M.P., Lewis, K.W., Mangold, N., Minitti, M.E., Palucis, M., Rice, M., Williams, R.M.E., Yingst, R.A., Blake, D., Blaney, D., Conrad, P., Crisp, J., Dietrich, W.E., Dromart, G., Edgett, K.S., Ewing, R.C., Gellert, R., Hurowitz, J.A., Kocurek, G., Mahaffy, P., McBride, M.J., McLennan, S.M., Mischna, M., Ming, D., Milliken, R., Newsom, H., Oehler, D., Parker, T.J., Vaniman, D., Wiens, R.C. and Wilson, S.A. (2015) Deposition, exhumation, and paleoclimate of an ancient lake deposit, Gale crater, Mars. *Science*, **350**, aac7575.
- Grotzinger, J.P., Sumner, D.Y., Kah, L.C., Stack, K., Gupta, S., Edgar, L., Rubin, D., Lewis, K., Schieber, J., Mangold, N., Milliken, R., Conrad, P.G., DesMarais, D., Farmer, J., Siebach, K., Calef, F., 3rd, Hurowitz, J., McLennan, S.M., Ming, D., Vaniman, D., Crisp, J., Vasavada, A., Edgett, K.S., Malin, M., Blake, D., Gellert, R., Mahaffy, P., Wiens, R.C., Maurice, S., Grant, J.A., Wilson, S., Anderson, R.C., Beegle, L., Arvidson, R., Hallet, B., Sletten, R.S., Rice, M., Bell, J., 3rd, Griffes, J., Ehlmann, B., Anderson, R.B., Bristow, T.F., Dietrich, W.E., Dromart, G., Eigenbrode, J., Fraeman, A., Hardgrove, C., Herkenhoff, K., Jandura, L., Kocurek, G., Lee, S., Leshin, L.A., Leveille, R., Limonadi, D., Maki, J., McCloskey, S., Meyer, M., Minitti, M., Newsom, H., Oehler, D., Okon, A., Palucis, M., Parker, T., Rowland, S., Schmidt, M., Squyres, S., Steele, A., Stolper, E., Summons, R., Treiman, A., Williams, R., Yingst, A. and MSL Science Team (2014) A habitable fluvio-lacustrine environment at Yellowknife Bay, Gale Crater, Mars. *Science*, **343**, 1242777.
- Gwizd, S., Fedo, C., Grotzinger, J., Banham, S., Rivera-Hernández, F., Stack, K.M., Siebach, K., Thorpe, M., Thompson, L., O'Connell-Cooper, C., Stein, N., Edgar, L., Gupta, S., Rubin, D., Sumner, D. and Vasavada, A.R. (2022) Sedimentological and geochemical perspectives on a marginal lake environment recorded in the Hartmann's Valley and Karasburg members of the Murray formation, Gale crater, Mars. *J. Geophys. Res. Planets*, **127**, e2022JE007280.
- Gwizd, S., Fedo, C., Grotzinger, J., Edgett, K., Rivera-Hernandez, F. and Stein, N. (2018) Depositional history of the Hartmann's valley member, Murray formation, Gale crater, Mars. In the 49th Lunar and Planetary Science Conference, Abstract #2150.
- Hall, J.K. (1996) Digital topography and bathymetry of the area of the Dead Sea depression. *Tectonophysics*, **266**, 177–185.
- Hartmann, W.K. and Neukum, G. (2001) Cratering chronology and the evolution of mars. In: *Chronology and Evolution of Mars. Space Sciences Series of ISSI*, Vol. 12 (Eds Kallenbach, R., Geiss, J. and Hartmann, W.K.), pp. 165–194. Springer, Dordrecht.
- Heins, W.A. and Kairo, S. (2007) Predicting sand character with integrated genetic analysis. In: *Sedimentary Provenance and Petrogenesis: Perspectives from Petrography and Geochemistry* (Eds Arribas, J., Critelli, S. and Johnsson, M.J.), *Geol. Soc. Am. Spec. Pap.* **420**, 345–379.
- Hickley, P., Boar, R.R. and Mavuti, K.M. (2003) Bathymetry of Lake Bogoria, Kenya. *J. East Afr. Nat. Hist.*, **92**, 107–117.
- Horwell, C.J., Williamson, B.J., Llewellyn, E.W., Damby, D.E. and le Blond, J.S. (2013) The nature and formation of cristobalite at the Soufrière Hills volcano, Montserrat: implications for the petrology and stability of silicic lava domes. *Bull. Volcanol.*, **75**, 696.
- Howe, T. (2017) The evolution and stratigraphic architecture of fluvio-lacustrine deltas: reservoir characteristics from the red River Delta, Lake Texoma and the Denton Creek Delta, Grapevine Lake, TX. Doctoral dissertation, Texas Christian University.
- Hunter, R.E. (1977) Basic types of stratification in small eolian dunes. *Sedimentology*, **24**, 361–387.
- Inbar, M. (1987) Effects of a high magnitude flood in a Mediterranean climate: a case study in the Jordan River basin. In: *Catastrophic Flooding* (Eds Mayer, L. and Nash, D.), pp. 333–353. London, UK, Allen & Unwin.
- Jackson, J.C., Wright, H.J., Chou, I.-M. and Belkin, H.E. (2011) Monoclinic tridymite in clast-rich impact melt rock from the Chesapeake Bay impact structure. *Am. Mineral.*, **96**, 81–88.
- Johnson, C.L. and Graham, S.A. (2004) Sedimentology and reservoir architecture of a synrift lacustrine delta, Southeastern Mongolia. *J. Sed. Res.*, **74**, 770–785.
- Kah, L.C., Stack, K.M., Eigenbrode, J.L., Yingst, R.A. and Edgett, K.S. (2018) Syndepositional precipitation of calcium sulfate in Gale Crater, Mars. *Terra Nova*, **30**, 431–439.
- Kataoka, K.S. and Nagahashi, Y. (2019) From sink to volcanic source: unravelling missing terrestrial eruption records by characterization and high-resolution chronology of lacustrine volcanic density flow deposits, Lake Inawashiro-ko, Fukushima, Japan. *Sedimentology*, **66**, 2784–2827.
- Kelts, K. and Hsü, K.J. (1978) Freshwater carbonate sedimentation. In: *Lakes: Chemistry, Geology, Physics* (Ed Lerman, A.), pp. 295–323. Springer-Verlag, New York, NY.
- Kenkmann, T., Poelchau, M.H. and Wulf, G. (2014) Structural geology of impact craters. *J. Struct. Geol.*, **62**, 156–182.
- Kocurek, G. and Dott, R.H. (1981) Distinctions and uses of stratification types in the interpretation of eolian sand. *J. Sed. Res.*, **51**, 579–595.
- Lang, S.C., Payenberg, T.H.D., Reilly, M.R.W., Hicks, T., Benson, J. and Kassan, J. (2004) Modern analogues for dryland sandy fluvial-lacustrine deltas and terminal splay reservoirs. *APPEA J.*, **44**, 329–356.
- Lazar, O.R., Bohacs, K.M., Schieber, J., Macquaker, J.H.S. and Demko, T.M. (2022) Mudstone nomenclature. In: *Sequence stratigraphy: Applications to fine-grained rocks* (Eds Bohacs, K.M. and Lazar, O.R.), Vol. **126**, pp. 21–34. AAPG Memoir, Tulsa, OK.
- Lazar, O.R., Bohacs, K.M., Macquaker, J.H.S., Schieber, J. and Demko, T.M. (2015) Capturing key attributes of fine-grained sedimentary rocks in outcrops, cores, and thin sections: nomenclature and description guidelines. *J. Sediment. Res.*, **85**, 230–246.
- Le Deit, L., Hauber, E., Fueten, F., Pondrelli, M., Rossi, A.P. and Jaumann, R. (2013) Sequence of infilling events in Gale Crater, Mars: results from morphology, stratigraphy, and mineralogy. *J. Geophys. Res. Planets*, **118**, 2439–2473.

- Li, Z., Schieber, J. and Pedersen, P.K.** (2021) On the origin and significance of composite particles in mudstones: examples from the Cenomanian Dunvegan Formation. *Sedimentology*, **68**, 737–754.
- Malin, M.C. and Edgett, K.S.** (2000) Sedimentary rocks of early Mars. *Science*, **290**, 1927–1937.
- Mangold, N., Baratoux, D., Arnalds, O., Bardintzeff, J.M., Platevoet, B., Grégoire, M. and Pinet, P.** (2011) Segregation of olivine grains in volcanic sands in Iceland and implications for Mars. *Earth Planet. Sci. Lett.*, **310**, 233–243.
- Mangold, N., Dehouck, E., Fedo, C., Forni, O., Achilles, C., Bristow, T., Downs, R.T., Frydenvang, J., Gasnault, O., L'Haridon, J., Le Deit, L., Maurice, S., McLennan, S.M., Meslin, P.-Y., Morrison, S., Newsom, H.E., Rampe, E., Rapin, W., Rivera-Hernandez, F., Salvatore, M. and Wiens, R.C.** (2019) Chemical iteration of fine-grained sedimentary rocks at Gale crater. *Icarus*, **321**, 619–631.
- Manville, V., Németh, K. and Kano, K.** (2009) Source to sink: a review of three decades of progress in the understanding of volcaniclastic processes, deposits, and hazards. *Sed. Geol.*, **220**, 136–161.
- Maurice, S., Wiens, R.C., et al.** (2012) The ChemCam instrument suite on the Mars Science Laboratory (MSL) rover: Science objectives and mast unit description. *Space Sci. Rev.*, **170**, 95–166.
- McSween, H.Y., Wyatt, M.B., Gellert, R., Bell, J.F., III, Morris, R.V., Herkenhoff, K.E., Crumpler, L.S., Milam, K.A., Stockstill, K.R., Tornabene, L.L. and Arvidson, R.E.** (2006) Characterization and petrologic interpretation of olivine-rich basalts at Gusev Crater, Mars. *J. Geophys. Res. Planets*, **111**, E02S10.
- Milliken, R.E., Grotzinger, J.P. and Thomson, B.J.** (2010) Paleoclimate of Mars as captured by the stratigraphic record in Gale crater. *Geophys. Res. Lett.*, **37**, L04201.
- Minitti, M.E., Malin, M.C., Van Beek, J.K., Caplinger, M., Maki, J.N., Ravine, M., Calef, F.J., III, Edgar, L.A., Harker, D., Herkenhoff, K.E., Kah, L.C., Kennedy, M.R., Krezoski, G.M., Kronyak, R.E., Lipkaman, L., Nixon, B., Rowland, S.K., Schieber, J., Schroeder, J.F., Stack, K.M., Williams, R.M.E. and Yingst, R.A.** (2019) Distribution of primary and secondary features in the Pahrump Hills outcrop (Gale crater, Mars) as seen in a Mars Descent Imager (MARDI) “sidewalk” mosaic. *Icarus*, **328**, 194–209.
- Morris, R.V., Vaniman, D.T., Blake, D.F., Gellert, R., Chipera, S.J., Rampe, E.B., Ming, D.W., Morrison, S.M., Downs, R.T., Treiman, A.H., Yen, A.S., Grotzinger, J.P., Achilles, C.N., Bristow, T.F., Crisp, J.A., Des Marais, D.J., Farmer, J.D., Fendrich, K.V., Frydenvang, J., Graff, T.G., Morookian, J.M., Stolper, E.M. and Schwenthaler, S.P.** (2016) Silicic volcanism on Mars evidenced by tridymite in high-SiO₂ sedimentary rock at Gale crater. *Proc. Natl Acad. Sci. USA*, **113**, 7071–7076.
- Mtelela, C., Roberts, E.M., Downie, R. and Hendrix, M.S.** (2016) Interplay of structural, climatic, and volcanic controls on late quaternary lacustrine–deltaic sedimentation patterns in the western branch of the East African Rift System, Rukwa Rift Basin, Tanzania. *J. Sed. Res.*, **86**, 1179–1207.
- Nemec, W.** (1995) The dynamics of deltaic suspension plumes. In: *Geology of Deltas* (Eds Oti, M.N. and Postma, G.), pp. 31–93. Balkema, Rotterdam.
- Nesbitt, H. and Young, G.M.** (1982) Early proterozoic climates and plate motions inferred from major element chemistry of lutites. *Nature*, **299**, 715–717.
- Newsom, H., Edgett, K., Fey, D., Wiens, R., Frydenvang, J., Banham, S.G., Gupta, S., Williams, A.J., Grotzinger, J.P., Mangold, N., Schieber, J., Rivera-Hernandez, F. and Belgacem, I.** (2018) A buried aeolian lag deposit at an unconformity between the Murray and Stimson formations at Marias Pass, Gale Crater, Mars. Lunar and Planetary Science Conference, abstract # 2263, Mar 2018, Houston, TX, USA.
- Ocampo-Díaz, Y.Z.E., Sosa-Ceballos, G., Saucedo, R., Macías, J.L., Bolós, X., Radilla-Albarrán, U.A., Martínez-Paco, M., Salinas-Ocampo, U. and Cisneros-Máximo, G.** (2021) Provenance and compositional variations of intra-caldera lake sediments at La Primavera, Jalisco, Western Mexico. *J. S. Am. Earth Sci.*, **110**, 103335.
- Osinski, G.R.** (2006) Effect of volatiles and target lithology on the generation and emplacement of impact crater fill and ejecta deposits on Mars. *Meteorit. Planet. Sci.*, **41**, 1571–1586.
- Palmer, B.A. and Shawkey, E.P.** (1997) Lacustrine sedimentation processes and patterns during effusive and explosive volcanism, Challis volcanic field, Idaho. *J. Sed. Res.*, **67**, 154–167.
- Palucis, M.C., Dietrich, W.E., Hayes, A.G., Williams, R.M.E., Gupta, S., Mangold, N., Newsom, H., Hardgrove, C., Calef, F., III and Sumner, D.Y.** (2014) The origin and evolution of the Peace Vallis fan system that drains to the Curiosity landing area, Gale Crater, Mars. *J. Geophys. Res. Planets*, **119**, 705–728.
- Pietruszka, A.J. and Garcia, M.O.** (1999) A rapid fluctuation in the mantle source and melting history of Kilauea Volcano inferred from the geochemistry of its historical summit lavas (1790–1982). *J. Petrol.*, **40**, 1321–1342.
- Prospero, J.M.** (1981) Eolian transport to the world ocean. In: *The Sea, Volume 7, The Oceanic Lithosphere* (Ed Emiliani, C.), pp. 801–874. John Wiley and Sons, New York, NY.
- Pye, K. and Tsoar, H.** (2009) Aeolian bed forms. In: *Aeolian Sand and Sand Dunes* (Eds Pye, K. and Tsoar, H.), pp. 175–253. Unwin Hyman, London.
- Rapin, W., Ehlmann, B.L., Dromart, G., Schieber, J., Thomas, N.H., Fischer, W.W. and Vasavada, A.R.** (2019) An interval of high salinity in ancient Gale crater lake on Mars. *Nat. Geosci.*, **12**, 889–895.
- Reineck, H.E. and Singh, I.B.** (1980) *Depositional Sedimentary Environments*. Springer Study Edition. Springer, Berlin, Heidelberg.
- Remy, R.R.** (1992) Stratigraphy of the Eocene part of the Green River Formation in the south-central part of the Uinta Basin, Utah. U.S. Geological Survey Bulletin 1787-BB.
- Renaut, R.W. and Gierlowski-Kordesch, E.H.** (2010) Lakes. In: *Facies Models 4* (Eds James, N.P. and Dalrymple, R.W.) *Geol. Assoc. Can. GEOText*, **6**, 541–575.
- Rhodes, M.K. and Carroll, A.R.** (2015) Lake type transition from balanced-fill to overfilled: laney member, Green River Formation, Washakie Basin, Wyoming. In: *Stratigraphy and Paleolimnology of the Green River Formation, Western USA*. Syntheses in Limnogeology, Vol. 1 (Eds Smith, M. and Carroll, A.), pp. 103–125. Springer, Dordrecht.
- Rhodes, M.K., Carroll, A.R., Pietras, J.T., Beard, B.L. and Johnson, C.M.** (2002) Strontium isotope record of paleohydrology and continental weathering, Eocene Green River Formation, Wyoming. *Geology*, **30**, 167–170.
- Rivera-Hernández, F., Sumner, D.Y., Mangold, N., Banham, S.G., Edgett, K.S., Fedo, C.M., Gupta, S., Gwizd, S., Heydari, E., Maurice, S., Nachon, M., Newsom, H., Schieber, J., Stack-Morgan, K., Stein, N. and Wiens, R.C.**

- (2020) Grain size variations in the Murray Formation: stratigraphic evidence for changing depositional environments in Gale Crater, Mars. *J. Geophys. Res. Planets*, **125**, e2019JE006230.
- Rubin, D.M.** (1987) *Cross-Bedding, Bedforms, and Paleocurrents. SEPM Concepts in Sedimentology and Paleontology*, Vol 1, p. 187. SEPM Society for Sedimentary Geology, Tulsa, OK.
- Rubin, M.** and **Hunter, R.E.** (1983) Reconstructing bedform assemblages from compound crossbedding. In: *Developments in Sedimentology*, Vol. 38 (Eds Brookfield, M.E. and Ahlbrandt, T.S.), pp. 407–427. Elsevier, Amsterdam.
- Schieber, J.** (1998) Possible indicators of microbial mat deposits in shales and sandstones: examples from the Mid-Proterozoic Belt Supergroup, Montana, U.S.A. *Sed. Geol.*, **120**, 105–124.
- Schieber, J.** (2011) Reverse engineering mother nature—shale sedimentology from an experimental perspective. *Sed. Geol.*, **238**, 1–22.
- Schieber, J.** (2018) How small is it? Pushing MAHLI to the limit in the search for mudstones at Gale crater, Mars. 49th Lunar and Planetary Science Conference, The Woodlands, Texas, USA, March 19–23, 2018, 1100 pp.
- Schieber, J.** and **Shao, X.** (2021) Detecting detrital carbonate in shale successions – relevance for evaluation of depositional setting and sequence stratigraphic interpretation. *Mar. Petrol. Geol.*, **130**, 105130.
- Schieber, J., Bish, D., Coleman, M., Reed, M., Hausrath, E.M., Cosgrove, J., Gupta, S., Minitti, M.E., Edgett, K.S. and Malin, M.** (2017) Encounters with an unearthly mudstone: understanding the first mudstone found on Mars. *Sedimentology*, **64**, 311–358.
- Schieber, J., Bohacs, K., Coleman, M., Bish, D., Reed, M.H., Thompson, L., Rapin, W. and Yawar, Z.** (2022) Mars is a Mirror – Understanding the Pahrump Hills Mudstones from a perspective of earth analogues. *Sedimentology*, **69**, 2371–2435.
- Schieber, J., Bohacs, K.M., Coleman, M., Bish, D., Reed, M.H., Thompson, L., Rapin, W. and Yawar, Z.** (2022) Mars is a mirror – understanding the Pahrump Hills mudstones from a perspective of Earth analogues. *Sedimentology*, **69**, 2371–2435.
- Schieber, J., Miclaus, C., Seserman, A., Liu, B. and Teng, J.** (2019) When a mudstone was actually a “sand”: results of a sedimentological investigation of the bituminous marl formation (Oligocene), Eastern Carpathians of Romania. *Sed. Geol.*, **384**, 12–28.
- Schieber, J., Minitti, M.E., Sullivan, R., Edgett, K.S., Malin, M.C., Parker, T. and Calef, F.** (2020) Engraved on the rocks—aeolian abrasion of Martian mudstone exposures and their relationship to modern wind patterns in Gale Crater, Mars. *Depos. Rec.*, **6**, 625–647.
- Schieber, J., Southard, J.B. and Schimmelmann, A.** (2010) Lenticular shale fabrics resulting from intermittent erosion of water-rich muds—interpreting the rock record in the light of recent flume experiments. *J. Sed. Res.*, **80**, 119–128.
- Schieber, J., Sumner, D., Bish, D., Stack, K., Minitti, M., Yingst, A., Edgett, K., Malin, M., Grotzinger, J. and MSL Science Team.** (2015) The Pahrump succession in Gale Crater—a potential evaporite bearing lacustrine mudstone with resemblance to Earth analogs. Lunar and Planetary Science Conference, 46, 2153.
- Schmidt, M.E., Farrand, W.H., Johnson, J.R., Schröder, C., Hurowitz, J.A., McCoy, T.J., Ruff, S.W., Arvidson, R.E., Des Marais, D.J., Lewis, K.W. and Ming, D.W.** (2009) Spectral, mineralogical, and geochemical variations across Home Plate, Gusev Crater, Mars indicate high and low temperature alteration. *Earth Planet. Sci. Lett.*, **281**, 258–266.
- Schumm, S.A.** (1977) *The Fluvial System*, p. 338. John Wiley & Sons, New York, NY.
- Schumm, S.A.** (1981) Evolution and response of the fluvial system: sedimentologic implications. In: *Recent and Ancient Nonmarine Depositional Environments: Models for Exploration* (Eds Ethridge, F.G. and Flores, R.M.), SEPM Spec. Publ. **31**, 19–29.
- Shaw, J.B., Ayoub, F., Jones, C.E., Lamb, M.P., Holt, B., Wagner, R.W., Coffey, T.S., Chadwick, J.A. and Mohrig, D.** (2016) Airborne radar imaging of subaqueous channel evolution in Wax Lake Delta, Louisiana, USA. *Geophys. Res. Lett.*, **43**, 5035–5042.
- Siebach, K.L., Baker, M.B., Grotzinger, J.P., McLennan, S.M., Gellert, R., Thompson, L.M. and Hurowitz, J.A.** (2017) Sorting out compositional trends in sedimentary rocks of the Bradbury group (Aeolis Palus), Gale crater, Mars. *J. Geophys. Res. Planets*, **122**, 295–328.
- Smith, M.E., Carroll, A.R., Jicha, B.R., Cassel, E.J. and Scott, J.J.** (2015) Paleogeographic record of Eocene Farallon slab rollback beneath western North America: REPLY. *Geology*, **43**, e364.
- Smoot, J.P. and Lowenstein, T.K.** (1991) Depositional environments of non-marine evaporites. In: *Evaporites, Petroleum, and Mineral Resources* (Ed. Melvin, J.L.), *Developments in Sedimentology*, **50**, 189–347.
- Southard, J.B. and Boguchwal, L.A.** (1990) Bed configuration in steady unidirectional water flows. Part 2. Synthesis of flume data. *J. Sed. Petrol.*, **60**, 658–679.
- Stack, K.M., Grotzinger, J.P., Lamb, M.P., Gupta, S., Rubin, D.M., Kah, L.C., Edgar, L.A., Fey, D.M., Hurowitz, J.A., McBride, M., Rivera-Hernández, F., Sumner, D.Y., Van Beek, J.K., Williams, R.M.E. and Yingst, R.A.** (2019) Evidence for plunging river plume deposits in the Pahrump Hills member of the Murray formation, Gale crater, Mars. *Sedimentology*, **66**, 1768–1802.
- Stanley, K.O. and Surdam, R.C.** (1978) Sedimentation on the front of Eocene Gilbert-type deltas, Washakie Basin, Wyoming. *J. Sed. Res.*, **48**, 557–573.
- Stockhecke, M., Sturm, M., Brunner, I., Schmincke, H.U., Sumita, M., Kipfer, R., Cukur, D., Kwiecien, O. and Anselmetti, F.S.** (2014) Sedimentary evolution and environmental history of Lake Van (Turkey) over the past 600 000 years. *Sedimentology*, **61**, 1830–1861.
- Taylor, K.G. and Macquaker, J.H.** (2014) Diagenetic alterations in a silt-and clay-rich mudstone succession: an example from the Upper Cretaceous Mancos Shale of Utah, USA. *Clay Mineral.*, **49**, 213–227.
- Taylor, S.R. and McLennan, S.** (2009) *Planetary Crusts: Their Composition, Origin and Evolution*, Vol. 10. Cambridge University Press, Cambridge, UK.
- Thomas, N.H., Ehlmann, B.L., Meslin, P.-Y., Rapin, W., Anderson, D.E., Rivera-Hernández, F., et al.** (2019) Mars Science Laboratory observations of chloride salts in Gale crater, Mars. *Geophys. Res. Lett.*, **46**, 10754–10763.
- Thompson, L.M., Berger, J.A., Spray, J.G., Fraeman, A.A., McCraig, M.A., O'Connell-Cooper, C.D., Schmidt, M.E., VanBommel, S., Gellert, R., Yen, A. and Boyd, N.I.** (2020) APXS-derived compositional characteristics of the Vera Rubin Ridge and Murray Formation, Gale crater, Mars: geochemical implications for the origin of the ridge. *J. Geophys. Res. Planets*, **125**, e2019JE006319.

- Thomson, B.J., Bridges, N.T., Milliken, R., Baldridge, A., Hook, S.J., Crowley, J.K., et al.** (2011) Constraints on the origin and evolution of the layered mound in Gale crater, Mars, using Mars Reconnaissance Orbiter data. *Icarus*, **214**, 413–432.
- Tomanka, G.D.** (2013) Morphology, mechanisms, and processes for the formation of a non-bifurcating fluvial-deltaic channel prograding into Grapevine Reservoir, Texas. Thesis (M.S.), University of Texas at Arlington, 113 pp.
- Trepmann, C.A., Dellefant, F., Kaliwoda, M., Hess, K.-U., Schmahl, W.W. and Hözl, S.** (2020) Quartz and cristobalite ballen in impact melt rocks from the Ries impact structure, Germany, formed by dehydration of shock-generated amorphous phases. *Meteorit. Planet. Sci.*, **55**, 2360–2374.
- Vlastellic, I., Peltier, A. and Staudacher, T.** (2007) Short-term (1998–2006) fluctuations of Pb isotopes at Piton de la Fournaise volcano (Reunion Island): origins and constraints on the size and shape of the magma reservoir. *Chem. Geol.*, **244**, 202–220.
- Watkins, J.A., Grotzinger, J.P., Stein, N.T., Banham, S.G., Gupta, S., Rubin, D.M., Stack-Morgan, K., Edgett, K.S., Frydenvang, J., Siebach, K.L., Lamb, M.P., Sumner, D.Y. and Lewis, K.W.** (2022) Burial and exhumation of sedimentary rocks revealed by the base Stimson erosional unconformity, Gale crater, Mars. *J. Geophys. Res. Planets*, **127**, e2022JE007293.
- Werner, S.C.** (2019) In situ calibration of the Martian cratering chronology. *Meteorit. Planet. Sci.*, **54**, 1182–1193.
- Whaling, A.R.** (2018) Changes to subaqueous delta bathymetry following a high river flow event, Wax Lake Delta, USA. Thesis (M.S.), University of Arkansas, Fayetteville, 43 pp.
- Wiens, R.C., Maurice, S., Barracough, B., Saccoccio, M., Barkley, W.C., Bell, J.F., Bender, S., Bernardin, J., Blaney, D., Blank, J., Bouyé, M., Bridges, N., Bultman, N., Cais, P., Clanton, R.C., Clark, B., Clegg, S., Cousin, A., Cremers, D., Cros, A., DeFlores, L., Delapp, D., Dingler, R., D'Uston, C., Darby Dyar, M., Elliott, T., Enemark, D., Fabre, C., Flores, M., Forni, O., Gasnault, O., Hale, T., Hays, C., Herkenhoff, K., Kan, E., Kirkland, L., Kouach, D., Landis, D., Langevin, Y., Lanza, N., LaRocca, F., Lasue, J., Latino, J., Limonadi, D., Lindensmith, C., Little, C., Mangold, N., Manhes, G., Mauchien, P., McKay, C., Miller, E., Mooney, J., Morris, R.V., Morrison, L., Nelson, T., Newsom, H., Ollila, A., Ott, M., Pares, L., Perez, R., Poitrasson, F., Provost, C., Reiter, J.W., Roberts, T., Romero, F., Sautter, V., Salazar, S., Simmonds, J.J., Stiglich, R., Storms, S., Striebig, N., Thocaven, J.-J., Trujillo, T., Ulibarri, M., Vaniman, D., Warner, N., Waterbury, R., Whitaker, R., Witt, J. and Wong-Swanson, B.** (2012) The ChemCam instrument suite on the Mars Science Laboratory (MSL) rover: body unit and combined system tests. *Space Sci. Rev.*, **170**, 167–227.
- Williams, R.M.E., Grotzinger, J.P., Dietrich, W.E., Gupta, S., Sumner, D.Y., Wiens, R.C., Mangold, N., Malin, M.C., Edgett, K.S., Maurice, S., Forni, O., Gasnault, O., Ollila, A., Newsom, H.E., Dromart, G., Palucis, M.C., Yingst, R.A., Anderson, R.B., Herkenhoff, K.E., Le Mouélic, S., Goetz, W., Madsen, M.B., Koefoed, A., Jensen, J.K., Bridges, J.C., Schwenger, S.P., Lewis, K.W., Stack, K.M., Rubin, D., Kah, L.C., Bell, J.F., Farmer, J.D., Sullivan, R., Van Beek, T., Blaney, D.L., Pariser, O., Deen, R.G. and MSL Science Team** (2013) Martian fluvial conglomerates at gale crater. *Science*, **340**, 1068–1072.
- Yen, A.S., Morris, R.V., Ming, D.W., Schwenger, S.P., Sutter, B., Vaniman, D.T. and VanBommel, S.J.** (2021) Formation of tridymite and evidence for a hydrothermal history at Gale crater, Mars. *J. Geophys. Res. Planets*, **126**, e2020JE006569.
- Yuretich, R.F.** (1979) Modern sediments and sedimentary processes in Lake Rudolf (Lake Turkana) eastern rift valley, Kenya. *Sedimentology*, **26**, 313–331.
- Zamiatina, D.A., Zamyatin, D.A., Mikhalevskii, G.B. and Chebikin, N.S.** (2023) Silica Polymorphs Formation in the Jänsjärvi impact structure: tridymite, cristobalite, quartz, trace stishovite and coesite. *Minerals*, **2023**, 686.
- Zavala, C., Ponce, J.J., Arcuri, M., Drittanti, D., Freije, H. and Asensio, M.** (2006) Ancient lacustrine hyperpycnites: a depositional model from a case study in the Rayoso Formation (cretaceous) of West-Central Argentina. *J. Sed. Res.*, **76**, 41–59.

Manuscript received 18 June 2024; revision accepted 3 October 2024

Supporting Information

Additional information may be found in the online version of this article:

Appendix S1. Source information for images.

Appendix S2. Instrumentation and miscellaneous technical issues.

Appendix S3. Overview of APXS data.

Appendix S4. ChemCam Ca-sulphate grain size assessment.